Spatial temperature measurements and turbulence analysis using DTS in the LIAISE field campaign

Gijs Vis

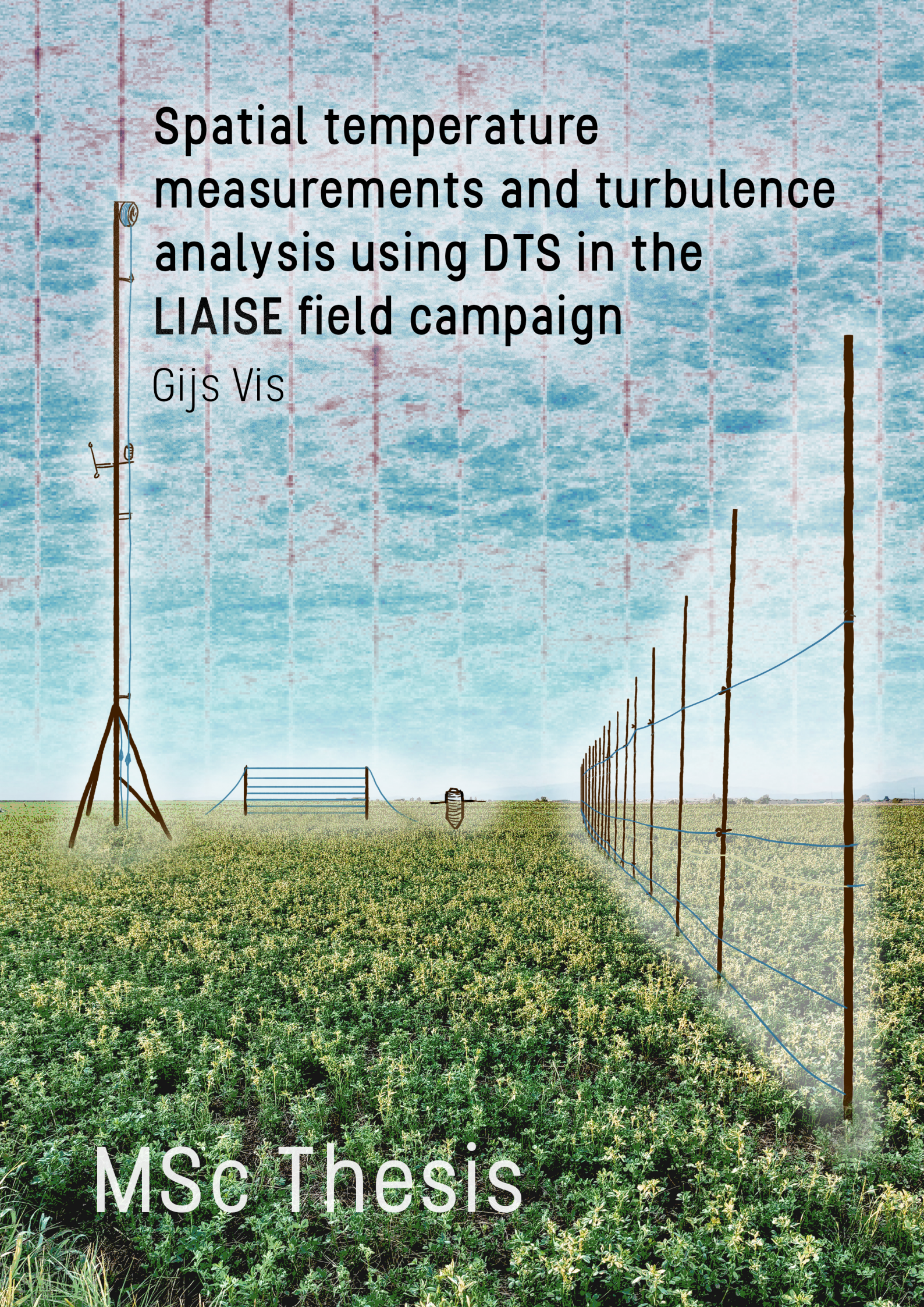

MSc Thesis

MSc Thesis

Spatial temperature measurements and turbulence analysis using DTS in the LIAISE field campaign

Author
Gijs Vis

Committee
Dr. ir. Miriam Coenders
Dr. ir. Oscar Hartogensis
Dr. ir. Marie-Claire ten Veldhuis

Delft University of Technology
Faculty of Civil Engineering and Geosciences
MSc Civil Engineering
Environmental Science

December 9, 2022

Acknowledgements

The MSc thesis presented here is the culmination of my 7.5 year period as a student, of which this thesis project encompassed the past 1.5 years. Both periods have been challenging and enriching on a personal and professional level, and I would like to mention some of the people involved in this period to thank them.

Starting academically, I want to thank my committee, Miriam Coenders, Oscar Hartogensis and Marie-Claire ten Veldhuis. Marie-Claire was of great help in the construction of the measurement set-ups in this field campaign. Oscar has introduced me to meteorological field campaigning and turbulent theory with a dedication that is exemplary.

And I especially want to thoroughly thank Miriam for the pro-active daily supervision, also on a personal level, the many coffee breaks we had, and the time and care she invested into bringing this thesis to a good end. I look forward to continue our collaboration after my graduation with enthusiasm and I am glad we met through the 'Measurements for Water' course.

My field of study has changed throughout the years from labwork on microscopy in the BSc Applied Physics to measuring the results obtained from this thesis, outdoors, within the MSc Environmental Engineering track. For this very welcome change I mostly want to thank Rolf Hut and my fellow Arctic Geophysics 2019 people in Svalbard. Rolf, thanks for all the talks we had and our collaboration during the last years. Svalbard people, you literally opened to world for me to go into environmental science. Tusen takk.

I would like to thank Christoph Thomas for sharing his extensive knowledge on fiber-optic distributed sensing during the 2022 Svalbard campaign and for thinking along in this project. Also Bas van de Wiel deserves thanks for taking the time to enthusiastically think along with this project. I want to mention Remko Uijlenhoet for making it possible to go to this field campaign during uncertain Covid-19 times. I want to thank the LIAISE-NL group for the fantastic experience of my first proper field campaign and then in particular Jordi Vila for being a great Catalonian host.

Op persoonlijk niveau wil ik ook een aantal mensen bedanken. Bedankt Ties, Daan en Puck voor het kritisch doorlezen van mijn thesis. Daarnaast veel dank aan de groep mede-studenten en -muzikanten voor de steun en de avonturen tijdens de afgelopen jaren. Daaronder vallen bijvoorbeeld Dante, Gijs van G., Daan, Jurriaan, Bente, Ties, Lucas, Lukas, Iris, Larissa, Wietske en nog een aantal anderen. In het bijzonder wil ik Puck Bieseman bedanken, voor onze sterke vriendschap van al meer dan 10 jaar en voor de schitterende voorpagina die je hebt gemaakt voor dit werk. Added to this list should also be Svenja, who has been an incredibly supportive friend ever since we met in the Polar night of 2019. Danke.

Als laatste wil ik mijn familie bedanken. Jullie zijn een ontzettende steun en motivatie geweest in het leren en studeren over de jaren heen. Met eerlijkheid kan ik zeggen dat ik niet zo ver was gekomen zonder zo'n fijne thuisbasis in Valkenburg. Ontzettend bedankt. De opa's en oma's kijken trots mee met het resultaat wat jullie mogelijk hebben gemaakt.

Gijs Vis

December 2022

Abstract

Experiments using fiber-optical set-ups for distributed temperature sensing (DTS) were conducted in the LIAISE (Land surface Interactions with the Atmosphere over the Iberian Semi-arid Environment) field campaign during 15-30 July 2021 in the north-east of Spain. Three DTS set-ups were installed to measure temperature profiles along varying vertical scales; 1.6 - 40 m in the atmosphere, 0 - 1 m into the rapidly-growing alfalfa canopy and -0.5 - 0 m in the soil. Measurements were conducted at 5 s and 25.4 cm resolutions using a 1.6 mm Kevlar-reinforced fiber. The preliminary data of these three set-ups are described in the first part of this thesis, which display the potential of using DTS in a land surface campaign to capture vertical temperature structure in great detail.

A fourth fiber-optic set-up was installed with a horizontal extent of 70 m, measuring at four heights between 0.40 m and 2.05 m height. A thinner 0.5 mm cable was used here in an effort to obtain the fastest possible time response in order to measure temperature turbulence parameters using DTS. Measurements were made at 1 Hz and 12.7 cm resolution, however the actual sampling frequency appeared to be 0.15 Hz in the temperature spectrum, likely because of the long response time of the cable.

Despite the limited 0.15 Hz sampling rate it was possible to obtain turbulence information through the use of the structure parameter of temperature, C_T^2 . This parameter indicates the intensity of temperature fluctuations and was calculated over time, as is conventional. In a novel approach, it was also calculated over space, using the spatio-temporal dataset as obtained by DTS. Both the definition of C_T^2 and the inertial range of the temperature spectrum were used to determine C_T^2 . The spatial C_T^2 obtained through the definition method was found to have the best correlation with a sonic anemometer reference, with an R^2 of 0.88. The temporal C_T^2 lack the structure that is shown in the spatial C_T^2 , which is likely due to 30-min averaged data for horizontal wind speed from the sonic anemometer or to Taylor's frozen turbulence hypothesis not being a suitable assumption within the dimensions of this research. Determining C_T^2 through the turbulent spectrum was successful for limited data points for the time series, and is currently inconclusive for the spatial series.

Recommendations for further research for using DTS in turbulence analysis are to investigate the effect of instrument noise and the limited sampling rate. Also a critical look into the current DTS calibration routines for atmospheric is recommended. This work provides a first step towards using DTS in capturing turbulent information along spatial temperature series.

Contents

1. Introduction

The impact of human activities on future water resources is one of the major focus areas of environmental science. This change in water availability is especially critical in semi-arid regions that serve as the bread baskets of the world, as water resources in these regions are already scarce, as is outlined in the WCRP Grand Challenge on *Water for the Food Baskets of the World* (Van Oevelen et al., 2020). One of these bread basket regions is the Mediterranean Basin, which is projected to be one of the 21st century climate hot spots of the world (Cos et al., 2022).

The Mediterranean Basin is typical highly heterogeneous area, it being a combination of naturally arid areas and man-made irrigated areas. Within the Basin, precipitation generally only occurs in winter or in the mountain ranges (Cos et al., 2022), so to perform consistent agriculture the use of dams and irrigation is therefore necessary. In other words, human intervention in the water system sustains these bread basket regions.

One example of a semi-arid region within the Mediterranean Basin is the Pla d'Urgell region of the Ebro River Valley in Catalonia, Spain. This is the location of the LIAISE (Land surface Interactions with the Atmosphere over the Iberian Semi-arid Environment) field campaign (Boone, 2019) that this project is based on. Human interventions in this semi-arid region have created a patchwork of dry and wet areas: a combination of naturally arid vegetation and irrigated crops (Figure 1a and 1b). As a result, an environment is made which is homogeneous on the scale of single fields, but heterogeneous on larger, regional scales.

Because of these differences in scale it can be complex to characterize the land-surface interaction of this area. One field can act as a source of atmospheric moisture by evaporation from irrigated crops, while a neighbouring dry field can have little moisture to offer, creating strong regional differences on moisture and heat fluxes. Furthermore, land-surface interaction has a time-dependence because of fast vegetation growth and intermittent irrigation, where fields are irrigated by flooding a large amount of water at specific times (Figure 1d). The combination of plant transpiration and evaporation driven by the Mediterranean solar radiation, then dry out the field over a period of typically two weeks (Figure 1c). This cyclical change of water availability combined with abundant availability of energy from radiation then drives a strong vegetation growing cycle of up to 5 cm per day.

Land-surface interactions are currently measured using a variety of state of the art techniques, such as resistive and capacitive measurements of temperature and humidity and sonic measurements of fluxes using eddy-covariance. However, these are typically time series of point measurements, which are in large contrast to atmospheric models that provide information in three dimensions in space and over time. In order to bridge this gap between modelling and measurement approaches, a large expansion of both the space and the time captured by measurements is desired.

Large-scale measurements can be done by satellites using remote sensing, but this requires in-situ validation and calibration. Another approach is scintillometry, which measures how fluctuations in temperature and humidity affect a wave propagating between two points. These fluctuations are a measure of atmospheric turbulence, which can be used to derive fluxes of heat, moisture and momentum (Moene et al., 2009). Scintillometry enables the capturing of information along a propagation path across 10^2 - 10^4 m, rather than at a single point, but it has also a limitation in the sense that this information is an integrated measurement along the scintillometer path.

To capture spatial information over time, ideally an instrument is used which is in between a point measurement and an integrated path, so both spatial and temporal information are available. Distributed

(a) Arid area (left) and irrigated area (right)

(b) Local variation of aridity between fields

(c) Dry field with a beginning crop of alfalfa

(d) Alfalfa crop being flood irrigated

Figure 1.: Overview of the environment in which the LIAISE field campaign was conducted, in July 2021 in the Lleida region of Catalonia, Spain, on different scales. Visible is a patchwork of arid and wet areas and fields with different stages of vegation. Figure **(a)** shows the difference in an area between arid and dry. Figure **(b)** shows the variation around the experimental location of La Cendrosa. Figures **(c)** and **(d)** show the differences on field between a dry field and a field being irrigated.

Temperature Sensing (DTS) can offer a solution for bridging the gap between point and integrated path measurements. DTS uses the non-elastic backscattering of light in fiber-optic cables to sense temperature, and with that enables spatial measurements of temperature along the fiber path. Improvements in precision and accuracy over the past two decades have allowed for the deployment of DTS across hydrology (Selker et al., 2006), meteorology (Thomas et al., 2012) and environmental sciences (Tyler et al., 2009).

By arranging the fiber with physical coordinates of interest, spatial measurements in an environmental situation of choice can be retrieved. Atmospheric profile measurements can capture features that would have gone unnoticed by conventional point measurements, such as shallow fog events (Izett et al., 2019), and can provide a vertical profile of temperature and humidity that is required to estimate the Bowen ratio (Schilperoort et al., 2018). 2D and 3D arrangements of fibers can be used to create vertical cross sections that can provide a look into turbulent structure (Hilland et al., 2022; Zeller et al., 2021). Additionally, other environmental parameters have been derived from these temperature measurements, such as wind speed and direction (Lapo et al., 2020), soil heat flux (Bense et al., 2016) and soil moisture (Steele-Dunne et al., 2010). These previous studies highlight the capability of DTS being used for environmental measurements and its potential in alleviating spatial limitations from point measurements.

The measurements of DTS allow for the determination of temperature gradients in a more rigorous way than by using conventional instrumentation, because the gradients can be determined by spatially distributed measurements. This is useful in determining components of the surface energy balance (SEB)

$$Q^* = H + \rho_w L_v E + G, \tag{1}$$

with Q^* the net radiation, H the sensible heat flux, $\rho_w L_v E$ the latent heat flux and G the ground heat flux, all in units of $\mathrm{W\,m^{-2}}$. Here the latent heat flux term is comprised of the density of water ρ_w in $\mathrm{kg\,m^{-3}}$, the latent heat of vaporisation L_v in $\mathrm{J\,kg^{-1}}$ and the evaporation E in $\mathrm{m\,s^{-1}}$. As a conceptual simplified surface energy balance, advection terms are ignored here. The SEB quantifies the energy budget within the land-atmospheric interaction, specifically the distribution of solar radiation into heat (H), evaporation ($\rho_w L_V E$) and into the ground (G). By measuring vertical temperature profiles with DTS within the soil ($\frac{\partial T_s}{\partial z}$), the ground heat flux

$$G = -\rho_s c_s \kappa_s \frac{\partial T_s}{\partial z}, \tag{2}$$

can be calculated using soil density ρ_s in $\mathrm{kg\,m^{-3}}$, heat capacity c_s in $\mathrm{J\,kg^{-1}\,K^{-1}}$ and thermal diffusivity κ_s in $\mathrm{m^2\,s^{-1}}$. Combining the DTS vertical temperature profiles of the atmosphere ($\frac{\partial T_a}{\partial z}$) with similarity theory a similar expression for the sensible heat flux

$$H = \rho c_p K_h \frac{\partial T_a}{\partial z}, \tag{3}$$

can be created. In this expression, the used turbulent diffusivity K_h (in $\mathrm{m^2\,s^{-1}}$) is a function of thermal diffusivity κ (in $\mathrm{m^2\,s^{-1}}$), friction velocity u_* (in $\mathrm{m\,s^{-1}}$), height z and a non-dimensional flux-gradient relationship ϕ_h (Moene and Van Dam, 2014). Converting temperature gradients $\frac{\partial T}{\partial z}$ into fluxes in $\mathrm{W\,m^{-2}}$ still requires external input, because the density, heat capacity and diffusivity need to be determined through other methods.

Vegetation also affects the vertical transport of energy in the surface energy balance, as it adds an extra layer of resistance and storage for heat and moisture. The storage of heat in the land is then split up from G into two separate components G_v and G_s for the vegetation and soil respectively. Therefore determining the vertical temperature gradients within the canopy is also an interesting application of DTS in the context of resolving the SEB. The terms of the surface energy balance that make up the vertical transport of energy are graphically summarized in Figure 2.

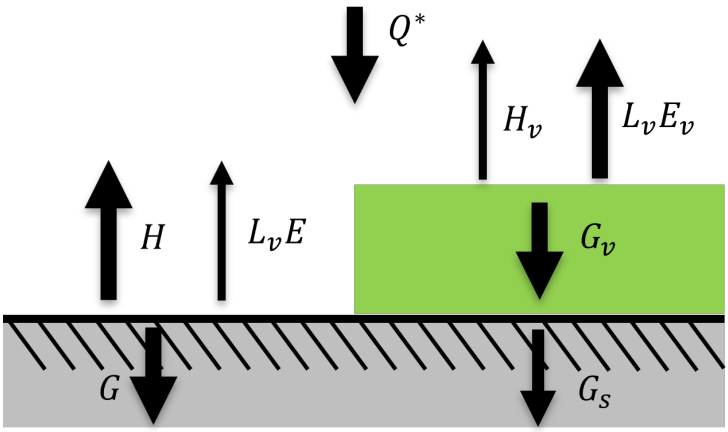

Figure 2.: Graphical interpretation of the surface energy balance (Equation 1) and the influence of vegetation. Incoming solar radiation Q^* is transported away into the atmosphere as sensible (H) and latent (L_vE) fluxes or stored in the land as ground (G) heat fluxes. Vegetation modulates these heat fluxes and splits storage into two separate components for soil (G_s) and vegetation (G_v). Advection terms (horizontal transport) are ignored in this interpretation.

An approach in measuring vertical temperature profiles of air, soil and vegetation is outlined in the first part of this work. Methods of three DTS set-ups are described in order to obtain mean vertical temperature profiles on several scales; 40 m into the air, 0.5 m into the ground and within the vegetation. The goal of this first part is to show the richness in possibilities of using DTS in a land surface interaction context to measure temperature spatially in great detail.

Other than vertically oriented set-ups, horizontally aligning fibers enables the possibility of looking into the horizontal distribution of temperature. This horizontal temperature information is typically not obtained with in-situ measurements in SEB campaigns. A fourth DTS set-up is used in the second part of this work to include horizontal temperature measurements over a scale of 70 m and a vertical scale of 2 m.

The core of the research in this work is however is in investigating the applicability of DTS for turbulent measurements. In order to obtain information about turbulence, turbulence parameters can be determined using temperature measurements from DTS. In this work the turbulence parameter used is the structure parameter of temperature, C_T^2 , which quantifies the intensity of temperature fluctuations over a certain scale and can be seen as a 'scaling parameter of the temperature spectrum in the inertial range of turbulence' (Hartogensis, 2006; Stull, 1988). The structure parameter can be determined using temperature series directly, using its definition. Alternatively, the inertial range of the turbulent temperature spectrum can be used to obtain C_T^2 through the Kolmogorov -5/3 power law (Stull, 1988). C_T^2 will be further introduced in Chapter 8.

The unique aspect of this research is that DTS enables the determination of structure parameters over both time and spatial series. Turbulent fluctuations can be determined over time by looking at a point of the fiber over time, similarly to the conventional approach of using a sonic anemometer. Multiple points along the fiber can be averaged over space to obtain turbulent information corresponds to using the line-of-sight measurements of scintillometers. However, by looking at a certain point in time along the fiber, a spatial temperature series can now also be used to determine C_T^2 . Additional (spatial) turbulent information is now available, adding to the already existing determination of the structure parameter using time series.

Turbulent parameters can then potentially be obtained over time and space, and by using a combination of time and space using averaging. In this analysis, the determination of the structure parameter is split up over time and space, as well as using either the definition of C_T^2 or the turbulent temperature spectrum. Therefore four different methods for obtaining turbulent information using DTS are investigated. The resulting structure parameters as also compared to a reference dataset obtained from a sonic anemometer. The main research question that is addressed in this work is

Can distributed temperature sensing be used to resolve temperature turbulence values over time and space?

To give an answer to this question, it is split up into several subquestions

- *How do structure parameters of temperature determined using DTS time series compare to a novel method of determining structure parameters using spatial data?*
- *How well do both methods using the definition of C_T^2 and using the turbulent temperature spectrum work for DTS temperature data?*
- *What is the correlation between temperature turbulence parameters obtained from DTS compared to those obtained from a sonic anemometer?*

This work starts with a description of the LIAISE experimental campaign and its location, this is followed by a chapter on the theory behind distributed temperature sensing. Then the work is split up into two parts. The first part concerns the description of temperature profiles obtained with three vertical DTS set-ups; 40 m into the air, 0.5 m into the ground and within the vegetation respectively. The second part of this study is centered around turbulence analysis using a DTS set-up that extends 2 m vertically and 70 m horizontally. Both parts will present a method describing the set-ups deployed and the research approach, after which results of the method are presented along with a discussion and a conclusion.

2. Campaign description

The measurements used in this study were conducted over a 15 day period between 15 and 30 July 2021 during the Special Observation Period (SOP) of the LIAISE field campaign. The SOP was a period of intensive collaborated experiments that were part of a longer campaign that was running April through September 2021. The location of the campaign was a region of approximately 10 km radius in the Pla d'Urgell region in north-eastern Spain. Specifically, the measurement location was a field of irrigated alfalfa called La Cendrosa, located at 41.69336 °N and 0.92841 °E at an altitude of 240 m. The region around La Cendrosa is shown in Figure 1 and a top view of the site is shown in Figure 4. Figure 3 shows the campaign location within Spain.

(a) Location of the campaign within Spain.

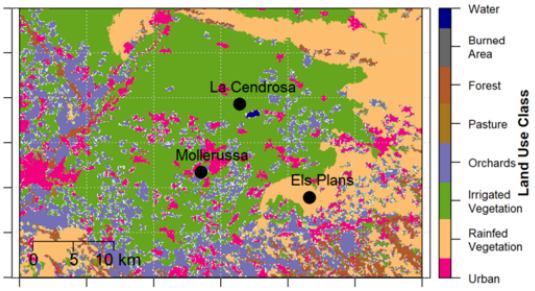

(b) Land use of the region of the campaign.

Figure 3.: LIAISE campaign location in Spain (Figure **(a)**) and the research area (Figure **(b)**).

Conditions in the area at this time of year are typically hot and dry, with maximum 2 m temperatures reaching 30 - 35 °C and occasional convective precipitation. The predominant wind regime is a weaker (south)westerly during the day that increases magnitude and switches direction in the afternoon because of the sea breeze effect. July is part of the dry season, with an average monthly precipitation of 12 mm and skies that are typically clear or consist of high clouds.

The alfalfa crop was cut and harvested before the campaign on 5 July and irrigated on 10 July, so the SOP started with a starting alfalfa crop, similar to Figure 1c and Figure 5a. The crop grew about 4 cm per day until 70 cm at the end of the SOP and was irrigated once during this period on the night of 23 to 24 July (Figure 1d).

Four distributed temperature sensing set-ups were installed in this experiment and points of interest for these set-ups are marked in Figure 4. Point 1 was the location of the cabin that houses the DTS electronical and calibration equipment. Three of the set-ups were vertically oriented and located at points 2, 3 and 4. At point 2 a 50 m meteorological mast was operated by Meteo France, to which a fiber was attached up to 40 m. Point 3 had a set-up which was dug into the soil, a so-called ground coil and adjacent to it was an in-canopy set-up at point 4. Co-located at point 3 and 4 was a soil measurement site operated by Wageningen University and Research. These three set-ups are described in more detailed in the Methods chapter of Part 1.

A horizontal set-up in the form of a fence (harp) was installed over 70 m between points 5 and 6 and parallel to points 7 and 8 which are the beginning and end points of pair of laser scintillometers. Both these paths are oriented perpendicular to the predominant south-westerly wind direction to capture the same footprint as much as possible. This set-up is the focus of Part 2 and described in more detail in the chapters there.

Figure 4.: Top view of the La Cendrosa measurement site, from RBG drone composite images. The instrumentation is centered around a field of approximately 300 m x 400 m containing irrigated alfalfa and bordered by other fields and a farm to the west. Eight locations of interest are marked on the figure: Cabin containing DTS computers **(1)**, 50 m mast **(2)**, ground coil **(3)**, canopy harp **(4)**, beginning **(5)** and end **(6)** of the turbulence harp and the beginning **(7)** and end **(8)** of the scintillometer path.

(a) Early alfalfa canopy **(b)** Late alfalfa canopy

Figure 5.: Alfalfa canopy at La Cendrosa for two different growth stages. The vegetation starts as a sparsely covering canopy and grows into a dense crop of 1 m height at a rate of approximately 4 cm d^{-1}.

3. Distributed temperature sensing

The concept behind distributed sensing with fiber optics is observing the conditions around a specific length along the fiber (LAF, or x_L) by using the travel time of the light within the fiber. These conditions are monitored by sending a near-infrared pulsed laser signal into the fiber and by then measuring the backscattering in the fiber after each pulse as a function of x_L. Translating the measured conditions from a function of x_L into a physical coordinate system then gives spatially-distributed information of the conditions at the location of the fibers in the real world (Selker et al., 2006).

Light travelling through a fiber optic core has a small chance of being backscattered non-elastically by Raman scattering. There are two components within Raman scattering; a Stokes and an anti-Stokes component. Both components are dependent on the intensity of the laser and the attenuation along the fiber. Besides that, the anti-Stokes component has a strong temperature dependence, as opposed to a weak dependence for the Stokes component (Bao and Chen, 2012).

The measurements of a DTS instrument consist of the power of both the Stokes $P_+(x_L, t)$ and the anti-Stokes $P_-(x_L, t)$ components as a function of time and length along the fiber. Dividing the two components then gives an expression which is dependent on the temperature, but independent of laser intensity. This expression, the power ratio

$$I(x_L, t) = \ln\left(\frac{P_+(x_L, t)}{P_-(x_L, t)}\right), \tag{1}$$

is used to get an equation for temperature T that is called the DTS equation

$$T\left(x_L, t\right) = \frac{\gamma}{I\left(x_L, t\right) + C(t) + \int_0^{x_L} \Delta\alpha(x'_L)dx'_L}. \tag{2}$$

Here γ and $C(t)$ are set-up specific sensitivities of temperature and the detector respectively. $\Delta\alpha$ is the differential attenuation, which is the difference in attenuation between both Raman components. The differential attenuation is a function of the fiber length and is affected by physical properties of the fiber, such as bends, connections and the type of fiber (Hausner et al., 2011).

The power ratio I is the input signal of the instrument and the temperature T as a function of fiber length and time is the desired output. The temporal and spatial resolutions of T are limited by the signal processing of the input within the instrument. The temporal resolution is limited by the ability of the instrument to statistically measure the power of the received Raman components, which are typically weak signals in the order of nW. Spatial averaging, which is dependent on fiber type and signal processing speed, limits the spatial resolution of T. The resolutions of current state-of-the art instruments are in the order of 1 s and 10 cm.

DTS measures a ratio of powers and therefore yields a relative temperature. To convert this ratio into an absolute temperature, an external comparison is needed. For this, sections of the fiber are placed in a stable environment with known temperature. Typically, insulated baths filled with water are used for these reference sections, called calibration baths. The fiber is loosely coiled in the bath and a pump is used to maintain homogeneous temperature within the bath.

A schematic view of a calibration bath is shown in Figure 6b and the application of calibration baths in the LIAISE campaign are shown in Figures 6a and 6a. Comparing the temperatures in the calibration baths

(a) Top view with several fibers, without water, sensors, and mixing equipment

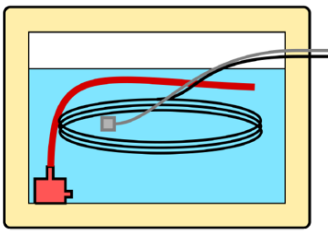

(b) Schematic view of calibration bath

(c) Two stacked baths deployed in the field, including water.

Figure 6.: Schematic and deployed view of calibration baths. **(a)** shows the lengths of fiber coiled into an insulated bath before filling with water. **(b)** gives a schematic view of a bath, with the coil of fiber in black, mixing equipment in red and an external sensor in gray. **(c)** shows two calibration baths as deployed in the experiment, including water and sensors.

with an external temperature sensor then converts the raw measurements into a physically meaningful temperature. This conversion has been implemented in the open-source Python package DTSCALIBRATION (des Tombe et al., 2020).

Part 1: Spatial temperature measurements: Mean profiles

The aim of Part 1 is to give a broad perspective into the potential of applying distributed temperature sensing within the context of a land surface interaction campaign. Three vertical DTS set-ups are described to measure temperature profiles on different vertical scales; in the air (1.6 m - 40 m), the soil (-0.5 m - 0 m) and the vegetation layer (0 m - 1 m). An overview of the resulting dataset is given with a discussion of the limitations and possibilities for future research.

4. Methods

4.1. DTS set-ups

4.1.1. General

The three vertical set-ups (50 m mast, ground coil and canopy harp) were linked together in one continuous, single-ended, fiber. The path of this fiber through the set-ups and components is shown in Figure 7. The fiber began in an air-conditioned cabin, which also housed the DTS (SiliXa Ultima M) computer and laser. A calibration bath with temperature T_{in} was also located in the cabin, which was left to be in thermal equilibrium with the cabin air temperature.

Two calibration baths were located in the field, stacked on top of each other, as visible in Figure 6c. The top bath was exposed to direct short-wave radiation and therefore had a warm temperature T_{sun}. The bottom bath was covered from direct radiation by the top bath and had a cooler temperature T_{shade}. In order to keep a desired temperature difference between the top and bottom bath, the bottom bath was also cooled. Each day the water had to be refreshed and ice packs were added in order to keep T_{shade} low.

The three set-ups were joined together by two splices in between the calibration baths, which split up the fiber in three sections. The fiber was run back and forth through the calibration baths, so that each set-up had at least two reference sections within that section of the fiber. Each calibration bath contained an external sensor to record an independent temperature to be used for calibration. Both Pt-100 sensors and HOBO TidbiT Water Temperature Data Loggers were used for this purpose.

To locate the physical extent of the set-ups along the length of the fiber, ice packs were placed at key locations of the set-ups. In this way, sharp temperature drops could be seen in the raw data at certain LAF, which were then translated to corresponding physical locations in an (x, y, z) coordinate system. In this coordinate system, z is the vertical coordinate, pointed upwards from ground level, x is the horizontal coordinate running along a length of fiber, and y is the horizontal coordinate perpendicular to the direction of the fiber.

To convert the recorded raw data from the DTS computer into physical quantities, the open-source package PYFOCS (Lapo and Freundorfer, 2020) was used. This package handles the processing of DTS data by archiving the raw data, performing calibration using the DTSCALIBRATION routine (des Tombe et al., 2020) and mapping the calibrated temperatures to a physical coordinate system (Schilperoort et al., 2020). Processing is performed based on a user-defined configuration file, which consists of the physical coordinates of the set-ups and the calibration baths and the desired settings to be used. The workflow of PYFOCS is shown in Figure 8.

The coordinates of the reference sections and the set-ups were initially input as recorded in the field using the ice pack method and then changed iteratively based on the raw temperature data (lower left of Figure 8). The processed data was saved separately for each set-up in NetCDF files in intervals of 30 minutes.

Each of the three set-ups in this part work with a temporal resolution of 5 s and a spatial resolution of 25.4 cm, which are the resolution limits of the Ultima M. A 1.6 mm Kevlar reinforced fiber optic cable is used through the fiber path.

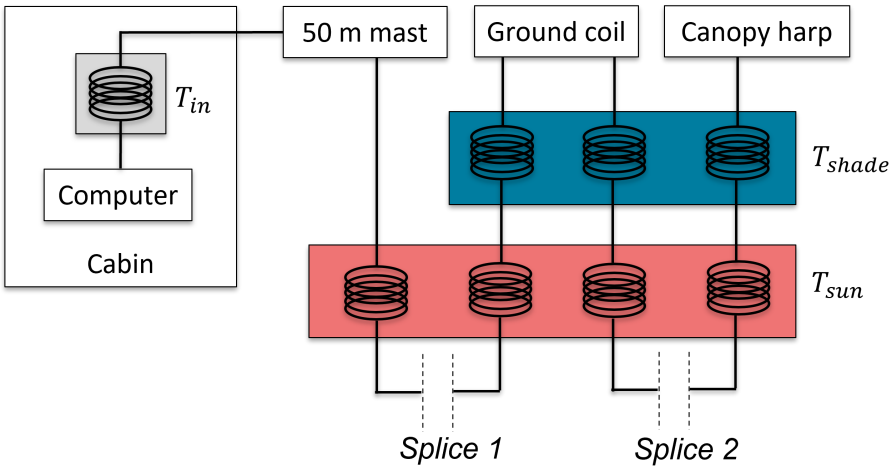

Figure 7.: Overview of the complete fiber path along the three vertical set-ups. The fiber path begins in an air-conditioned cabin with a calibration bath of temperature T_{in}, then travels along the three set-ups; the 50 m mast, the ground coil and the canopy harp. Between set-ups, the fiber runs along two outdoor calibration baths. These calibration baths are placed on top of each other in the field, so that one of them is in the shade with a temperature T_{shade} and one of them is on top in direct radiation with temperature T_{sun}. There are two splices connecting the three set-ups into a single path.

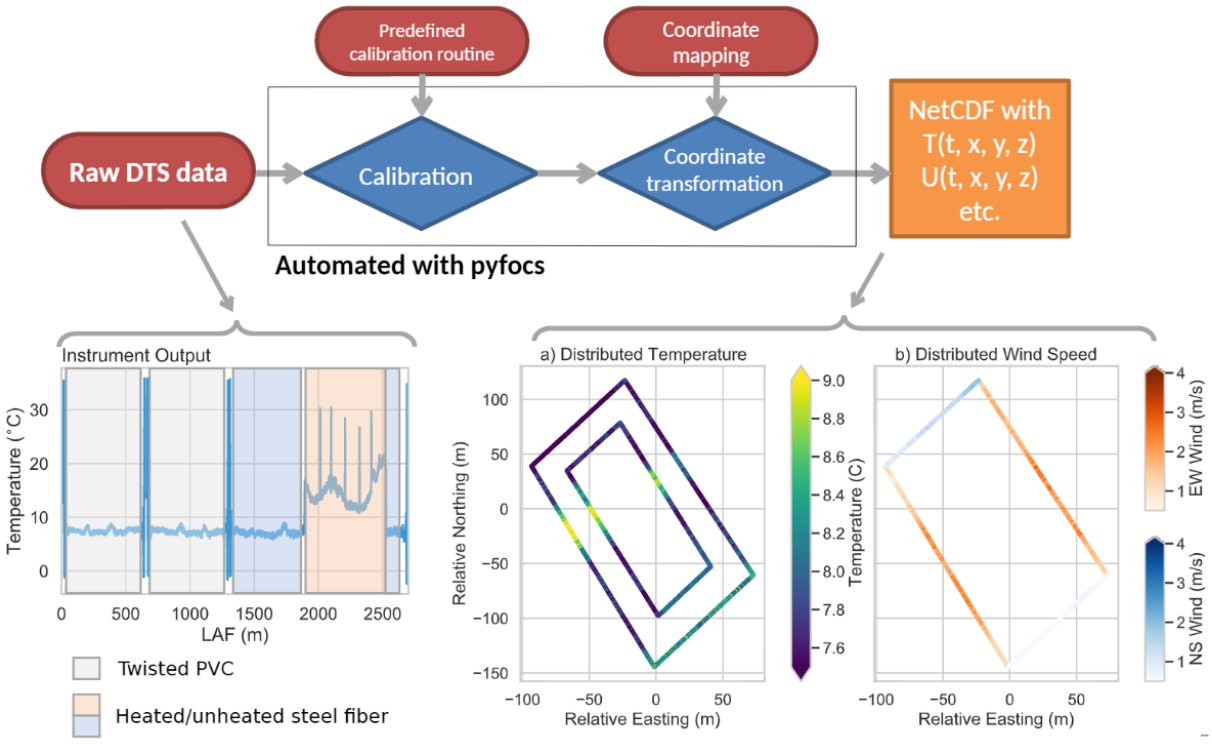

Figure 8.: Workflow of the data processing of DTS data using PYFOCS (Lapo and Freundorfer, 2020). Raw data in the form of Stokes and anti-Stokes intensities are transformed into physical temperatures using DTSCALIBRATION with a user-defined routine. The temperatures are then mapped to a physical coordinate system (from LAF to x, y, z) and saved as NetCDF files in a selected interval.

4.1.2. 50 m mast

The 50 m mast set-up is installed into a meteorological tower from Meteo France. The fiber optic cable goes upwards and downwards from $z = 1.6$ m to 40 m. The fiber is installed with the use of a pulley and rope system. A pulley is attached to the mast at $z = 40$ m, which has a rope along it going towards the surface in two directions. Upon deployment of the fiber onto the mast, the fiber is attached to the rope and hoisted upwards and then downwards using this pulley. After this, the fiber is fed back towards the cabin that houses the DTS computer.

In order to keep the fiber in a vertical orientation along the mast, especially during windy conditions, fiber guides made of PVC pipe were installed at several heights along the mast. These PVC guides can be seen in Figure 9a, which shows the PVC guide at $z = 3$ m and looks upwards along the tower. The PVC guides were installed at heights of $z = 3$, 8, 16, 20, 24, 27.5, 30, 32, 34, 36, 38, 40 m.

To prevent the fiber from slipping from its original position, for example by wind pulling it, it is clamped along its path. Slipping of the fiber should be prevented, as this creates complication in transforming the measurements from *LAF* to physical coordinates. The cable ties and hose clamps are used in order to apply enough pressure on that point of the fiber that it will not slip. To prevent breakage or damage to the fiber, and to minimize signal changes by distortion of the cable, pipe insulation foam was placed between the clamps and the fiber. A compilation of examples concerning the fastening and securing of the fiber can be found in the Appendix in Figure 57.

Figure 9 shows two views of the mast in the landscape and a schematic view of the fiber deployment along the mast, along with the positions of weather stations from Meteo France.

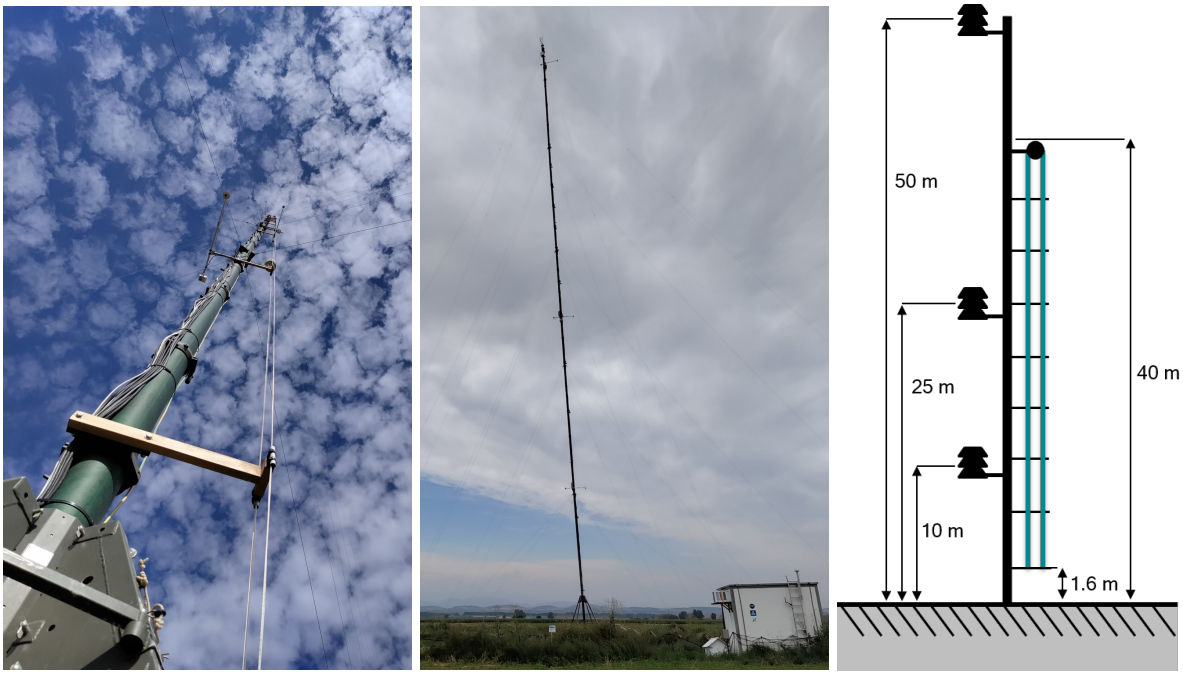

(a) Upwards view **(b)** Total view **(c)** Schematic view

Figure 9.: Overview of the 50 m mast set-up, with a fiber installed adjacent to a 50 m mast from 1.6 m height up to 40 m upwards and then downwards. Also located on the mast are three Meteo France weather stations at 10 m, 25 m and 50 m.

4.1.3. Ground coil

The set-up to measure temperature profiles into the soil is based on a 3D printed column around which the fiber is wrapped like a coil. The design process of the coil is described in a technical note by Schilperoort (2022) and its 3D design can be found on GitHub (Schilperoort, 2020). Figure 10 shows a view of the complete coil, as well as of it installed in the ground and a schematic view.

The coil is made of 3D printed PLA with an infill of 48%, so that its effective thermal conductivity is at least 4 times lower than typical dry soils. This is to create a minimal effect on the temperature distribution in the soil by the coil itself. The coil has slotted grooves to allow for both rigid installation of the fiber and sufficient contact with the soil.

A 1.6 mm fiber optic cable is installed into the coil and winds down the coil with each rotation having a length (circumference) of 24.7 cm, spaced apart by 1.25 cm. After completing the windings, the fiber then goes back up back through the centre of the column. The dimensions of these rotations combined with the spatial resolution of 25.4 cm result in an effective vertical resolution of 1.3 cm. The soil temperature profile obtained from the ground coil then has 43 data points.

For installation the ground coil has an attachable set of handles which also fit a spool containing extra fiber (see Figure 10a). This means that after pre-drilling a hole with an auger, it is possible to screw the coil into the ground using the handles. For screwing the ground coil into the ground, care must be taken to ensure proper contact with the ground, so that as little air gaps as possible are present between the coil and the soil. After screwing in, the spool on top can be rolled out to be put into the calibration baths and spliced to the rest of the fiber.

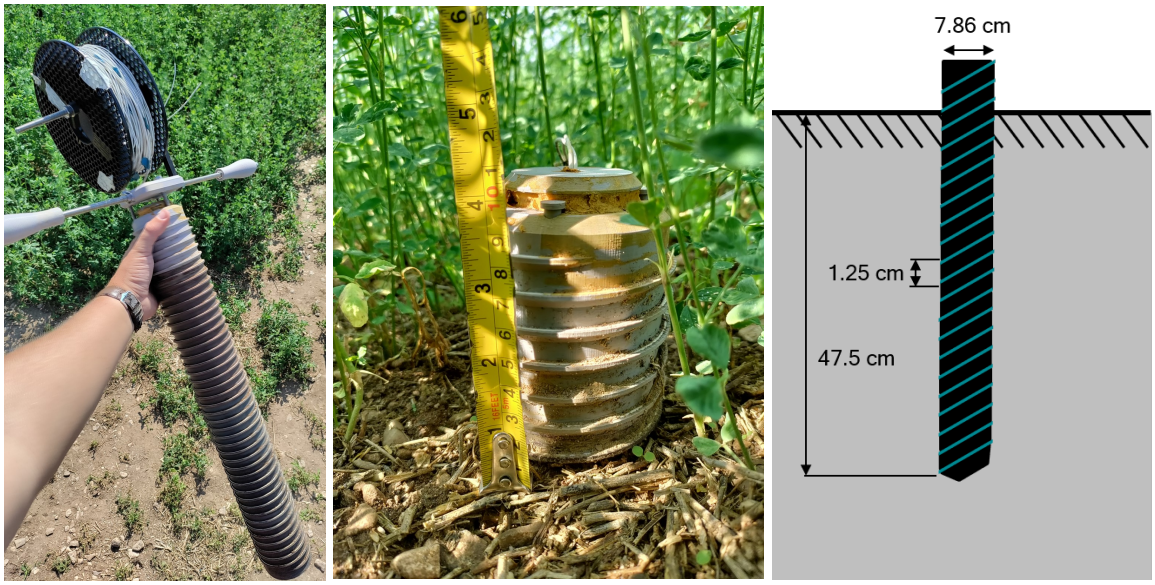

(a) Complete view **(b)** Installed view **(c)** Schematic view

Figure 10.: Overview of the ground coil set-up, which consists of a fiber wrapped around a 3D-printed coil that is installed into the ground. The coil reaches until a depth of 47.5 cm with windings that are spaced 1.25 cm apart and is located next to the WUR soil site within the alfalfa field.

4.1.4. Canopy harp

The canopy harp set-up is centered around two electric fence poles, around which the fiber is winded back and forced in order to create a harp-like shape. The poles are placed 2.5 m apart so that there are approximately 10 data points for each height of the canopy harp. The electric fence poles had hooks at certain heights that were used to route the fiber. At these hooks the fiber was held into place in the same way as was described for the 50 m mast.

The heights of the harp were predetermined by the locations of the hooks of the poles, which are $z = 14$, 22, 30, 41, 53, 63, 74 and 87 cm. In total this results in a harp that spans 2.5 m wide and close to 1 m tall. This configuration is shown in the field in Figure 11a and schematically in Figure 11b.

The conversion from LAF to physical coordinates was done in two steps. First, the locations of the poles along the fiber were recorded using both ice packs and the raw data. After that, each section of fiber between two poles (e.g. each section at a different height) was averaged in order to get one temperature for each of the heights. This results into 8 data points over z for each time period.

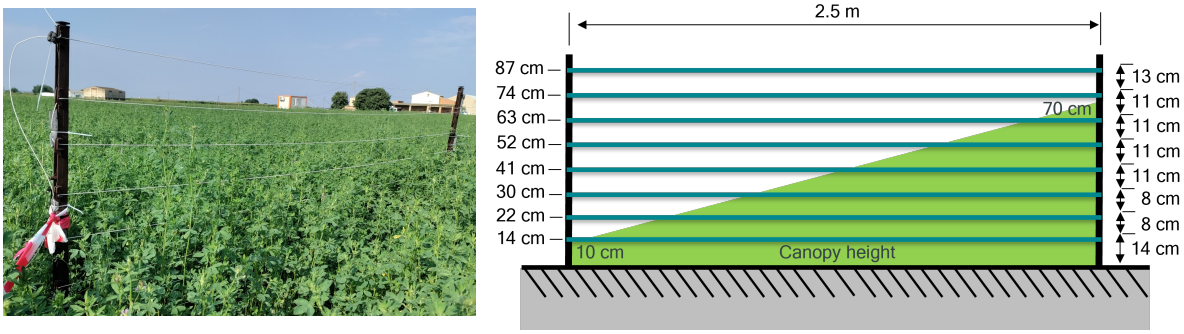

(a) Installed view

(b) Schematic view

Figure 11.: Overview of the canopy harp set-up, with the fiber arranged back and forth between two posts over 2.5 m length in a harp-like fashion, from 14 cm to 87 cm above ground. The recorded canopy height of the growing alfalfa is shown schematically with a green background, which ranges from 10 cm to 70 cm. The set-up is located within this canopy.

4.2. Research approach

4.2.1. Operational overview

A schematic overview of the operation of all set-ups during the campaign is given in Figure 12. This figure shows the time periods in which data was acquired, as well as events that happened during the campaign. A detailed log, including timestamps, on which this figure is based can be found in Appendix C. Within the figure the three vertical set-ups are shown in a timeline, along with a horizontal set-up (the turbulence harp), which will be described in Part 2.

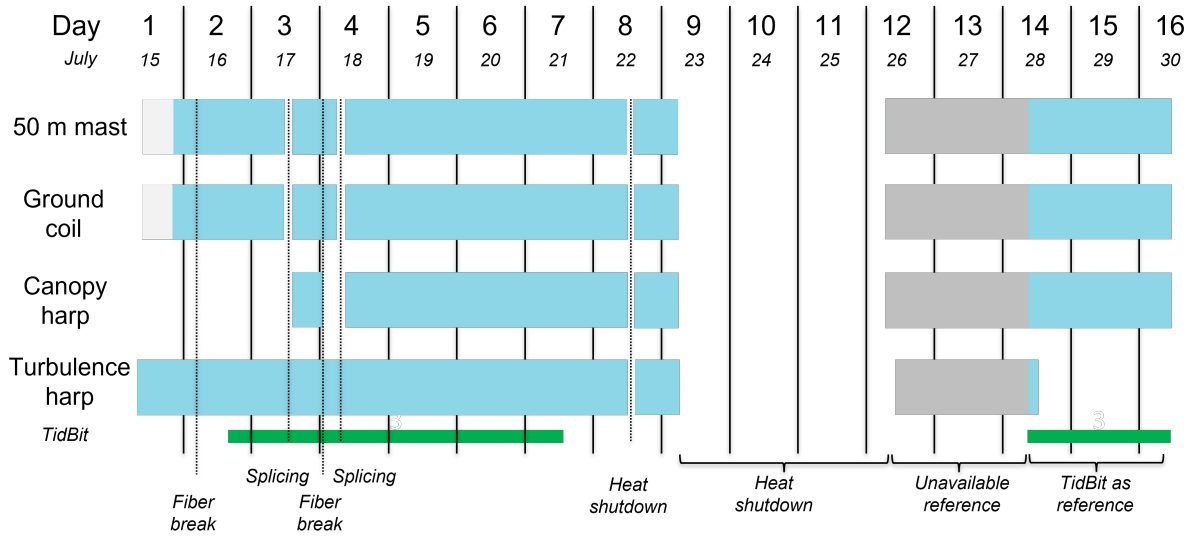

Figure 12.: Overview of operational moments of all set-up during the campaign. Blue areas mark time periods where the set-up was operational. Grey areas mark periods were a set-up was operational, but with issues. Moments of interest during the campaign are also marked.

A double-ended configuration was initially planned and installed on July 15, linking the three setups together. However, this had to be converted into a single-ended configuration (one cable end attached to the DTS computer, rather than both) because of a fiber break on July 16. This change was motivated by the preference to have a continuous time series as long as possible during the campaign using the same settings, rather than to try out different settings during the campaign.

Measurements were briefly interrupted on July 17 to install the canopy harp. A fiber break took down the canopy harp measurements in the night of 17 to 18 July, which was repaired in the morning of July 18. After running continuously for several days, measurements had to be shut down because of a too large power consumption demand resulting from a heat wave. This created gaps in the data timeline between 22 and 26 July.

Between 16 and 21 July, HOBO TidbiT Water Temperature Data Loggers were deployed in the outdoor calibration baths, along with the Pt-100 sensors (marked in green in Figure 12). This was done in order to assess the quality of the TidBit sensors for use as reference sensors. A comparison of the TidBit and the Pt-100 temperature time series can be found in Appendix G.

The same TidBit sensors were used as reference sensor during the last days of the campaign. The Pt-100 sensors used in the rest of the campaign were not available because of damage during a storm on July 26. Upon discovery, the TidBit sensors were deployed as a replacement reference sensor in the calibration baths. Between the unavailability of the Pt-100 sensors and the deployment of the TidBit sensors is a period where the DTS measurements were done without reference sensors (except for the indoor calibration bath). This is marked in grey in Figure 12. There is potential that this part of the time series can be calibrated using the calibration parameters obtained during other times of operation.

4.2.2. Campaign overview

This section gives an overview over the duration of the campaign using DTS time series in order to give a broad overview of the conditions during the campaign. Figure 13 shows this overview using 5-min averaged temperature values from each of the three set-ups. Shown in this figure is the 2 m air temperature, a canopy temperature at z = 0.18 m, and two soil temperatures, one at the surface and one at z = -0.40 m. Also added to Figure 13 is the recorded crop height during the campaign in the bottom figure.

Figure 13 shows the temperature measurements during the growth of the crop along 15 days. The crop growth causes a difference in dynamics across the campaign duration for these four temperature time series. Surface temperature varies strongly in the beginning of the campaign, as the crop is still relatively small at this period, therefore providing little shadow. As the campaign progresses, the amplitude of the surface temperature over the diurnal cycle decreases relative to the 2 m air temperature.

The air temperature at z = 2 m (taken from the 50 m mast) during the campaign varies with maximum temperatures of typically 30 - 35 °C and minimum temperatures of 15 - 20 °C. Canopy temperatures closely follow the 2 m air temperature, but with a dampened maximum temperature and a lower minimum temperature. The temperature within the soil, at z = -0.40 m, changes with a much smaller amplitude than the other temperatures, as can be expected. Looking at the diurnal changes in soil temperature along the campaign, it can be seen that these changes are larger in the beginning of the campaign than in the later part. This difference could be due to the increase in crop height, which has a dampening effect on heat transfer from the atmosphere to the soil. Another observation is the seemingly low temperatures during the last part of the campaign, which could be due to the instrument calibration not being sufficiently accurate to account for longer term changes in calibration parameters.

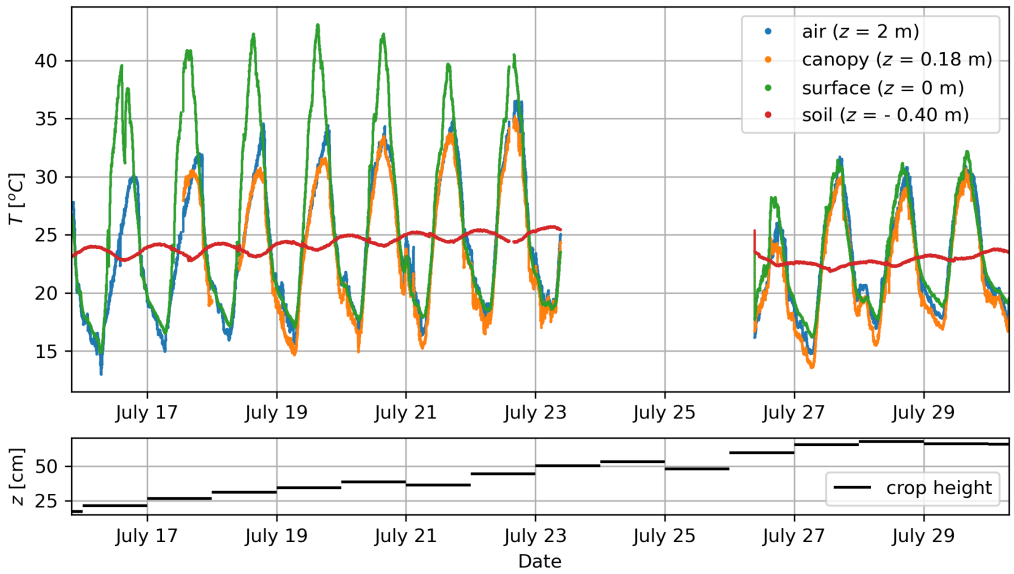

Figure 13.: Crop height and selected temperatures time series along the whole campaign. Time series of temperatures of air (at z = 2 m), canopy (z = 0.18 m), surface (z = 0 m) and soil (z = -0.40 m) are displayed in the upper plot as 5-min averages. In the lower plot, crop height along the campaign is shown.

Figure 14 is an addition to the campaign overview given in Figure 13 which shows the 5-min variance of the four selected time series along the campaign. This figure shows a variance in canopy temperature that is low in the beginning of the campaign (small crop), high halfway the campaign (growing crop that is free to move), and then decreasing again (crop has grown enough to constrict movement in the lower part of the crop). Surface temperature variance is high in the beginning of the campaign and lower in the end of the campaign, which fits the above explanation.

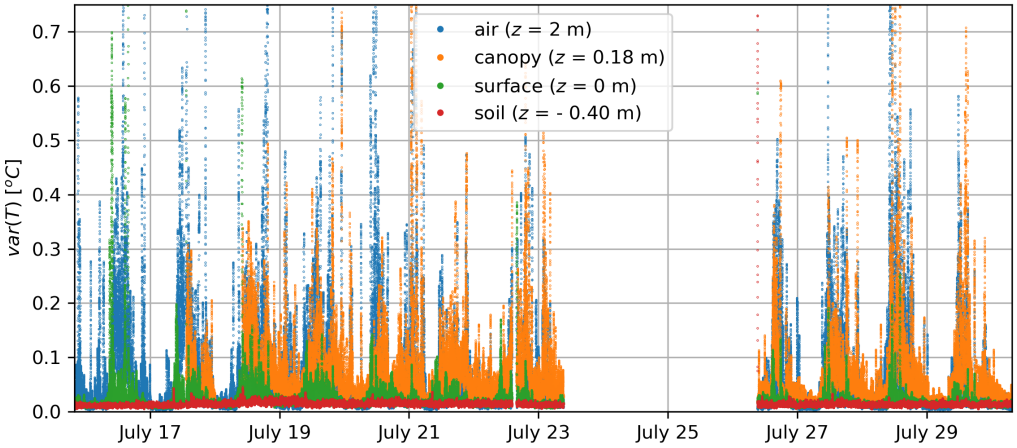

Figure 14.: 5-min variance of selected temperatures along the whole campaign. The variances displayed are temperatures of air (at $z = 2$ m), canopy ($z = 0.18$ m), surface ($z = 0$ m) and soil ($z =$ -0.40 m).

The calibration of the raw measurements into physical temperatures was complicated because of varying temperatures in the calibration baths. The focus of Part 1 for this thesis is on displaying the data that was acquired during the LIAISE campaign. Therefore it was decided to display the temperature data in this part using the calibrated temperatures as were done by the instrument itself, rather than the thorough calibration as done by the available software. Future investigation will have to be done to check these issues and perform a thorough calibration.

5. Results and discussion

5.1. 50 m mast

This section gives an overview of the temperature data as obtained by the 50 m mast. A specific day, July 21, was chosen as a typical day to use as a case for describing the data characteristics. The same figures, but for an alternative day, July 28, can be found in Appendix F. Since the 50 m mast covers a significant amount of vertical distance, the potential temperature θ is used to account for the adiabatic effect with height using the conversion

$$\theta = T + \frac{g}{c_p} z, \tag{1}$$

with g the gravitational constant (9.81 $\mathrm{m\,s^{-2}}$), c_p the heat capacity of air (1004.7 $\mathrm{J\,kg^{-1}\,K^{-1}}$) and z the height in m.

Like classical meteorological mast observations, the data from this mast can be used to create time series of temperatures at different heights. This is shown in Figure 15 for heights of z = 5, 15, 25 and 35 m. Here 5 minute averages are superimposed on the instantaneous 5 second data with solid lines.

A diurnal cycle is visible in the temperature, with highest temperatures found at 17:30 and lowest temperatures at 6:00. During the day, temperatures at different heights closely match each other, which indicates a well-mixed atmosphere (e.g., $\frac{\partial \theta}{\partial z} = 0$ or stable conditions). There is an exception of this around 12:00, where conditions briefly turn stable. During night there is a return to stable conditions because of radiative cooling. The extent of the vertical temperature gradient ($\frac{\partial \theta}{\partial z}$) can vary throughout the night, as for example seen at 2:30 (almost no gradient) and between 6:00 and 8:00 (strong gradient).

To more closely look at these gradients, a relative potential temperature can be plotted. This relative temperature, $\theta - \theta_{1.6}$, is defined as the temperature relative to the lowest data point of the mast at z = 1.6 m. Time series of $\theta - \theta_{1.6}$ are plotted in Figure 16. In this figure it is visible that compared to the lowest point of the mast, the temperatures higher up in the mast are slightly colder (typically 1 K) during the day. During night this is contrasted by warmer temperatures at higher locations, up to 5 K.

The fiber measures temperature across the mast at 25.4 cm intervals, which gives the possibility to create a series of temperature measurements along space as well as time, along the vertical in the z-direction. Several vertical profiles are displayed in Figure 17. Each of these figures contain two temperature profiles, one of the fiber going up and one of it going down. The first and third figures are instantaneous (e.g. 5 second) measurements obtained during night (03:30) and day (15:30) respectively. Here the nighttime profile shows stable conditions with little variations relative to the daytime profile. The daytime profile shows neutral, well-mixed conditions, with considerable variations along the vertical and especially between the upwards and downwards profiles.

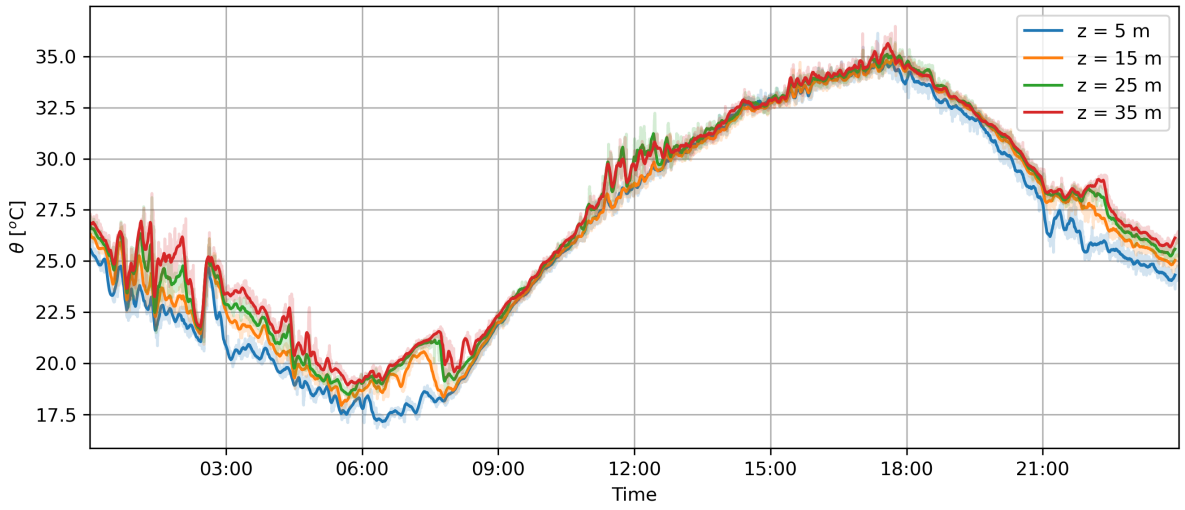

Figure 15.: Diurnal time series for different heights of the mast. Potential temperatures are shown for heights of z = 5, 15, 25 and 35 m during July 21. Bold lines are 5 minute averages, under which the 5 second instantaneous data is shown in transparent. The same plot for a different day, July 28, can be found in Appendix F.

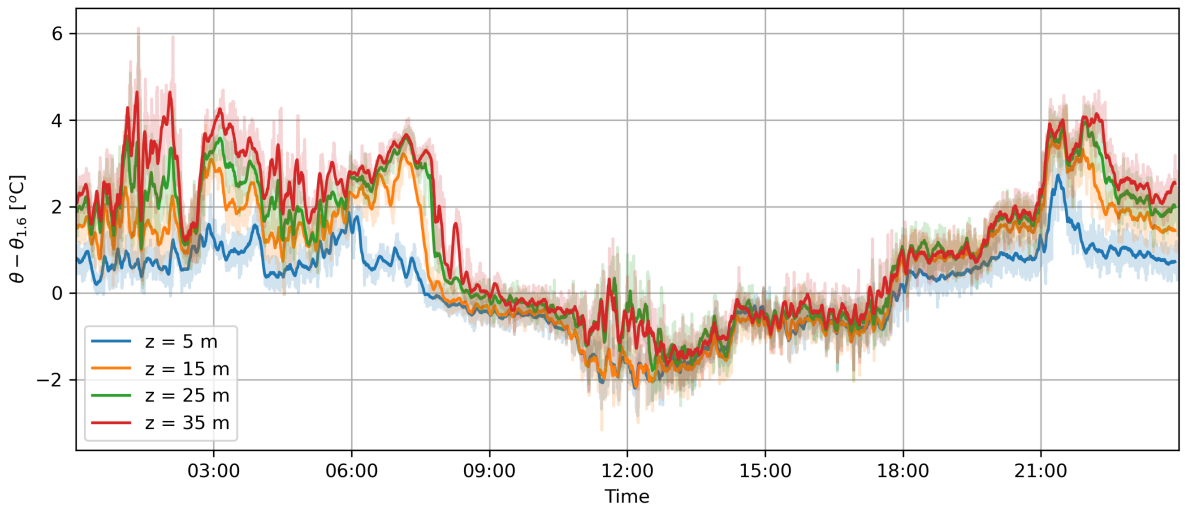

Figure 16.: Relative potential temperatures corresponding to the time series of Figure 15. Positive values indicate stable conditions and negative values unstable conditions. Temperatures are plotted relative to the potential temperature of the lowest point of the mast at z = 1.6 m. Bold lines are 5 minute averages, under which the 5 second instantaneous data is shown in transparent. The same plot for a different day, July 28, can be found in Appendix F.

The differences between the upwards and downwards profiles in Figure 17 are up to 1 K, and have at some points reached up to 2 - 3 K during the campaign. To check the effects of this difference between profiles on the longer term, 1 hour averaged profiles of the nighttime and daytime profiles were made. These were made around the hour of the instantaneous profile (e.g. 3:00-4:00 and 15:00-16:00) and are shown in the second and fourth plots of Figure 17. Noticeable here is a considerable smoothing of the profile along the vertical, as can be expected, since short-term fluctuations are smoothed out. For the nighttime averaged profile slight deviations between the upwards and downwards profile remain.

Differences between the averaged upwards and downwards profiles for daytime are still clearly visible and are up to 0.4 K. This is likely due to a difference in radiative effects for both fibers. The fibers have different orientations relative to the mast and the Sun, so will receive different amounts of shortwave radiation for different times of the day. A fiber could be closer to the mast itself, receiving more longwave radiation, both resulting in a difference in net radiation. Also visible are distinct heights in the profile where temperatures are considerably higher. These hot spots correspond with the locations of the PVC holders of the fiber. The designed heights of the PVC holders are indicated in all plots of Figure 17 with horizontal lines. The hot spots show that the effect of the PVC holder pipes are significant, creating temperature biases of over 1 K. These heights of the profile should therefore be masked out when used for further analysis (for example for determining gradients).

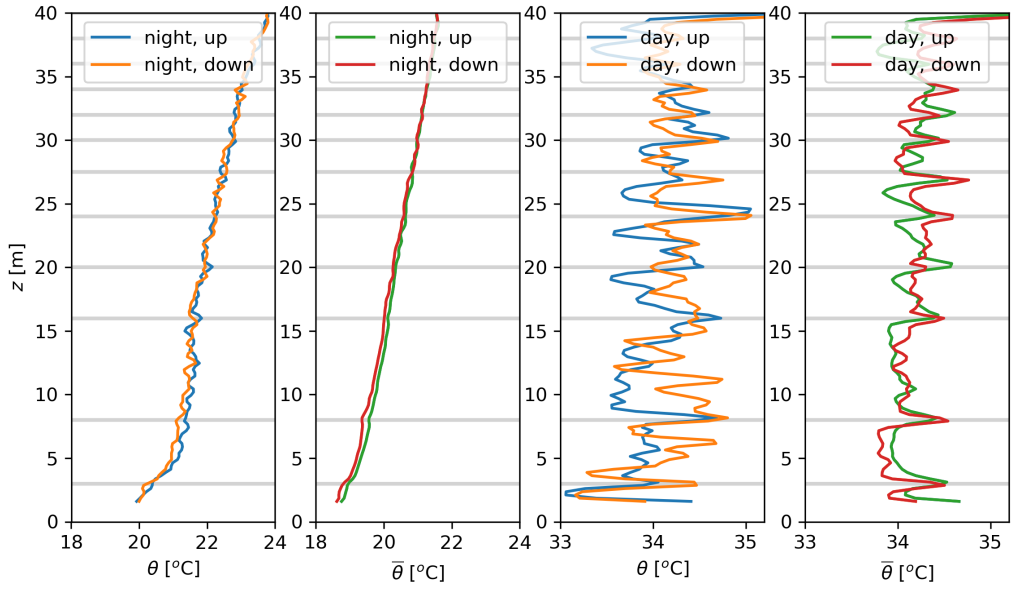

Figure 17.: Instantaneous and 1 hour averaged mast profiles for nighttime and daytime. Instantaneous profiles are given for July 21 3:30 and 15:30, for both the upwards and the downwards stretch of the fiber. Also given are 1 hour averaged $\overline{\theta}$ profiles centered around the instantaneous measurements. Horizontal lines indicate the heights of the PVC fiber holders.

The measurements over the time and space dimensions can be combined to create a two-dimensional image over time and space. Figure 18 shows this two-dimensional data set as a contour plot for all data obtained by the mast during July 21. Temperatures used here are averaged temperatures of both the upwards and downwards fibers ($\theta = (\theta_{up} + \theta_{down})/2$ for each z).

Figure 18 gives information about both the diurnal cycle and the stability during July 21. For example, the effect of radiative cooling can be seen from 21:00 onwards with the vertical temperature gradient becoming positive. The temperature bias created by the PVC pipe holders is clearly visibly during daytime as horizontal lines of enhanced temperature. During night uniform air masses of different temperatures are moving past the mast from 0:00 to 3:00, after which an inversion is formed. Around 8:00 is an event that will be highlighted later this section in Figure 20.

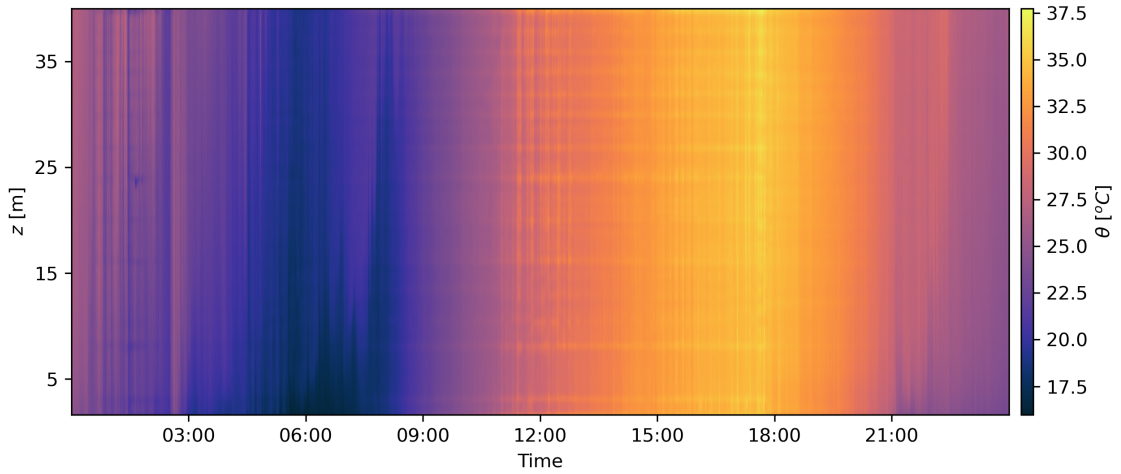

Figure 18.: Contour plot over height and time of potential temperature. Temperatures are taken as averages between the upwards and downwards fiber. Temperature values are indicated by a colourbar going from blue to white to red with increasing temperatures.

For Figure 18 the average temperature of the upwards and downwards fiber was taken. To investigate the effect of this choice, the temperature difference between the two fibers $\theta_{up} - \theta_{down}$ is plotted in Figure 19 for the same period as Figure 18. This figure also supports the analysis done using Figure 17, expanding on the difference in fiber temperature from instantaneous measurements to measurements over time.

Several features are visible in this figure, both in time and space. During night $\theta_{up} - \theta_{down}$ is typically low and slightly positive, which could be explained by the lack of Solar radiation. An exception to this is the period around 2:00, where air masses of different temperatures moving around create larger $\theta_{up} - \theta_{down}$. This is a feature that was only found during July 21, typically nighttime $\theta_{up} - \theta_{down}$ is low.

During daytime values of $\theta_{up} - \theta_{down}$ increase, varying both over time and space. Structural differences over time can be found for distinct heights, which is likely caused by a difference in net radiation between the two fibers. Two distinct vertical features are seen at 10:30 and at 19:30. The reason for this is yet unknown, but this feature can be found in some different days at similar times. There is a strong and consistent oscillation along all heights at 15:00, with first high, then low relative temperatures. It is possible that this is a transition period where first only the upwards fiber is in direct sunlight, which then flips around to the downwards fiber by the movement of the Sun.

To compare the consistency of differences in temperature across the campaign period, a second plot is included in Figure 19, which displays the mean for all temperature differences across the vertical, $\overline{[\theta_{up} - \theta_{down}]}_z$. In this way, a time series is created that can act as a signature describing the effect of using two fibers. Between campaign days, these signatures typically roughly correspond. There are low values during nighttime, higher values during daytime and there are two distinct features; the oscillation

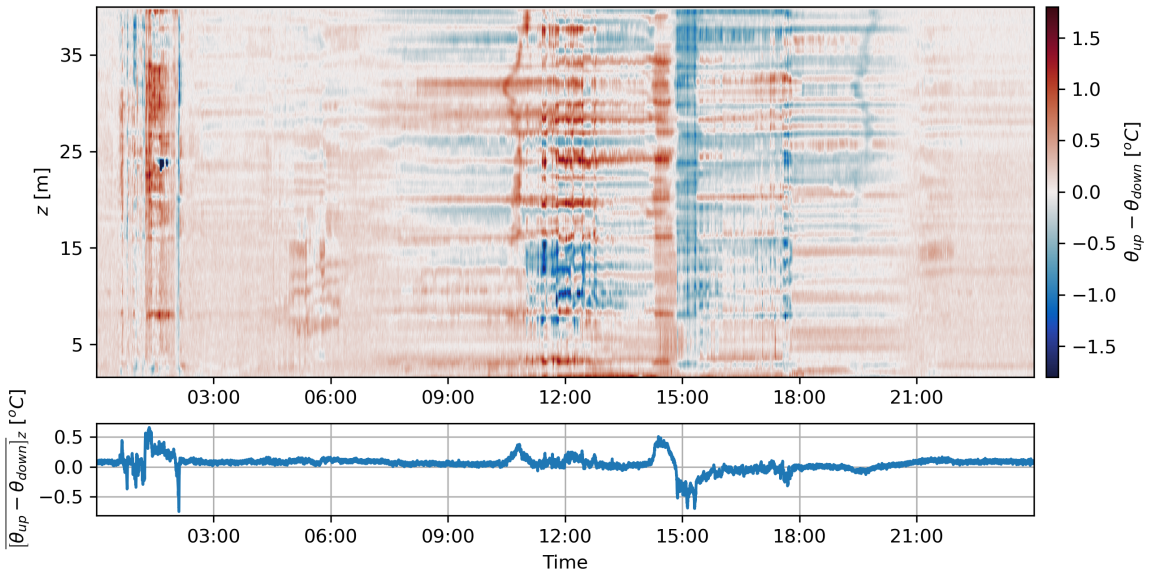

Figure 19.: Contour plot of temperature difference between the upwards and downwards fibers. The lower figure shows the mean temperature difference along the vertical.

around 15:00 and the enhanced values that correspond to the distinct features. The consistency of these features along the campaign indicate that there are mechanisms that drive these. Therefore future investigation into these features is recommended.

Alternative to full day contour plots, zoomed-in contour plots give the option of looking are temperature data at smaller scales. An example of this is shown in Figure 20, which is a zoom-in of Figure 18 between 6:00 and 9:00. This is the period at which the Sun comes up, radiative heating of the surface during the campaign typically starts at 7:30. However, here there is a persistent cold layer at lower heights that lasts until 8:30. This is an anomaly with the rest of the campaign, as can be seen by for example comparing it to the figures of July 28 in Appendix F.

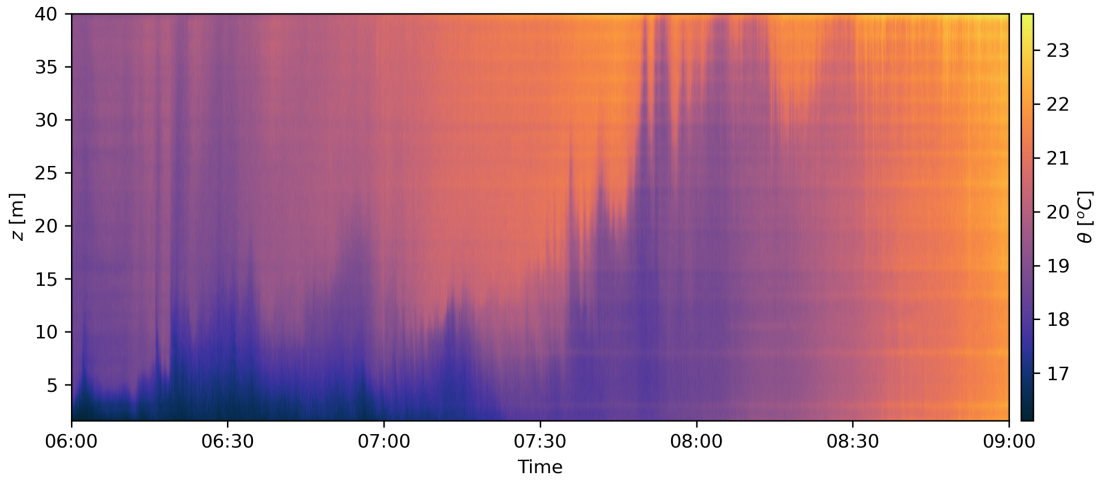

Figure 20.: Contour plot zoom-in of Figure 18, showing two distinct air masses with an abrupt temperature change over the vertical.

Figure 20 shows the unique capability of distributed temperature sensing in detecting distinct events. Here it shows two air masses with a 4 K temperature difference existing between 7:00 and 8:00. Since at this time of day convection has not yet started, this is likely due to a warmer air mass moving in by advection. The temperature change from one air mass to the other is abrupt, at 7:15 for example taking only 1 meter, which would likely not have been picked up using conventional instrumentation. For further analysis, detecting these interesting spatio-temporal events on smaller scale is recommended. One example of this could be the different air masses moving around between 0:00 and 3:00 in Figure 18.

5.2. Ground coil

The ground coil set-up has a much finer vertical spatial resolution than the other set-ups because of the winding of the fiber around the coil. This creates detailed smooth vertical profiles of soil temperatures, as will be described in this section. Besides that, time series of the soil temperatures will also be given for a typical day and for a rainy day.

Figure 21 shows the vertical temperature profile of the soil as a 1-hour average spaced 3 hours apart. The profiles in Figure 21 show the temperature dynamics in the soil over a diurnal cycle. At nighttime, the top of the soil has the lowest temperature because of radiative cooling during the night, and in the layer below the top soil there still is heat stored from the previous day. As night progresses, the top soil keeps radiatively cooling. Heat that was stored in the layer below the surface gets transported towards the surface, causing that layer to cool down. Once nighttime turns into daytime the surface rapidly heats up, creating a strong temperature gradient in opposite direction as in nighttime. As the day progresses, this temperature gradient penetrates deeper, giving off heat to deeper parts of the soil. After direct solar radiation disappears, the cycle starts again with the surface cooling radiatively. This diurnal temperature cycle in the soil seems to be captured completely within the 45 cm depth of the ground coil, as at this depth the temperature varies negligibly.

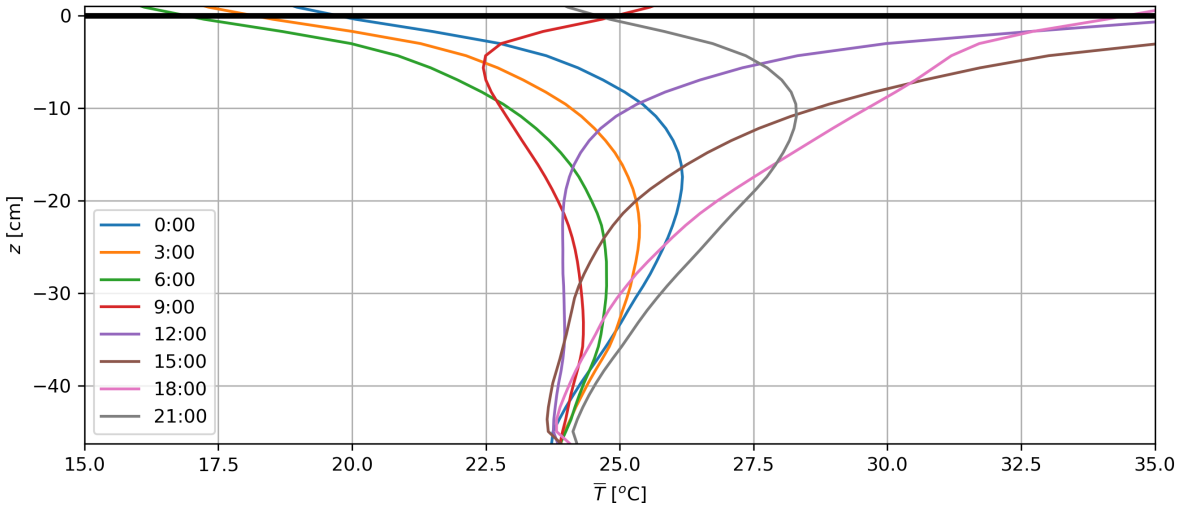

Figure 21.: Ground coil 1-hour averaged profiles spaced apart by three hours during July 16. The solid black line marks the surface level. Each profile is marked by a different colour and is a 1-hour average starting at the indicated time in the legend.

Besides profiles, time series of soil temperatures can also be made using data from this set-up. Figure 22 is one example of a diurnal time series obtained on July 28, which shows temperatures at a depth of $z = 3$, 10, 20, 40 cm. These depths were chosen as they represent an approximately logarithmic scale, which theoretically would give a linear spacing between the time series. Similar to the mast time series, the bold line marks a 5 minute averaged temperature, behind which the instantaneous measurements are marked in a more transparent colour.

The time series shown in Figure 22 show a diurnal cycle which is stronger in amplitude for decreasing depth. Besides that, the variation in temperatures is strongest at the surface, and decreases downward with depth. A phase delay of the diurnal cycle is visible with increasing depth. These three characteristics are typically what would be expected for a theoretical description of a diurnal cycle in soil temperatures (Moene and Van Dam, 2014).

An alternative time series of soil temperature is shown in Figure 23 for July 26. During the night preceding this day there was a storm event with 33 mm of rain. This caused a disruption in measurements, which were resumed again at 9:10, resulting in this figure. After the storm event the field was quite wet, resulting in low surface temperatures. The temperatures between a depth of 0 and 10 cm were uniform within 1 K until 14:00. After this, the surface and the canopy had dried out, resulting in rapidly increasing surface temperatures. Also visible is that the temperatures at larger depth follow this trend, with a dampened amplitude and a delay in phase. It should be taken into account that a wetter soil will also create a difference in thermal conductivity of the soil, which is not accounted for here, strictly looking at the DTS measurements.

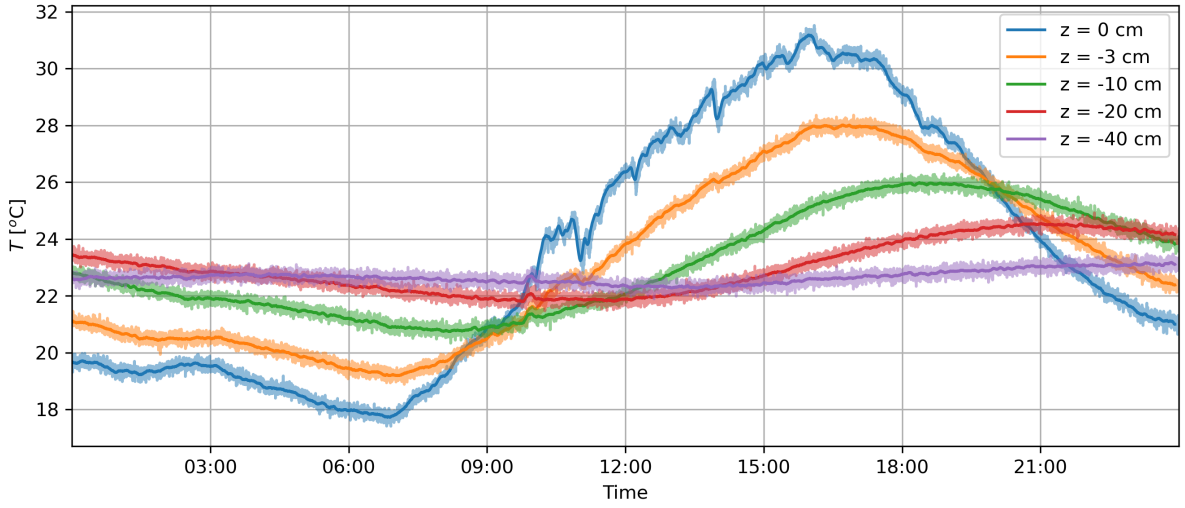

Figure 22.: Time series of soil temperatures for different depths during July 28. Temperature series are shown for depths of $z = 3$, 10, 20, 40 cm. The bold lines show 5 minute averaged of temperature, which are superimposed on the instantaneous measurements in a more transparent colour.

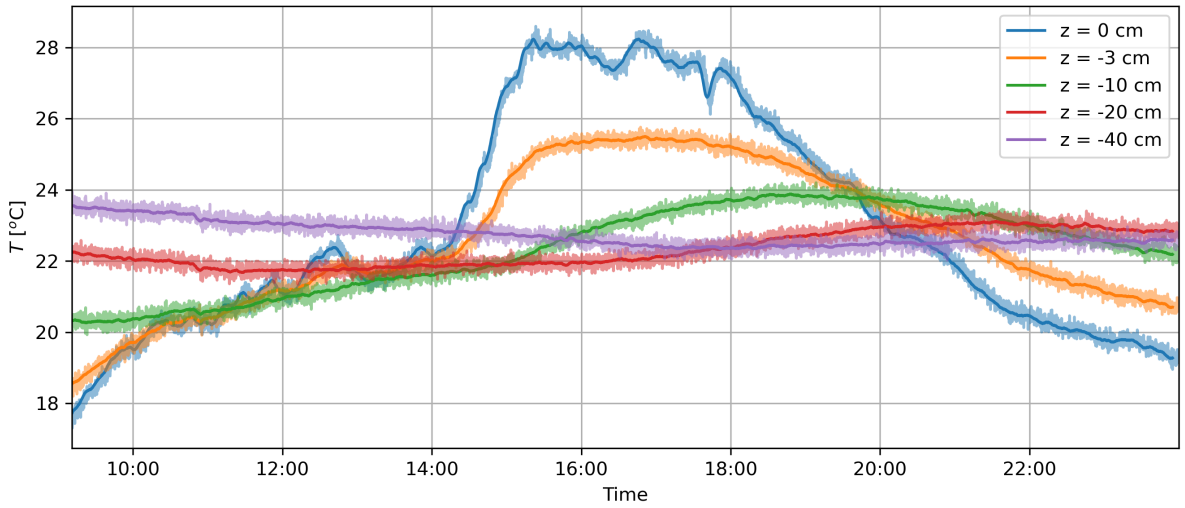

Figure 23.: Time series of soil temperatures for different depths during July 26, after a storm event. Temperature series are shown for depths of $z = 3$, 10, 20, 40 cm. The bold lines show 5 minute averaged of temperature, which are superimposed on the instantaneous measurements in a more transparent colour.

5.3. Canopy harp

For the canopy harp set-up, this section contains a description of canopy harp contour plots on two different time scales. First, two figures of one hour length are shown to display the temperature gradients in the canopy during different parts of the day. Second, two figures of containing three days of temperature data, spaced a week apart, are discussed. In this way, differences in temperature dynamics on a longer time scale, caused by crop growth, can be investigated.

Figures 24 and 25 show two 1-hour snapshots of the canopy during July 28, when crop height was 68.1 cm. Figure 24 shows the transition between nighttime and daytime, when after 8:00 solar radiation starts heating up the crop. Here is it visible that the crop does not heat up evenly. The last place to heat up seems to be the top of the canopy, while the first place to heat up is the middle part of the canopy. In Figure 25 two different regimes can be found. The first is where the top part of the crop and the air is warmer than the lower part of the crop (before 16:07). After this the situation reverses and top part is typically colder than the lower part of the crop. This shows the insulating effect of the crop, where temperature changes in the air are quickly transported into the top 15 cm of the canopy, but not as quickly further into the canopy.

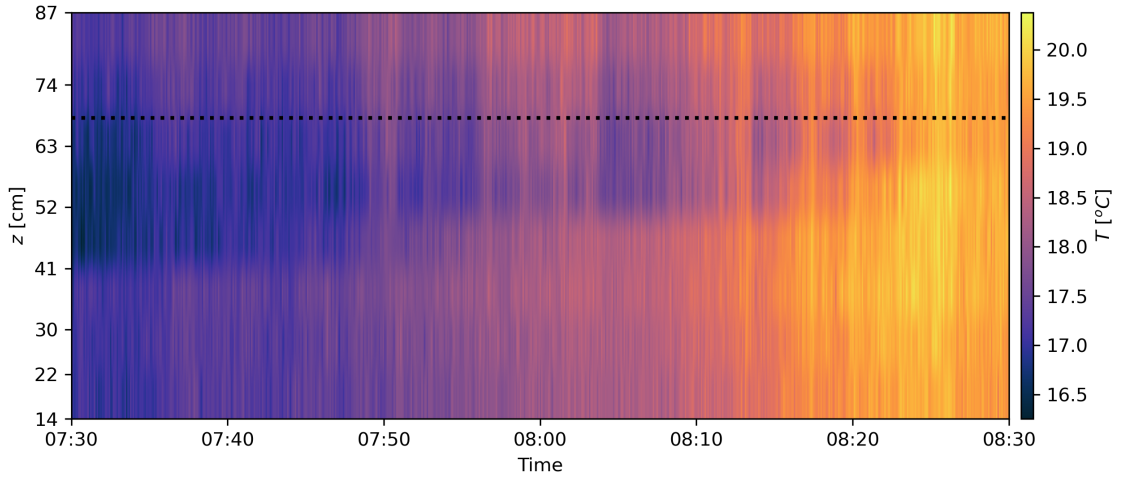

Figure 24.: Canopy temperature during sunrise for 28 July 7:30-8:30. Measured crop height is indicated by a dashed line.

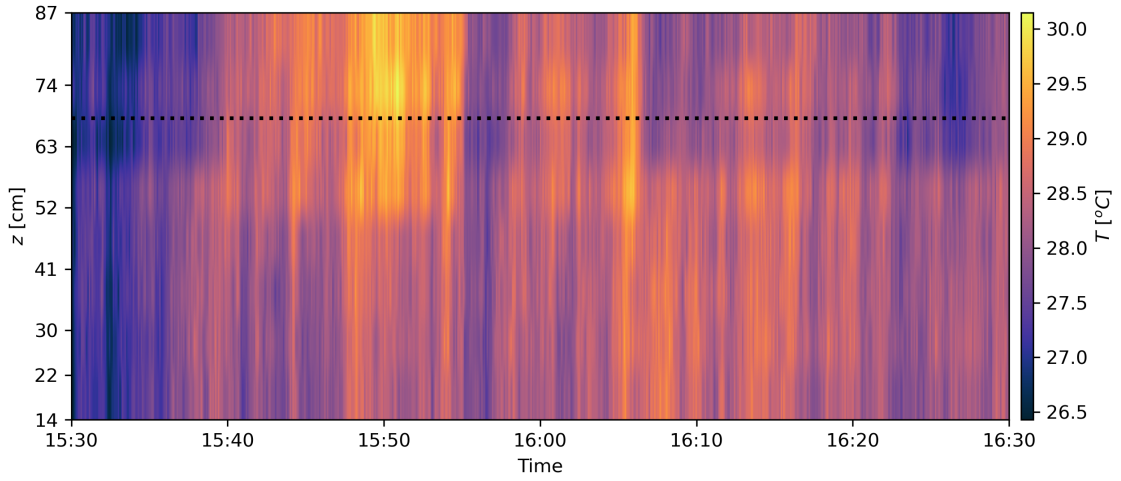

Figure 25.: Canopy temperature during the afternoon for 28 July 15:30-16:30. Measured crop height is indicated by a dashed line.

Since the temperature profile in the crop is influenced by the crop height, it is interesting to look at temperature data over a time of multiple days. Figure 26 and Figure 27 show two contour plots of two different three day periods, 19-21 July and 27-29 July. The data shown in these two figures is spaced apart by a week, during which the canopy grew by approximately 40 cm from approximately 35 cm to 65 cm.

The temperature difference within the canopy is small compared to the diurnal change in temperature. Therefore is is more illustrative to look at a local temperature relative to a diurnal temperature. This was done for both Figures 26 and 27. The diurnal temperature is taken as the average temperature across the canopy profile. This diurnal temperature $\bar{T}_z$, is shown in the bottom plot of both figures in black. The top part of both figures contain the temperature difference within the canopy, relative to this $\bar{T}_z$.

Both figures show the same characteristics following the diurnal cycle. At night, the crop is relatively warm, while during the day it is relatively cool. This demonstrates the insulating effect of the crop that was mentioned earlier. The transition from nighttime to daytime regimes show different structures. For the smaller canopy (Figure 26) the transition between a relatively warm (nighttime) or relatively cold canopy (daytime) is very sudden. With larger canopy (Figure 27) this transition is more gradual over time and merges into the next day. Two potential reason for this could be the canopy being denser and therefore having more capacity to keep its heat, and the canopy evaporating more on the last days of the campaign.

A recommendation from this set-up would be to look at the extent of the insulation effect of the crop on the land-surface interaction between the soil and the atmosphere. Also it could be an option to look into the difference in temperature variance within the crop.

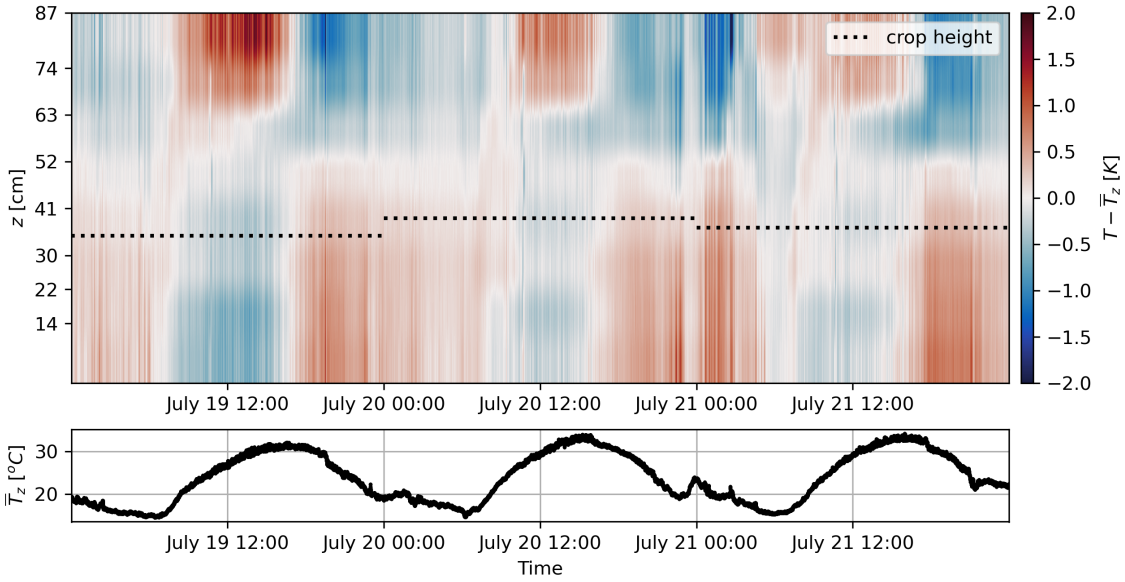

Figure 26.: Three consecutive days of relative canopy temperatures for smaller canopy, early in the campaign. Temperatures plotted in the top plot are relative to the current mean temperature along the vertical $\overline{T_z}$. This mean temperature is displayed in the bottom plot. Dashed black lines indicate recorded canopy height of that day.

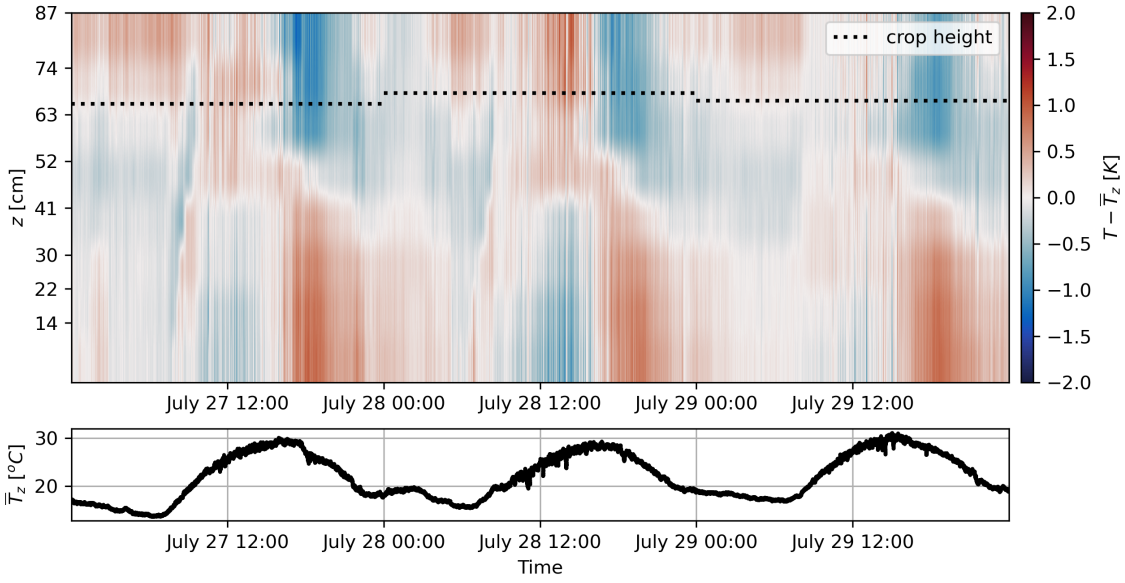

Figure 27.: Three consecutive days of relative canopy temperatures for larger canopy, late in the campaign. Temperatures plotted in the top plot are relative to the current mean temperature along the vertical $\overline{T_z}$. This mean temperature is displayed in the bottom plot. Dashed black lines indicate recorded canopy height of that day.

6. Discussion of Part 1

The discussion in this chapter is an addition to the points discussed in the previous sections while presenting the results. Topics touched upon in Chapter 5 concerned mainly the interpretation of the data, while here the discussion focusses mostly on the experiment itself and choices that were made during the campaign. Part of this discussion also concerns the design of the turbulence harp treated in Part 2, since there are similarities in design and the experiments.

6.1. Calibration

First addressed should be the complications regarding calibration. A thorough calibration of the raw power measurements was left out because using the reference data from this campaign did not result in a valid calibration using readily-available calibration routines. Calibration turned out to increase, rather than decrease, the temperature variance, Beside that, artificial features were created in DTS temperature series that could not be found in reference datasets. Likely these features are caused by the drift in temperature over time of the outdoor calibration baths. The baths were influenced by the outdoor environment and this might have created reference time series that are not stable enough for calibration over the standard 30-minute periods. An display of this environmental drift can be found in the Appendix in for example Figures 69 and 70.

In planning the experiment, it was expected that the temperature difference needed between the two beds could be obtained by keeping one bath in the shade and one in the sun. This assumption turned out to be wrong, as the styrofoam baths used slowly heated up over time and their insulating properties made radiative cooling not adequate to keep up with this warming. Therefore especially the cold bath slowly heated up, converging the temperatures between both baths.

In order to keep sufficient temperature difference between the calibration baths, ice packs were applied to the cold calibration bath daily. This created very sharp temperature drops in the bath (Figure 69) that rendered the results obtained in the 30 to 60 minute interval around this moment completely invalid using the current calibration routine. Because of the environmental influence on the temperature and the application of ice packs, the temperature difference between both baths was also not constant and sometimes approached zero or opposite values. This also effects the calibration quality with introduction of artificial features.

No literature was found that readily treats how to deal with the issues described above concerning non-stable references. Experiments are known that have used similar set-ups, but these results have either not been published or the extent of their reference temperature fluctuations are not known. Several attempts have been made in this work to find solutions using the existing DTSCALIBRATION and PYFOCS software, by changing reference sections and calibration intervals. These attempts have not conclusively produced acceptable results.

Since the goal of this thesis leaned more towards interpretation and analysis of DTS data, rather than investigating calibration routines, it was chosen to use the instrument-specified temperatures. The instrument calculates temperature directly from each measurement using an internal reference coil to estimate the calibration parameters. This approach is the historical approach of getting temperature data (Selker et al., 2006; Tyler et al., 2009), but more recent research has found that this method is not necessarily as accurate as desired (des Tombe et al., 2020; Hausner et al., 2011). The instrument-specified temperatures are however still values that represent physical temperature, albeit with potential offset and scaling

errors. Therefore using these temperatures can still create an overview of the capabilities of DTS for SEB measurement (Part 1) or be used for turbulence analysis using relative temperatures (Part 2).

Further use of this data set for research purposes should be preceded by a thorough investigation into the potential for further calibration. Either the current (instrument) calibration routine could be used, or further attempts into applying another routine (e.g., DTSCALIBRATION) should be made. In case of the first option, a critical look should be given to the appointed uncertainties of the data set. This can perhaps be quantified by comparing results obtained from a limited part of the data set calibrated using modern routines. For the second option, analysis can be done to try to find typical calibration parameters for the whole campaign using the most suitable parts of the campaign for calibration.

6.2. Reference baths

As the physical part of the calibration strategy, the reference baths should also also be mentioned. The reference baths are idealized as a homogeneously mixed volume of water which is in constant temperature and in thermal equilibrium with the fiber. Looking at the deployment of the reference baths in the campaign (Figure 6), several remarks can be made about this idealized scenario. The fiber is run through the outdoor baths for each section of fiber, so at least once for each set-up. This results in a significant length of fiber present in the bath (Figure 6c), which inevitably causes the fibers to touch each other, rather then float freely in the water. Adding to the crowdedness are the ice packs in case of the cold bath. As a result, mixing by the pump was obstructed and which hindered a constant temperature throughout the baths.

There are some parts of the reference section that show a consistently small bias in temperature because of not being in free contact with the water, either by touching too much other objects or by insufficient mixing. As stated by Tyler et al. (2009) and confirmed by Hausner et al. (2011) at least 10 sample points are needed to remove noise sufficiently within the calibration, which for this experiment results in at least 15 m of fiber. During installation it was decided to aim for 10 m of fiber per reference section, in order to have spare length in case of fiber break. While this is a sensible decision in terms of redundancy, this was also a main cause for the crowdedness.

In order to create a more homogeneous bath temperature, less spare fiber length could be used. Alternatively, fiber-glass mesh could be placed in the calibration baths to create more vertical space for the fiber to be placed. A recently published development is a new type of calibration baths using solid copper blocks as reference sections (Thomas et al., 2022). This method uses a metal mass which is kept at a constant temperature within 0.04 K and insulated from the environmental temperature. The fiber is then clamped into the metal block, and less than 10 sample points are needed to manage calibration noise. The technique works especially well for field locations which have a large temperature difference between the environment and the desired calibration temperature, which would make it suitable for the hot Spanish climate of this campaign.

In recent years, novel applications for using DTS in environmental science has shifted from hydrology (see for example Selker et al. (2006)) towards atmospheric and turbulence measurements (for example (Izett et al., 2019)). This has been made possible by developments in fiber application, data processing and experimental design, but the calibration approach has largely remained the same. For hydrological purposes, requirements for time and spatial scales are often looser than for turbulence analysis. Considering this, a critical look into the use of water calibration baths for turbulence and atmospheric measurements is certainly recommended, with perhaps a solid copper solution being a more rigid alternative (Thomas et al., 2022).

The TidBit sensors that were brought for calibration were at first considered redundant during the campaign, since it was arranged that better Pt-100 sensors could be used from WUR. The TidBits were still deployed to have an option to verify their results against the Pt-100 for calibration. A comparison between the Pt-100 and TidBit sensors is given in Appendix G. For the validation test it should be noted that the measurement interval was put at 5 minute resolution for the TidBits against the 10 s Pt-100

resolution to save battery. This should be prevented in future use, considering the costs of a campaign and other instruments involved as opposed to a TidBit.

Bringing the TidBit loggers did turn out to be beneficial, because of the loss of the Pt-100 sensors during a storm. The TidBit loggers could then be used as replacement reference sensors during the last three days of the campaign so that there was a least some reference material. However it is not recommended to use the TidBit loggers for further atmospheric DTS measurements. It was found (Appendix G) that the TidBit loggers have a time lag of 3 minutes compared to the Pt-100 during the ice pack switch. This long time response renders the TidBit unusable for calibration of any DTS measurements that desire time resolution within a 5 minute scale.

6.3. Design and operation of the experiment

The configuration of this experiment ended up being single-ended, meaning that the fiber is connected with one end to the DTS computer and then ran into the field. An alternative configuration configuration is double-ended, in which the fiber is connected to the DTS computer by both ends, therefore creating a loop across the field. Both ends of the fiber being connected to the computer means that the fiber can be probed from both directions, allowing to correct for effects of differential attenuation, such as bends and splices (Van De Giesen et al., 2012). This reduces uncertainties, but also comes with a speed disadvantage however; probing in both directions doubles the sampling time.

The focus of the experiment in this part is on collecting measurements to supplement SEB measurements, which would put the demand for low uncertainties ahead of fast sampling speed. For a double-ended configuration the minimum sampling time is 10 s, which is adequate for most intended purposes. Another consideration is the distribution of noise along the cable. For single-ended measurements, noise increases linearly along the fiber, while for double-ended noise is highest at the ends of the fiber and lowest in the middle section (Van De Giesen et al., 2012).

Both the reduction in uncertainty and the distribution of noise along the fiber are arguments for using the double-ended configuration in these set-ups. Forming the fiber path from Figure 7 into a loop by connecting the canopy harp to the DTS computer would have put the 50 m mast and especially the ground coil in the middle of the fiber path. That would put the lowest uncertainty at these set-ups, while the highest noise would be at the sections connecting the set-ups to the computer, which would be ideal.

The double-ended configuration was the original design of this experiment and was also constructed in the field. However, due to a fiber break in the returning fiber and difficulties in getting the double-ended path configured in the acquisition software, it was decided to switch to a single-ended configuration. Repairing the fiber would require significant effort, which along with the issues in getting data acquisition operational, could have taken one or two days during the campaign, with no guarantee of it working. Therefore the decision was made to instead measure with a single-ended measurements, so that a dataset could be created that is consistent and has a long coverage in time.

The use of the single-ended configuration means that uncertainty increases along the fiber length, so that the mast has lowest uncertainty and the canopy harp has highest uncertainty (see Figure 55). Potentially this raises uncertainties of the ground coil and the canopy harp above 0.3 K for a 5 s measurement. However, since the noise drops with the square root of measurement points, averaging over time can significantly reduce this large uncertainty. In case the temperature of interest is 5-min averaged, the noise drops to $1/\sqrt{60} = 12\%$. The availability of four reference sections for the ground coil can also contribute in decreasing uncertainty.

The time available for installing all DTS experiments was limited to a quite tight 2.5 days. Besides this, the uncertainty created by the Covid-19 pandemic caused preparations to be rather hasty and DTS operation experience at the campaign to be limited. Considering this, the rigidity and stability of the installed set-ups is something that can be commended. Over the campaign duration, we have been able to measure almost continuously, apart from being offline for splicing and the precautionary heatwave

shutdown (see also Figure 12). Securing and fastening the fiber was done thoroughly (Figure 57), resulting in negligible slippage and little damage to the fiber. Three fiber breaks have occurred, none of which caused one of the main set-ups to be offline for an extended amount of time. A full week of measurements are available in the first week of the campaign, with the turbulence harp having a continuous time series for 8 days.

Increasing temperatures halfway the campaign put additional strain on the power consumption of the research site. The cabin which housed the DTS computers was air-conditioned in order to keep the electronics and the researchers at a comfortable temperature. To keep the instrumentation running, power consumption had to be cut down and therefore the air-conditioning was shut down. After this, the DTS computers were shut down to prevent damage by high temperatures. Considering that cabin temperatures ranged typically from 20 °C to 35 °C, as displayed in Figure 76, it can be asked whether this was a necessity. The DTS components in the computer would have been influenced by the changing temperatures, but this could have been compensated for with external calibration (Hausner et al., 2011; Thomas et al., 2022). It should be noted that this would have affected the results as presented in this part, as it would have influenced internal calibration.

Lastly, some remarks concerning each three of the set-ups. For the 50 m mast, radiative effects create significant biases on the fiber temperature. As illustrated in Figure 19, temperature differences between the two fibers can range up to 0.5 K, of which a significant portion can likely be attributed to the fibers being exposed to direct Solar radiation and being subject to shade. Neilson et al. (2008) has found that the bias in fibers (submerged directly below a water surface) exposed to direct Solar radiation can be up to 0.2 K and Schilperoort et al. (2018) found a bias of up to 3 K for exposed fibers installed in a mast. Installing a radiation shield, consisting of gauze that blocks direct radiation, as is done in Schilperoort et al. (2018) can remove these biases to under 1 K and is recommended for future use.

An analysis on the current data set can still be done to quantify and remove the influence of direct radiation. Since the position of the fibers relative to the mast is known, a mask can be made using the Solar position to determine whether a fiber is shaded. Subtracting the shaded temperatures from the temperatures exposed to direct Sunlight can then give a figure for a Solar bias, which can then be corrected for the exposed temperatures.

The ground coil is a set-up that has previously been used successfully in this configuration (Schilperoort, 2022). For the ground coil attention should always be paid as to whether there is sufficient contact with the soil to allow for a representative thermal conductivity. Since the development of the ground coil, several campaigns have been completed using this set-up. A potentially interesting research question regarding the use of the ground coil as a profiling sensor is to compare the temperature data measured in these campaigns to reference sensors to characterize its performance and detect potential biases.

The canopy harp has a limited extent from a DTS point of view, having 8 averaged data points for each time instance. It does however produce a large amount of measurements compared to conventional sensors. Also present during the campaign was a canopy profiler, which measured temperature at several heights in the canopy. An interesting next step for this set-up would be to compare the results from both data sets and see whether they can complement each other.

7. Conclusions of Part 1

The aim of Part 1 was to give an insight into the potential for distributed temperature sensing to be used in determining temperature profiles in air, vegetation and soil. To this end, results were displayed from a 40 m atmospheric profile, a soil profile up to -0.45 m and an in-canopy profile. The results confirm that it is possible to use DTS to obtain temperature profiles within a surface energy balance context.

Land-surface interactions can be characterized by using the large number of spatial measurements available from the three set-ups of Part 1. Semi-continuous profiles of ground heat dynamics were measured, showing the effect of surface heating on the surface. Atmospheric events such as advecting air masses at different heights and drifting uniform nighttime air masses were detected. The insulating properties of a canopy were displayed, as well as change of behaviour in insulation as the canopy grows.

The additional information that DTS can provide in determining the surface energy budget lies in the capability of measuring in space and time simultaneously. The 1 cm vertical resolution of the ground coil creates a temperature gradient for potential better determination of ground heat fluxes. Sharp temperature changes in the air can be detected over space and time in the air. In-canopy measurements can be used to quantify the insulating effect of the canopy on heat exchange to the soil. This additional information can be used to supplement the determination of the surface energy balance, potentially helping to find a better closure in the budget.

Issues using reference sensors and applying calibration routines limit the accuracy of the current data set. Temperature values in this data set can have offsets of several tenths compared to absolute temperature. Further research into either applying a calibration routine or quantifying current uncertainties can make this data set suitable for sharing. Of the 15-day during campaign, 12 days were measured. The main limitations in operations were the shutdown during a heatwave and the lack of available reference sensors. Radiative effects have been found to create 0.5 K biases in the atmospheric measurements.

Future recommendations are to first investigate the options concerning calibration and quantifying the uncertainties of the data set. Afterwards, the three set-ups have potential for further research. The 50 m mast needs to be analysed for radiative effects and can then be used as a supplement to conventional measurements and the lower part of balloon soundings conducted during the campaign. An estimation of ground heat flux can be made with the ground coil and compared to reference sensors. The canopy harp can be used to quantify the insulating effect of the canopy on the soil.

Part 2: Turbulence analysis of temperature profiles

Part 2 covers an analysis on turbulence by looking at temperature fluctuations over time and over horizontal space. For this a DTS set-up called the turbulence harp is used, which extends 2 m vertically and 70 m horizontally. The goal of this part is to answer the question

Can distributed temperature sensing be used to resolve temperature turbulence values over time and space?

To give an answer to this question, it is split up into several subquestions

- *How do structure parameters of temperature determined using DTS time series compare to a novel method of determining structure parameters using spatial data?*
- *How well do both methods using the definition of C_T^2 and using the turbulent temperature spectrum work for DTS temperature data?*
- *What is the correlation between temperature turbulence parameters obtained from DTS compared to those obtained from a sonic anemometer?*

8. Theory

8.1. Turbulence description

Atmospheric turbulence is the chaotic and irregular movement of air in space and time. It is mostly produced by wind shear and surface heating at its largest scales and dissipated by viscous forces into heat on its smallest scales. Because of its unreproducible nature, turbulent flows can only be described in a statistical way (Moene and Van Dam, 2014). For this, Reynold decomposition is used. This splits a scalar value q (such as temperature, wind or humidity) into a component along the average flow, $\overline{q}$, and a deviation from that average flow q', so that

$$q = \overline{q} + q'. \tag{1}$$

Since turbulence is movement of air, its intensity can be characterized by the fluctuations of the wind in the three directions, u', v' (horizontal), and w' (vertical). Specifically, it is described by the turbulence kinetic energy (TKE) per unit mass m as

$$\overline{e} = \frac{TKE}{m} \equiv \frac{1}{2}\left(\overline{u'u'} + \overline{v'v'} + \overline{w'w'}\right), \tag{2}$$

where $\overline{u'u'}$, $\overline{v'v'}$ and $\overline{w'w'}$ are the means (overbar) of the square of each wind speed deviation (Moene and Van Dam, 2014). Since turbulent kinetic energy describes the intensity of turbulence, an increase in TKE means an increase in turbulence and vice versa. The budget for TKE for a horizontally homogeneous situation can be obtained from fluid dynamics (Wyngaard, 2010) as

$$\frac{\partial \overline{e}}{\partial t} = -\overline{u'w'}\frac{\partial \overline{u}}{\partial z} + \frac{g}{\overline{T}}\overline{w'T'} - ... - ... - \epsilon, \tag{3}$$

where the term on the left hand side is the change over time in TKE (positive means turbulence production). The first term is wind shear production, which is typically positive since the vertical momentum transport $\overline{u'w'}$ is typically negative. The second term describes the effect of buoyancy, which can either be positive (production) or negative (destruction). The third and fourth term are a pressure and a transport term, which are for now ignored because they mainly redistribute TKE. The last term is always a destructive term, it is the dissipation of TKE ϵ because of molecular friction (viscosity).

Besides a budget for TKE, a budget can also be obtained for another quantity involved in turbulence, the temperature variance

$$\frac{\partial \overline{T'T'}}{\partial t} = -2\overline{w'T'}\frac{\partial \overline{T}}{\partial z} + ... - 2\epsilon_\theta, \tag{4}$$

which describes the change over time in the variance budget. Similar to the TKE budget, this budget has a production term as first term, which is the heat flux H. There also is again a transport term and a destruction term, which is the dissipation of the temperature variance ϵ_θ. By neglecting the transport

and pressure terms and by assuming a stationary situation ($\frac{\partial}{\partial t} = 0$), the TKE and the temperature variance budgets then simplify to

$$\frac{g}{T}\overline{w'T'} - \overline{u'w'}\frac{\partial \overline{u}}{\partial z} = \epsilon, \tag{5}$$

$$-\overline{w'T'}\frac{\partial \overline{T}}{\partial z} = \epsilon_\theta. \tag{6}$$

The two budgets can be related to each other through the dissipation terms ϵ and ϵ_θ by the structure parameter of temperature, C_T^2, as

$$C_T^2 = 4\beta_\theta \epsilon_\theta \epsilon^{-1/3}, \tag{7}$$

where β_θ is the Obukhov-Corrsin constant (Hartogensis, 2006).

8.2. Turbulent temperature spectra

After a brief introduction into turbulence, this section now extends on this with the introduction of turbulent spectra. The spectrum of a variable describes how that variable is distributed over size (using the wave-number k) or over frequency (f). For a variable $f(x,t)$ that is a function in time and space, its distribution over k or f is obtained by taking the Fourier transform

$$\mathcal{F}(k,f) = \int_{-\infty}^{\infty}\int_{-\infty}^{\infty} f(x,t)e^{-j2\pi(kx+ft)}dxdt, \tag{8}$$

where j is the imaginary number and $\mathcal{F}(k,f)$ the transformed variable from space x and time t to wave-number k and frequency f. Taking the square of the absolute value of $\mathcal{F}$ then yields the energy spectral density S_f of the variable f

$$S_f = |\mathcal{F}|^2. \tag{9}$$

The turbulent spectrum is obtained by taking the energy spectral density of the temperature T. A conceptual representation of this spectrum is shown in Figure 28. This spectrum is taken over the wave-number k as this can relate it to the size of turbulent eddies. Eddies are swirling and rotating motions as a result of turbulence, so large eddies are large turbulent structures and vice versa. The size of eddies can be expressed as $2\pi k$.

At small wave-numbers (so large eddies) turbulence is generated by input from the heat flux H. This range is called the production range. As these eddies get mixed by turbulent mixing, they are broken up into smaller eddies while their energies are conserved and redistributed into smaller scales (so larger wave-number). This process of transferring energy from larger to smaller scales is called the energy cascade and happens in the inertial range. As the eddies get smaller, there is a length scale at which they start to be influenced by molecular effects. This happens at the inner scale of turbulence, l_0. At length scales smaller than l_0 eddies start to dissipate with a rate ϵ because of molecular friction and diffusion. For this reason, this smallest-scale range is called the dissipation range.

In the inertial range, the transferred energy scales with a -5/3 power law, the Kolomgorov power law

$$S_T = \beta_\theta \epsilon_\theta \epsilon^{-1/3} k^{-5/3} = 1/4 C_T^2 k^{-5/3}, \tag{10}$$

where the second equality comes from the definition of the structure parameter C_T^2 in Equation 7. The value of the spectrum in the inertial range therefore is proportional to C_T^2 , which will later be extensively used and elaborated on.

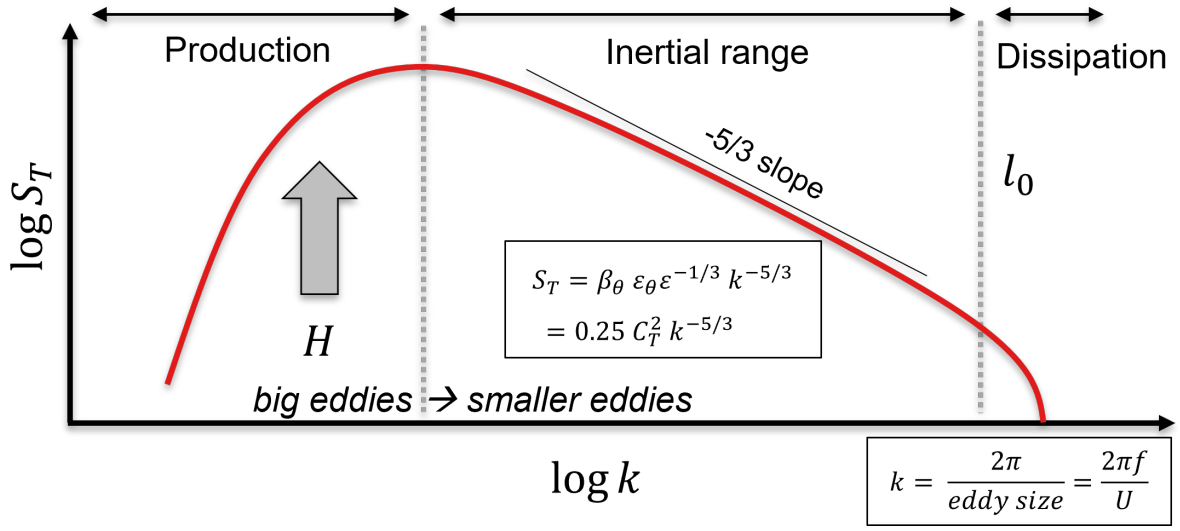

Figure 28.: Conceptual drawing of a turbulent spectrum. S_T, the spectral density of temperature and k, the wave number, are plotted logarithmically. Large turbulent eddies are produced from energy obtained by heat flux H. These eddies are then broken down into smaller eddies in the inertial range. This inertial breakdown happens by turbulent mixing, with a rate ϵ. Eddies small enough to be influenced by molecular effects are then destroyed by viscosity, which dissipates their energy. This dissipation happens from a scale smaller than l_0, the inner range of turbulence.

8.3. Structure parameter of temperature

The structure parameter can be obtained directly through its definition or with the use of the -5/3 slope in the inertial range of the turbulent spectrum. The structure parameter C_T^2 is a 'scaling parameter of the temperature spectrum in the inertial range of turbulence' (Hartogensis, 2006; Stull, 1988), which is defined as

$$C_T^2 \equiv \frac{\overline{[T(x) - T(x+r)]^2}}{r^{2/3}}, \tag{11}$$

where $T(x)$ is the temperature at location x and $T(x+r)$ is the temperature at a point separated from x by a distance r. This separation distance r should be chosen so that it lies within the turbulent length scales of the inertial range. Conceptually then, C_T^2 is a spatial turbulent statistic that describes the occurrence of temperature fluctuations at a certain scale r. By applying Taylor's hypothesis (Equation 11) can be calculated for a time series. This hypothesis states that turbulent eddies are frozen as they are advected past a sensor. In other words, that the distance r can be replaced by $U\Delta t$, with U the mean horizontal wind speed and Δt the time difference between two measurements. C_T^2 can then be measured by a point sensor as a time series

$$C_T^2 = \frac{\overline{[T(t) - T(t+\Delta t)]^2}}{(U\Delta t)^{2/3}}. \tag{12}$$

Alternatively, combining the expression for height of the turbulent spectra S_T in the inertial range (Equation 10) with the mean horizontal wind speed U can also yield a value for C_T^2. Substitution of the wave-number k for a frequency f using $k = 2\pi f/U$ then gives the expression

$$C_T^2 = 4\left(\frac{2\pi}{U}\right)^{2/3} f^{-5/3} S_T(f). \tag{13}$$

9. Methods

9.1. DTS set-up

The experiment described in this part concerns one large set-up that extends horizontally, as opposed to the three vertically extending set-ups from Part 1. The method for this set-up in terms of hardware is far a large part similar to the general method as outlined in Part 1 (Section 4.1.1). The same outdoor calibration baths as for the vertical set-ups are used (Figure 6) and fiber follows the same path going from the cabin to the outdoor calibration baths. As reference sensors, the same temperature data from the Pt-100 sensors and TidBit dataloggers described in Part 1 are used.

The set-up is however an indepently installed DTS experiment. It is not connected to the DTS experiment from Part 1, except that it takes place on the same location and that the same reference data is used. A schematic representation of the fiber path in this experiment is shown in Figure 29. A different DTS computer is used for this experiment, the SiliXa Ultima S. This DTS has a temporal resolution of 1 s and a spatial resolution of 12.7 cm, which is higher compared to the Ultima M from Part 1 (5 s and 25.4 cm). These resolutions therefore make the Ultima S a better option for looking into turbulent fluctuations.

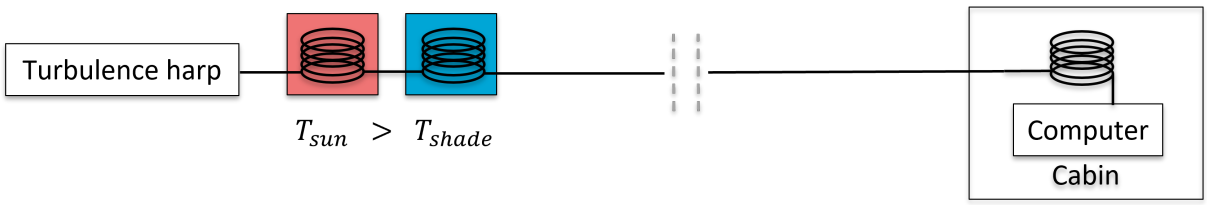

Figure 29.: Overview of the complete fiber path along the horizontal set-up. The fiber path begins in an air-conditioned cabin, starting at the DTS computer. The fiber path then goes towards the outdoor calibration baths, where it is spliced to a thinner cable before entering both calibration baths. The calibration baths are the same bath used in Part 1 with T_{sun} and T_{shade}.

A thinner 0.5 mm fiber with only an acryllic cladding is used for this experiment as this has a faster response time ($\approx$ 1 s) than the 1.6 mm Kevlar-reinforced fiber used in Part 1 ($\approx$ 10 s). This faster response time comes with the downside of the fiber being significantly more fragile. Therefore a 1.6 mm cable is used to cover the distance from the cabin to the outdoor calibration baths, which is spliced to the thin cable just before entering the calibration baths. A length of approximately 25 m of fiber is coiled loosely in both calibration baths to serve as reference sections, after which the fiber path goes towards the set-up (see Figure 29).

The set-up for this experiments consists of a turbulence harp, and is essentially a large-scale version of the canopy harp described in Part 1. The harp is designed to span a horizontal distance of 75 m, which is the same path length as the scintillometer installed by Wageningen University and Research. It is also placed into the same northeast-to-southwest orientatation of the scintillometer, at a distance of approximately 30 m as to not disturb the scintillometer measurements. This orientation, displayed in Figure 4, was chosen so that the turbulence harp catches the same footprint as the scintillometer for the predominant SW / NE wind direction.

Figure 30 shows a schematic depiction of the turbulence harp (Figure 30a) as well as two views of the turbulence harp installed in the field (Figures 30b and 30c). The set-up measures at heights of $z = 2.05$ m, $z = 1.40$ m, $z = 0.80$ m and $z = 0.40$ m and spans a horizontal path of $x = 70$ m. Iron poles with 2.5 cm diameter were hammered into the ground at 5 m intervals to provide attachment points for the fiber. The top height of $z = 2.05$ m is chosen as this is the same height as the scintillometer path.

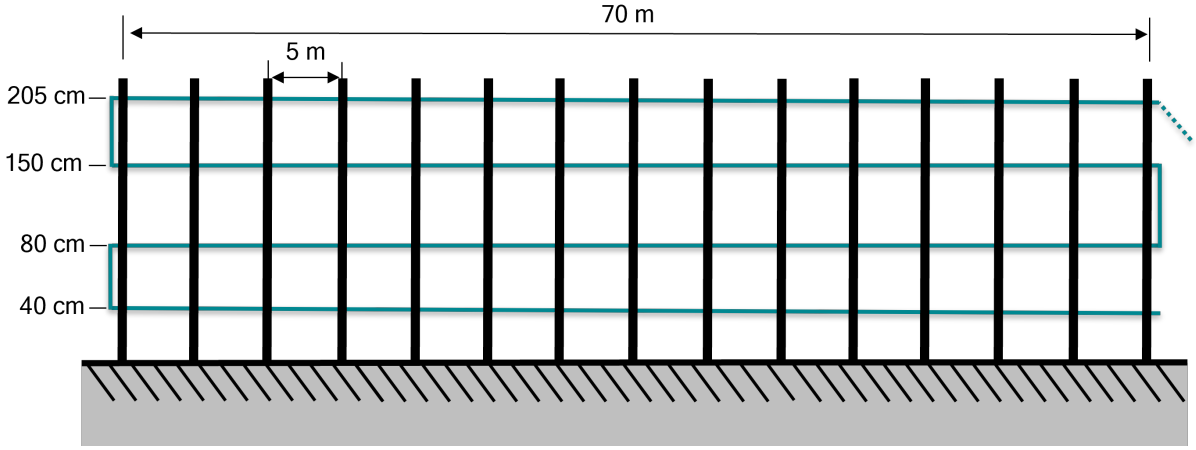

(a) Schematic view

(b) View along path

(c) View at pole

Figure 30.: Overview of the turbulence harp set-up, a large fence-like structure that spans 70 m and measures at heights of $z = 2.05$ m, $z = 1.40$ m, $z = 0.80$ m and $z = 0.40$ m. Metal poles are placed every 5 m to support the fiber.

The fiber is attached to the poles using pieces of foam that are clamped to the cable. A collection of examples concerning the securing and guiding of the fiber can be found in Figure 57 in the Appendix. Because the fragile thin fiber is susceptible to wind in this set-up, it is clamped at every connecting point using cable ties (Figure 57a), and at several connection points also with hose clamps (Figure 57d). This way the fiber can be pulled tight on the horizontal paths and then secured so it does not get moved and fluttered in the wind. Clamping the fiber horizontally also allows for less tension to be put on the fiber at the connection points at both ends of the harp. This prevents sharp corners in the fiber path where it connects the path at different heights (Figure 57e).

Conversion of the measurements from LAF coordinates to physical x and z coordinates is done using the same ice pack localization method as described in Part 1. Here it should be noted that the direction

of LAF reversed for different heights because of the fiber path going back and forth (see Figure 30a). The fiber path at lower height has the largest chance of breaking because of vegetation and rodents. Therefore the fiber path first travels along the top height ($z = 2.05$ m) before travelling downwards to low z. This way, when a break happens at low z, measurements will still continue for the rest of the set-up. An overview of the physical locations corresponding to the fiber path in LAF is given in Table 2 in the Appendix.

9.2. Research approach

9.2.1. Data processing

To convert the raw measurements into data suitable for analysis of structure parameters, several processing steps are needed. These steps are first listed in this section, after which several considerations and details in this approach are presented.

1. **Calibration** using the DTSCALIBRATION package (des Tombe et al., 2020).
2. **Mapping** the fiber path from LAF coordinates into physical coordinates x and z. Both calibration and mapping can be done simultaneously with the PYFOCS package (Lapo and Freundorfer, 2020). This results into NetCDF files for each 30 minute interval. The steps after this are executed on each NetCDF file separately.
3. **Convert to linearly-spaced time.** Each 1 second measurement conducted by the Ultima S requires a processing time which can differ for each measurement and will lower the effective temporal resolution. The measurement frequency is calculated as by dividing the number of measurements over 30 minutes, e.g. $f_s = \#\text{measurements}/1800\text{s}$.
4. **Conversion to UTC.** Universal Time = Local Time - 2 hours
5. **Masking out of poles.** Since the metal poles are large thermal masses, they will act as hot or cold spots and should therefore be filtered out. This filtering is done by masking out points along the line that have a temperature variance σ_T^2 over a day above a certain threshold.
6. **Linear detrending** per 30 minutes of measurement to remove longer term trends.

Similar to Part 1, calibration using the reference data and the proposed calibration strategy (steps 1 and 2 from Section 9.2.1) was not working properly. Therefore in this part it was also chosen to work with the raw data within the scope of this MSc thesis. Since the main interest of this part is looking into temperature fluctuations, absolute temperatures should not be strictly necessary. Rigid calibration is then left for further investigation into this data set. Instead a routine was developed to process the raw data into clean NetCDF files that can be used for analysis. This routine converts the raw data with LAF coordinates into 30 minute NetCDF files that contain a variable with temperature data for each four heights as a function of time t and distance x. Here $x = 0$ m is taken as the *north-westernmost* part of the turbulence harp (point 6 in Figure 4) and $x = 70$ m is the *south-easternmost* part. This means that x increases when looking towards the central measurement site.

Converting to linearly-spaced time (processing point 3) results in an effective measurement frequency of $f_s = (0.85 \pm 0.05)$ Hz. This value for f_s was obtained by taking the mean and standard deviation of the found measurement frequencies during July 16, as shown in Figure 31. This means that the average processing time per 1 s measurement is (0.18 ± 0.01) s.

The results from creating the pole mask are displayed in Figure 32. Here the resulting pole mask is plotted in grey along with the temperature variances found over the complete day of July 16. The mask is determined by detecting the maximum value of σ_T^2 at each pole location. To fully remove the effect of

the poles, four points on either end of this maximum value were then also masked out. This results in a mask size for each pole of 9 data points, or 1.14 m, which means 22% of the data along the transect is considered influenced by the poles.

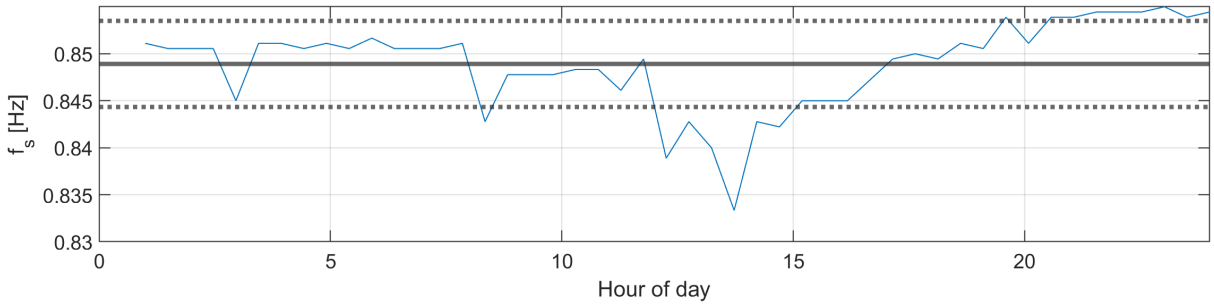

Figure 31.: Sampling frequencies f_s during July 16. Also plotted are the mean f_s during this day in a solid line and the standard deviation of the mean in dashed lines.

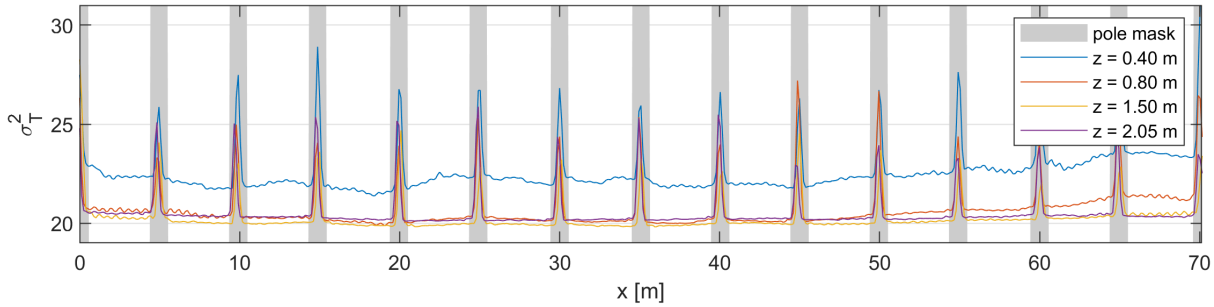

Figure 32.: Temperature variance along July 16 for pole masking. Temperature variance σ_T^2 is calculated for the full day and plotted for all heights. A pole mask is based on the extreme values of σ_T^2.

9.2.2. Structure parameter algorithms

Figure 33 outlines the workflow for determining the structure parameters C_T^2 with the processed data. Since the turbulence harp dataset $T(x,t)$ contains temperature data both over space and time, C_T^2 can be determined along both those dimensions. The first part of the analysis treats the data as a time series, where a point along the transect (line) is taken as a time series, resulting in the structure parameter over time $C_T^2(t)$. The second part of the analysis takes a series of temperature measurements along the transect at a certain point of time. This results in structure parameters over space $C_T^2(x)$. Within the two analysis parts, structure parameters are calculated both using the definition of C_T^2 and using the spectrum and the -5/3 power law for the inertial range. Four different structure parameters are thus obtained from the dataset; $C_{T,def}^2(t)$, $C_{T,spec}^2(t)$, $C_{T,def}^2(x)$ and $C_{T,spec}^2(x)$.

To obtain the structure parameters using the -5/3 power law, first the spectrum has to be calculated. This is done using the fast Fourier transform (FFT). The FFT is a routine to compute the discrete version of the Fourier transform (Equation 8)

$$\mathcal{T}[f] = \sum_{t=1}^{t_m} T[t] e^{-j2\pi(f-1)\frac{t-1}{t_m}}, \tag{1}$$

where $\mathcal{T}[f]$ is the discrete Fourier transform and t_m is the total measurement time. The `spec_FFT_OH.m` function (Hartogensis, 2006) is used to calculate the FFT and then its power spectrum. From this spectrum, C_T^2 is then calculated using `Cxy_Spectra_OH.m`. This function calculates C_T^2 for all points in the spectrum using the -5/3 power law (Equation 10) and then determines an average value for all found values that lie within a certain specification within the -5/3 slope.

The spatial series of the dataset is not a continuous series because the poles are masked out along it, therefore the FFT cannot be applied to it directly. Instead, a non-uniform discrete Fourier transform has to be applied to the spatial series

$$\mathcal{T}[k] = \sum_{x=1}^{X_m} T[x] e^{-j2\pi(k-1)\frac{P[x]}{X_m}}, \tag{2}$$

where $\mathcal{T}[k]$ is again the discrete Fourier transform and X_m is the total measurement period. Here a function $P[x]$ is introduced which defines the non-uniform spacing of the series. To obtain C_T^2 from the spectral methods, detection of the -5/3 slope is necessary. Therefore, only when an inertial range is present within the measurement periods, a structure parameter will be found. Using the definition of the structure parameter will produce a result regardless of the presence of an inertial range. This means the definition method will always work for determining C_T^2 , while the spectral method only works when there is an inertial range present.

As a reference dataset, temperature time series measurements from a sonic anemometer are used, located near the south-easternmost point of the turbulence harp. From this time series C_T^2 is also obtained from the definition method and the spectral method, resulting in $C_{Ts,def}^2$ and $C_{Ts,spec}^2$. Using the sonic anemometer data allows for comparison of the DTS structure parameters to a conventional instrument.

Because Taylor's frozen turbulence hypothesis is used in the determination of C_T^2 from time series, horizontal wind speed U is also needed in both time series methods. Time series from the sonic anemometer that is also used as the reference instrument are used to this end.

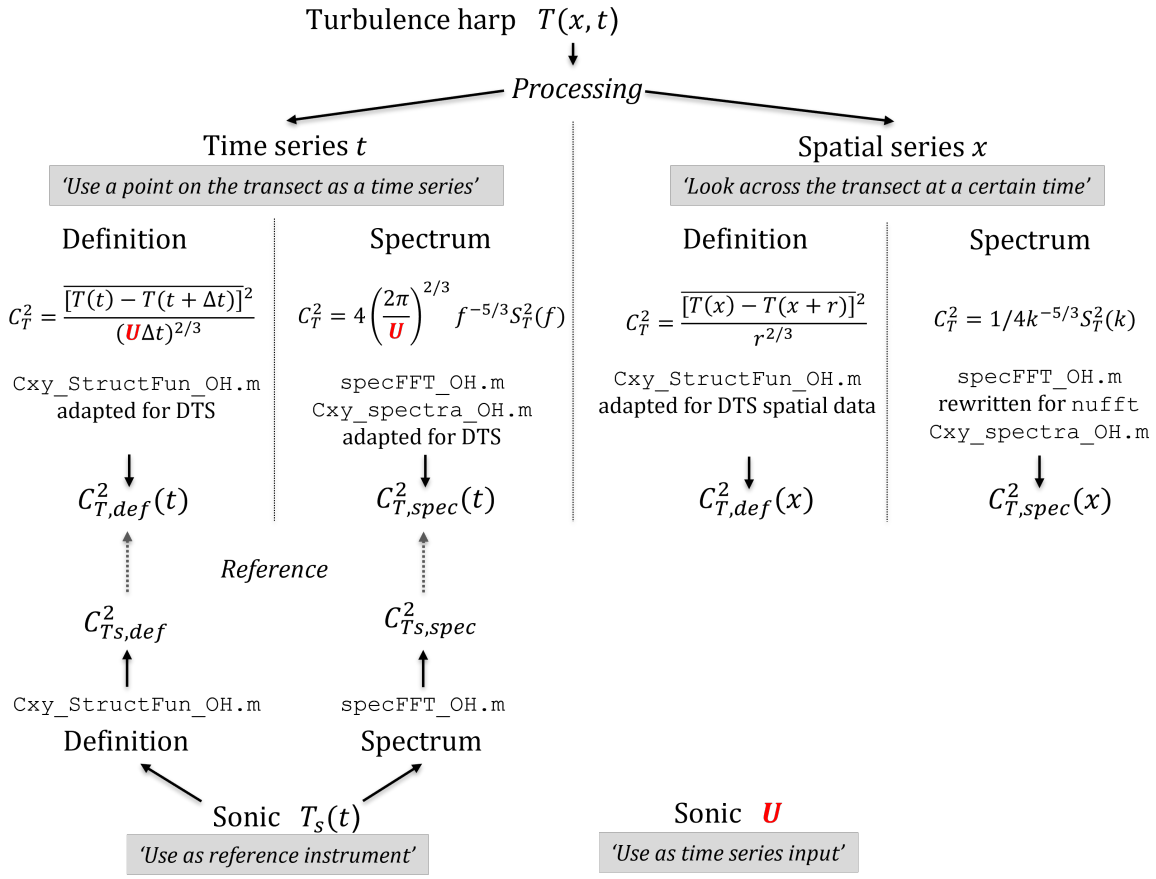

Figure 33.: Workflow in determining C_T^2 . The turbulence harp data is both used as time series and as spatial series. For each series, C_T^2 is determined through its definition and through its spectrum using the -5/3 power law. Sonic anemometer time series data is used as a reference dataset and as input for the horizontal wind speed.

9.3. Reference data

Before looking into the turbulence harp dataset, this section will first briefly present the reference values as obtained by the sonic anemometer. Using a temperature time series of 30 minutes (16 July 10:00-10:30 UTC) the turbulent spectrum for the sonic anemometer was computed, which is shown in Figure 34. Added to this figure is a -5/3 slope at an arbitrary height. Using this -5/3 slope as a reference, the inertial range appears to exist between 0.2 Hz and 8 Hz. Above 8 Hz the spectrum flattens, which is also where is approaches the limit of the sampling rate of the sonic of 20 Hz (e.g. the Nyquist limit of 10 Hz).

Included in Figure 34 are three values for the separation distance r as a reference to what place r corresponds to within the inertial range. Here r is calculated by combining $k = 2\pi f/U$ and $k = 2\pi/r$ so that $f = U/r$. Here $r = 5$ m and $r = 1$ m are chosen arbitrarily as typical scales. The value of $r = 8.31$ m is the separation distance that results in a $C_{Ts,def}^2$ that matches closest to $C_{Ts,spec}^2$. This result for r was obtained by minimizing the sum of squared differences between $C_{Ts,def}^2$ and $C_{Ts,spec}^2$.

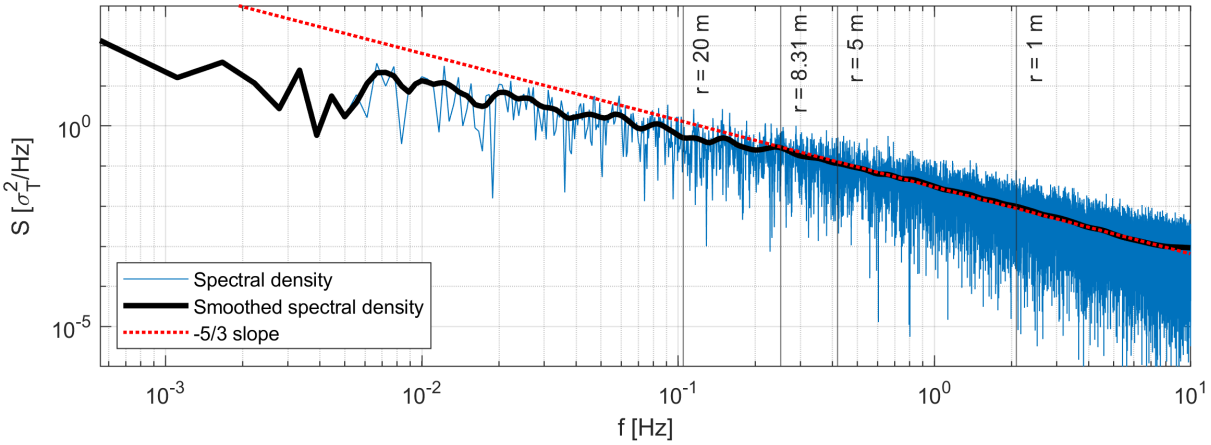

Figure 34.: Turbulent spectrum of the sonic anemometer, for 16 July 10:00-10:30 UTC. Both the raw and a smoothed spectrum are shown, as well as the -5/3 slope at an arbitrary height. Three values for the separation distance r are also included.

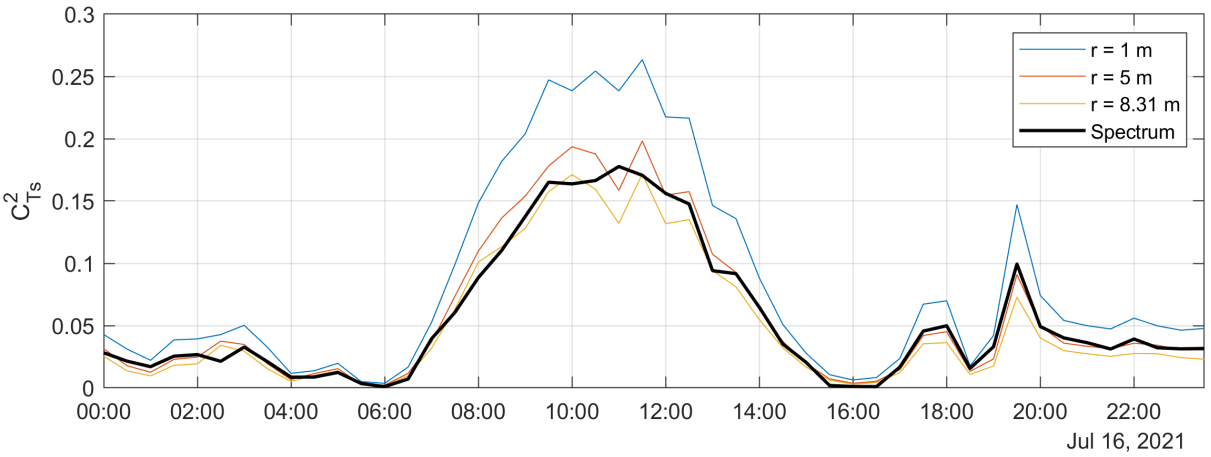

Figure 35.: Structure parameters from the sonic anemometer. Results from the spectral method $C^2_{Ts,spec}$ are shown in a solid black line. Results from the definition method are shown for three values of r.

10. Results

10.1. Raw data

The periods in which measurements were done and remarks around that are discussed in Part 1 in Section 4.2.1 and summarized in Figure 12. Mainly, the turbulence harp has been measuring continuously for a 7-day period with available reference data from 15 to 22 July. A figure of a single measurement along the whole dataset (including the connecting fiber paths and the calibration baths) for 16 July 12 UTC can be found in the Appendix in Figure 56.

It was chosen to limit most of this analysis to a single day for brevity and to make computation more manageable. July 16 was chosen, the second day of the campaign. Since this was in the beginning of the campaign there was still little vegetation, so there was a high Bowen ratio. Combined with the high temperatures of this day, it was considered the day with most potential for a large amount of temperature fluctuations. Most of the figures displayed in this chapter concern the transect at $z = 0.40$ m, since the largest amount of fluctuations are expected there.

Figure 36 shows unprocessed data for all of 16 July as a contour plot for $z = 0.40$ m. The diurnal trend is visible, as well as a clear bias in temperature introduced by the poles. The processed data is obtained following the processing steps for detrending and masking out the poles as outlined in Section 9.2.1, which is shown in Figure 37. Here it is already visible that temperature fluctuation are largest around noon. Figure 38 shows a 5 minute zoom-in version of turbulence harp data for all heights at 12 UTC. It should be noted here that the limit of the colour scale changes for different heights, but that the total range remains fixed at 5 °C. This is done to show enough contrast, without removing the vertical temperature gradient. The two-dimensional temperature data shown in this figure show a great benefit of using DTS to measure turbulent fluctuations, as turbulent structures can be seen across the transect. Also visible is that the structures seen occur on smaller scales for low z and become larger with increasing z (and smooth out in the figure). Physically this makes sense, considering that for low z the effect of surface heating is strongest and that at high z there is space for larger eddies.

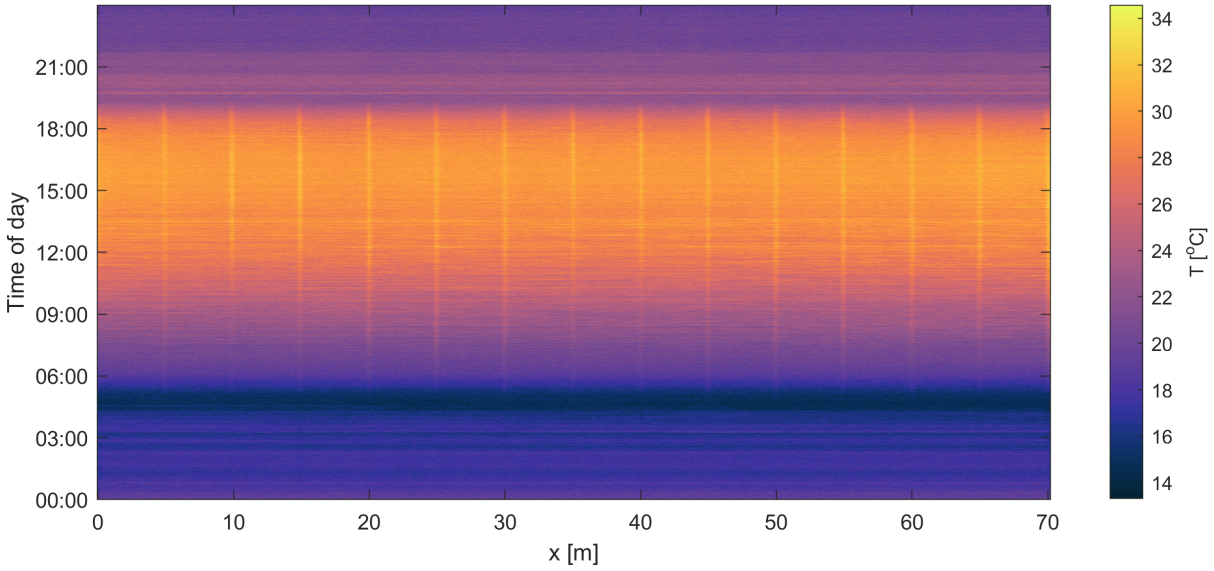

Figure 36.: Unprocessed dataset of the turbulence harp for 16 July and $z = 0.40$ m. Both the diurnal cycle and the temperature bias created by the poles are visible in the contour.

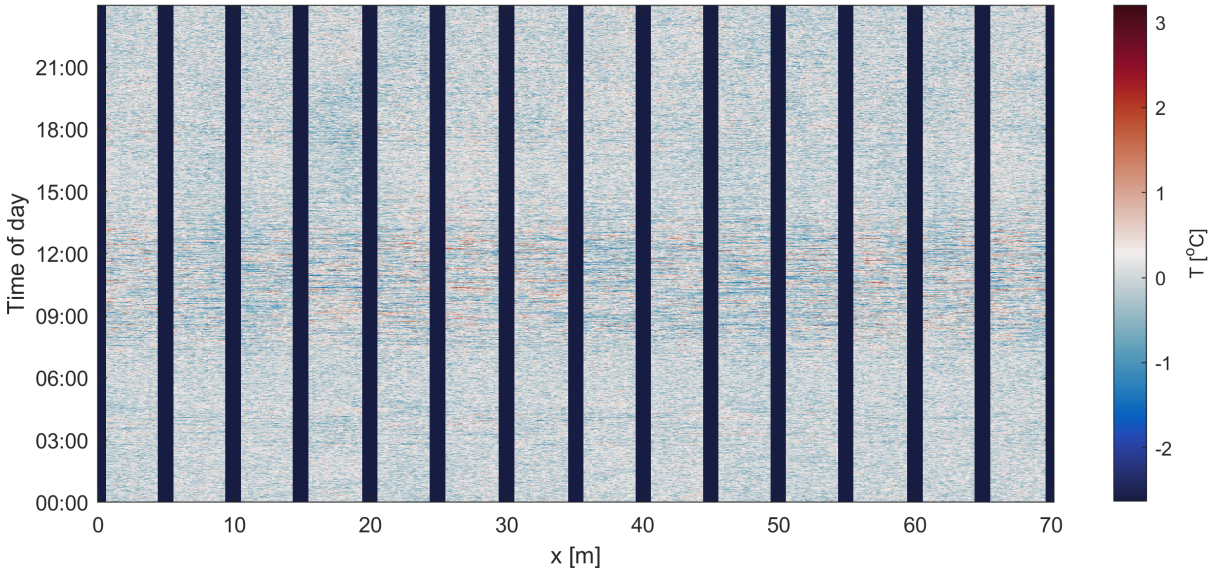

Figure 37.: Processed dataset of the turbulence harp for 16 July and $z = 0.40$ m. Poles are masked out and the data is detrended.

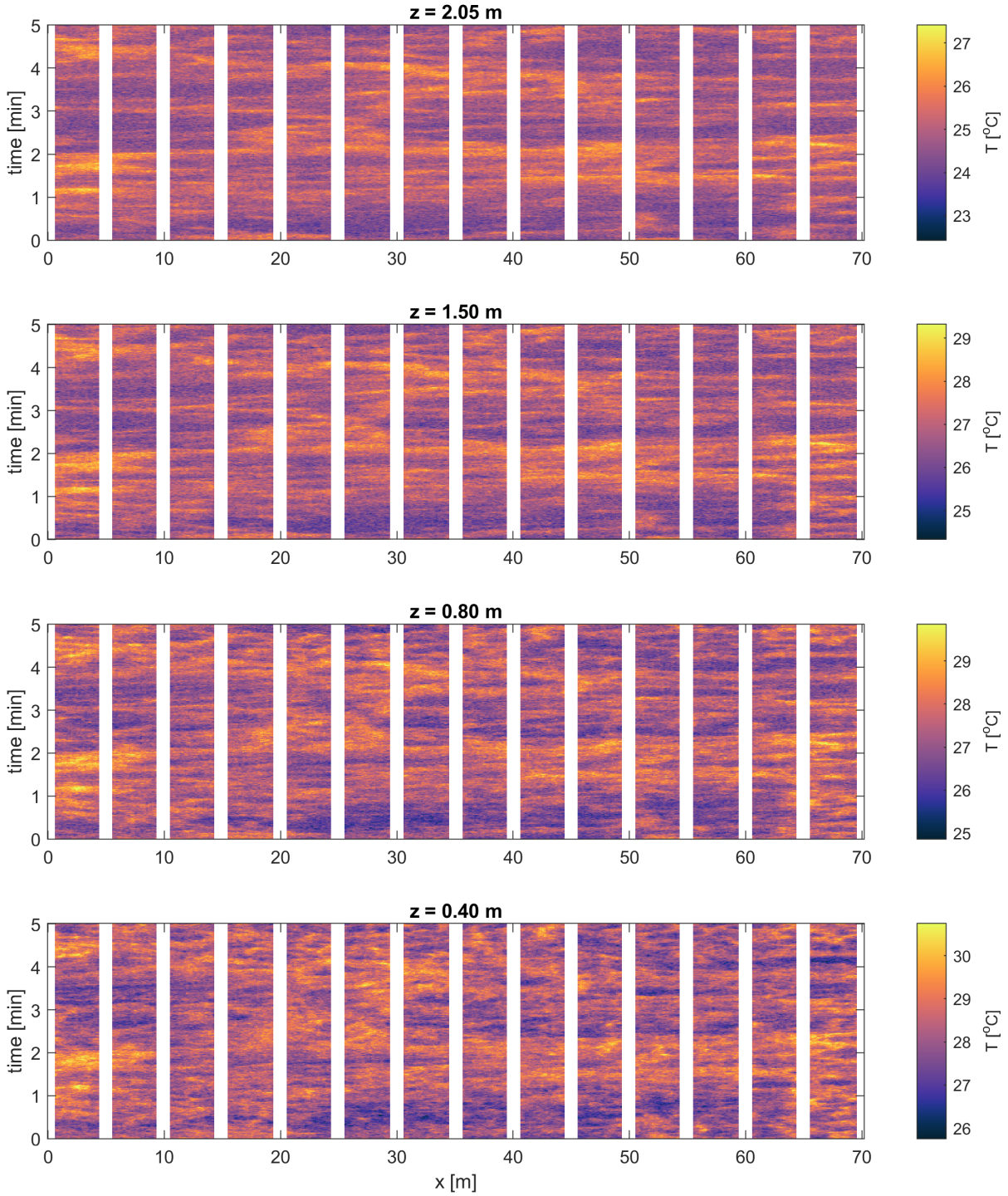

Figure 38.: 5-minute zoom-in of turbulence harp data for heights $z = 2.05$ m, $z = 1.50$ m, $z = 0.80$ m and $z = 0.40$ m. Note that the limits of the colorbar change, but that its range remains fixed at 5 °C to allow for enough contrast.

10.2. C_T^2 time series

10.2.1. Definition method

Using the definition of the structure parameter (Equation 12), $C_{T,def}^2(t)$ was calculated for all four heights of the turbulence harp using $r = 8.31$ m. Every 30 minute interval, for each point x along the transect the structure parameter was computed and then averaged across the transect. This resulted in $C_{T,def}^2(t)$ values every 30 minutes for each height, which are displayed in Figure 39. Also plotted here are the found structure parameters from the sonic anemometer obtained through the definition method (for $r = 8.31$ m) and the spectral method, as a reference.

In Figure 39 it is visible that there is a strong diurnal trend in C_T^2 for the sonic anemometer, as well as an enhancement of C_T^2 around 20:00. The structure parameters obtained from the turbulence harp seem to follow that same diurnal trend, but significantly more dampened. During the night, the DTS structure parameters are approximately double to those obtained from the sonic anemometer. This could be due to the instrument noise of the DTS creating artificial temperature fluctuations. Theoretically C_T^2 should be low (close to zero) in stable nighttime conditions because there will be stratification and temperature fluctuations will be small. Instrument noise could introduce more variance within the signal, therefore increasing the detected C_T^2 .

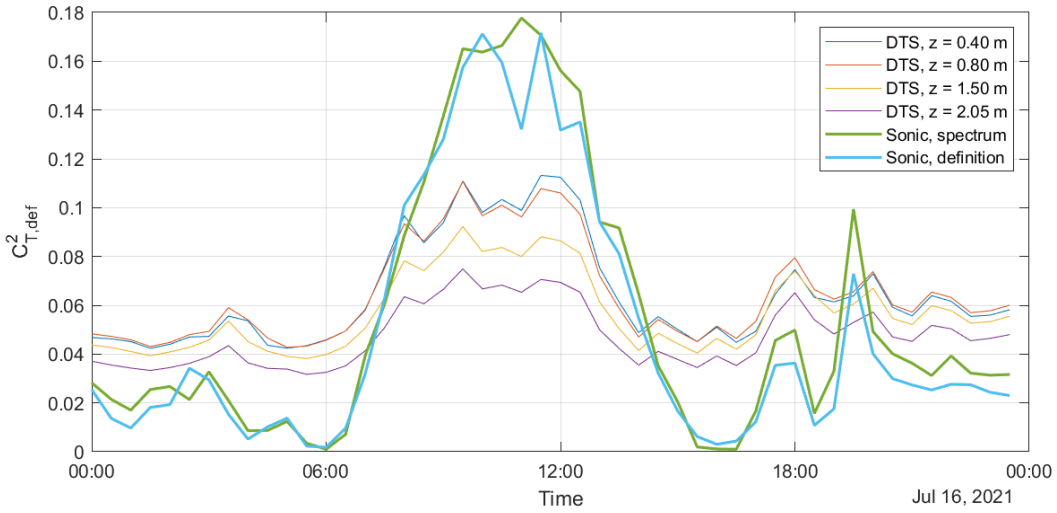

Figure 39.: Structure parameter over time obtained through its definition ($C_{T,def}^2(t)$) for all heights of the turbulence harp. Also plotted are the structure parameters obtained from the sonic anemometer through both the definition and the spectral method.

On the other end of the diurnal trend, the large C_T^2 values seen in the sonic anemometer data are not recreated by the DTS. This could be due to the DTS not measuring fast enough to sample a representative inertial range. Theoretically the DTS measures at 1 Hz, but the response time of the fiber, processing time and radiative effects could result in this being significantly slower. This effective sample rate will be investigated more closely using spectra in Section 10.2.2.

Both of the limitations of the DTS measurements mentioned above can be investigated with further investigation, if these causes are assumed to be independent of each other. To validate the nighttime noise hypothesis, the sonic anemometer dataset can be modified to contain more instrumentation noise. This can be achieved by adding a constant white noise signal to the dataset, therefore increasing the noise floor. If this results in an enhancement of C_T^2 at nighttime it can be a confirmation of the DTS introducing artificial C_T^2 values at night. To validate whether the DTS sampling rate is not fast enough to capture the inertial range properly, the sonic anemometer can also be altered to simulate a slower sampling rate. This can be done by either running a moving average over the time series or by applying a low-pass filter with a cut-off frequency of 1 Hz (the DTS sampling rate).

In an attempt to quantify the underestimation in the diurnal trend of C_T^2 by the DTS, the correlation between the sonic anemometer and DTS $C_{T,def}^2(t)$ is plotted and fitted in Figure 40. Here both suggested limitations can be seen in the offset and the slope of the fits. The offset present supports the nighttime noise hypothesis and the slope suggests that the DTS misses bandwidth to capture enough of the inertial range. Noticeable is that the slope increase significantly (by a factor of 2) going from the top height of the turbulence harp to the lowest height. This is likely due to smaller scale fluctuations being much more prevalent at low z, as was also visible in Figure 38.

The analysis from this section was also performed for 10 minute interval, instead of 30 minutes. The results of this analysis can be seen in the Appendix in Chapter D.

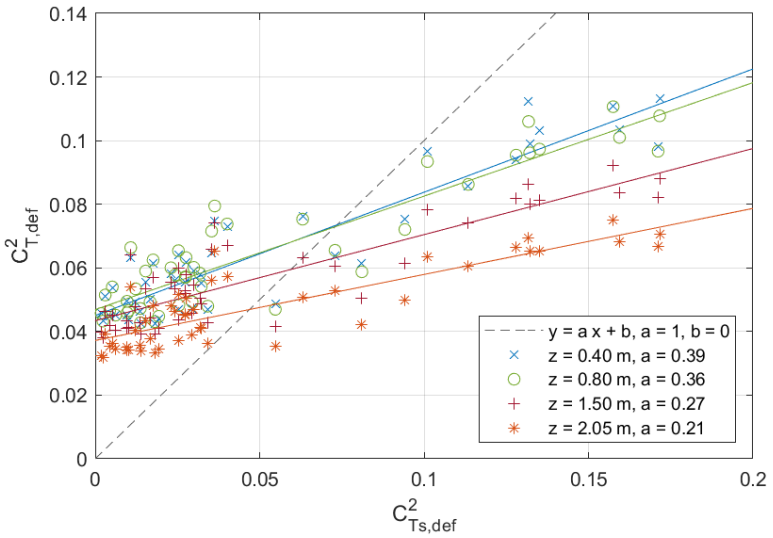

Figure 40.: Correlation between DTS and sonic anemometer for C_T^2 obtained through the definition method. The dashed line represents a 1-to-1 relation. The four heights of the turbulence harp are plotted with different colours.

The analysis in this section discussed structure parameters for each 30 minute interval using the definition method. This $C_{T,def}^2(t)$ was found by averaging C_T^2 for each point on the transect. To investigate the variation within this averaging, in this section the structure parameters for each point on the transect are plotted. Specifically, at all points C_T^2 on the transect is normalized by $C_{T,def}^2(t)$ (the mean C_T^2 of the transect) in order to find a deviation from the mean along the transect. These deviations can be found for all four heights in Figure 41. Noticeable in this figure are structural deviations across the day that can go up to 20% of the mean $C_{T,def}^2(t)$. Two distinct bands of deviation can be found at 4 UTC and 18 UTC and from $x = 0$ m to $x = 10$ m C_T^2 seems to be underestimated.

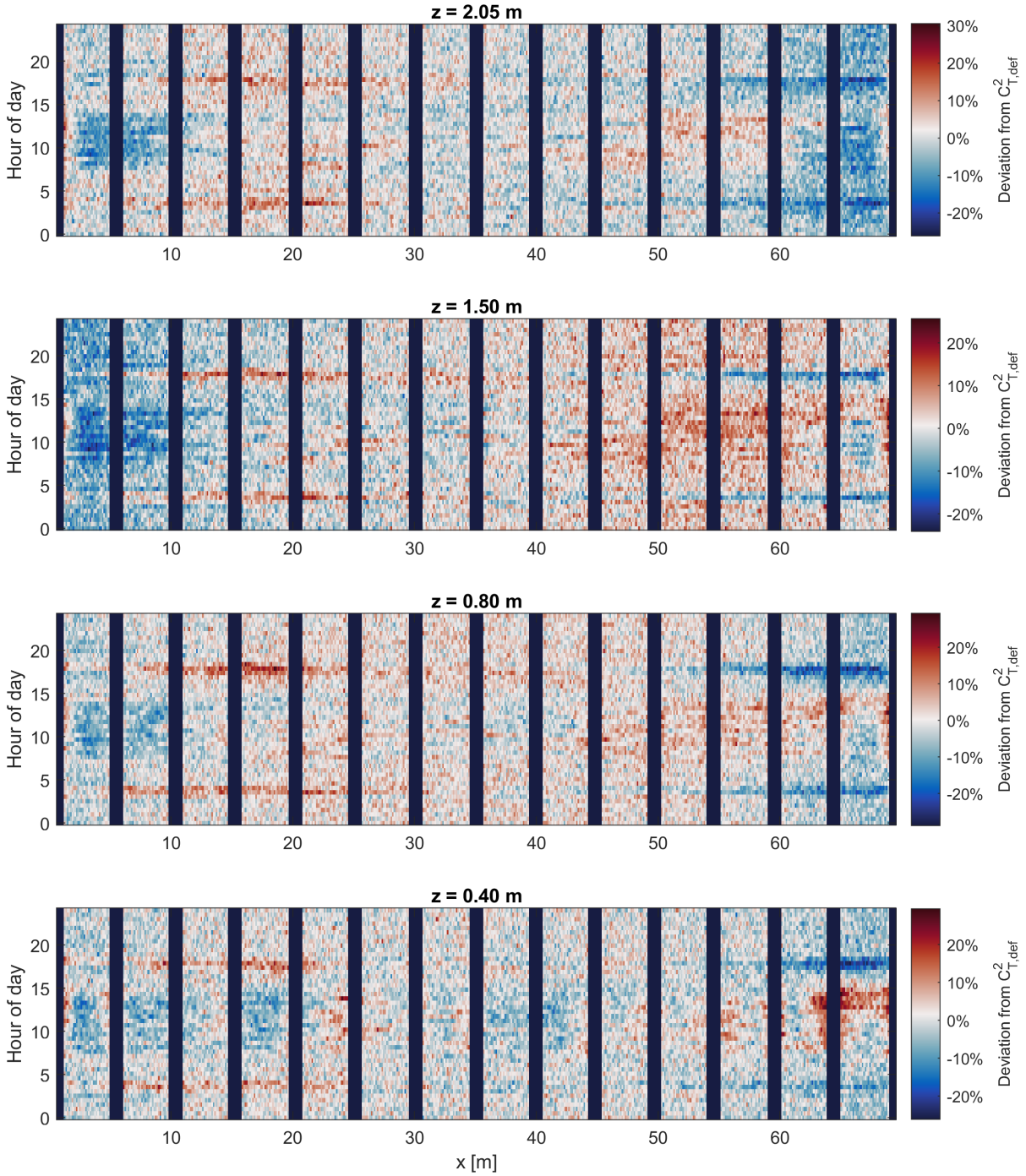

Figure 41.: Deviation of C_T^2 for each point on the fiber compared to $C_{T,def}^2(t)$ for all heights of the turbulence harp.

10.2.2. Spectral method

This section describes the results of using the spectral method to find the structure parameter in time, $C^2_{T,spec}(t)$. A spectrum of the turbulence harp is shown for $z = 0.40$ m on the right-hand side of Figure 42. This spectrum is obtained by computing the FFT of each point on the transect (shown in grey in the figure) and by taking a smoothed average of all points on the transect (shown as the thick black line). A reference -5/3 slope line is also plotted in red.

Using the -5/3 slope reference line it can be seen that a part of the DTS spectrum seems to have a corresponding -5/3, which would indicate the presence of an inertial range. This is the case between approximately $4 \cdot 10^{-2}$ Hz and $1 \cdot 10^{-1}$ Hz. On the left-hand side of Figure 42 the sonic anemometer spectrum is plotted for the same time period and with the same axis. The apparent inertial range present in the sonic anemometer is much broader than that of the DTS, both for higher and lower f.

For high frequencies, the DTS spectrum flattens off after 0.1 Hz, while the sonic anemometer spectrum continues with approximately -5/3 slope. This is a strong indication that the turbulence harp data set is limited either by noise or by a slow response time at high frequencies. When assuming that this flattening happens because of this, the effective sample rate seems to be around 0.1 Hz, rather than the 1 Hz sample rate that was specified. This limitation in bandwidth can be linked back to the results from the previous section for C^2_T obtained through the definition method, which also hinted at a this.

Spectra for the four heights of the turbulence harp are displayed in Figure 43 for the same time period as Figure 42.

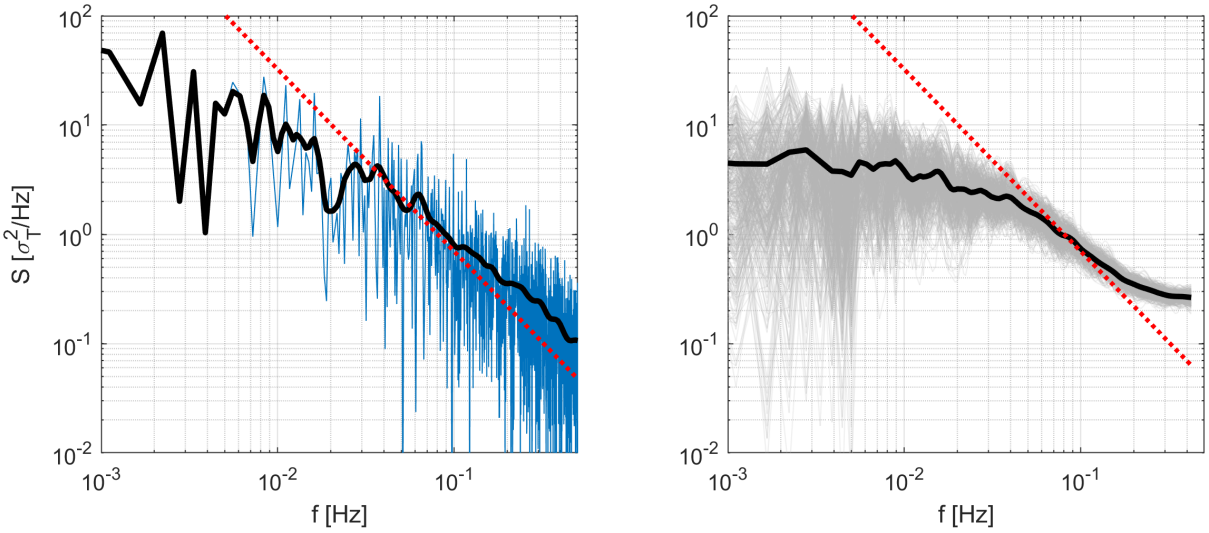

Figure 42.: Comparison of spectra. Sonic anemometer spectrum (left) compared to the DTS spectrum (right) for $z = 0.40$ m at 10:30 UTC. The dashed red line displays the -5/3 slope at the same height for both spextra.

The acquired DTS spectra were used to find structure parameters over time using the spectral method described in previous chapter. The results of this method are displayed in Figure 44 for the four heights of the turbulence harp along with the sonic anemometer results for reference. A noticeable difference between this method and the definition method is that in this method C^2_T was not always found. The definition method will always produce a result, while the spectral method needs the presence of an inertial range -5/3 slope to find a structure parameter value.

This lack of detection is especially present at nighttime, which makes sense considering that there are a smaller amount of temperature fluctuations without presence of Solar radiation. However, also during daytime C^2_T is often not detected. This is due to the inertial range being rather small in the DTS spectra (Figure 43), causing the -5/3 slope to not always be present enough to detect it for calculations of C^2_T .

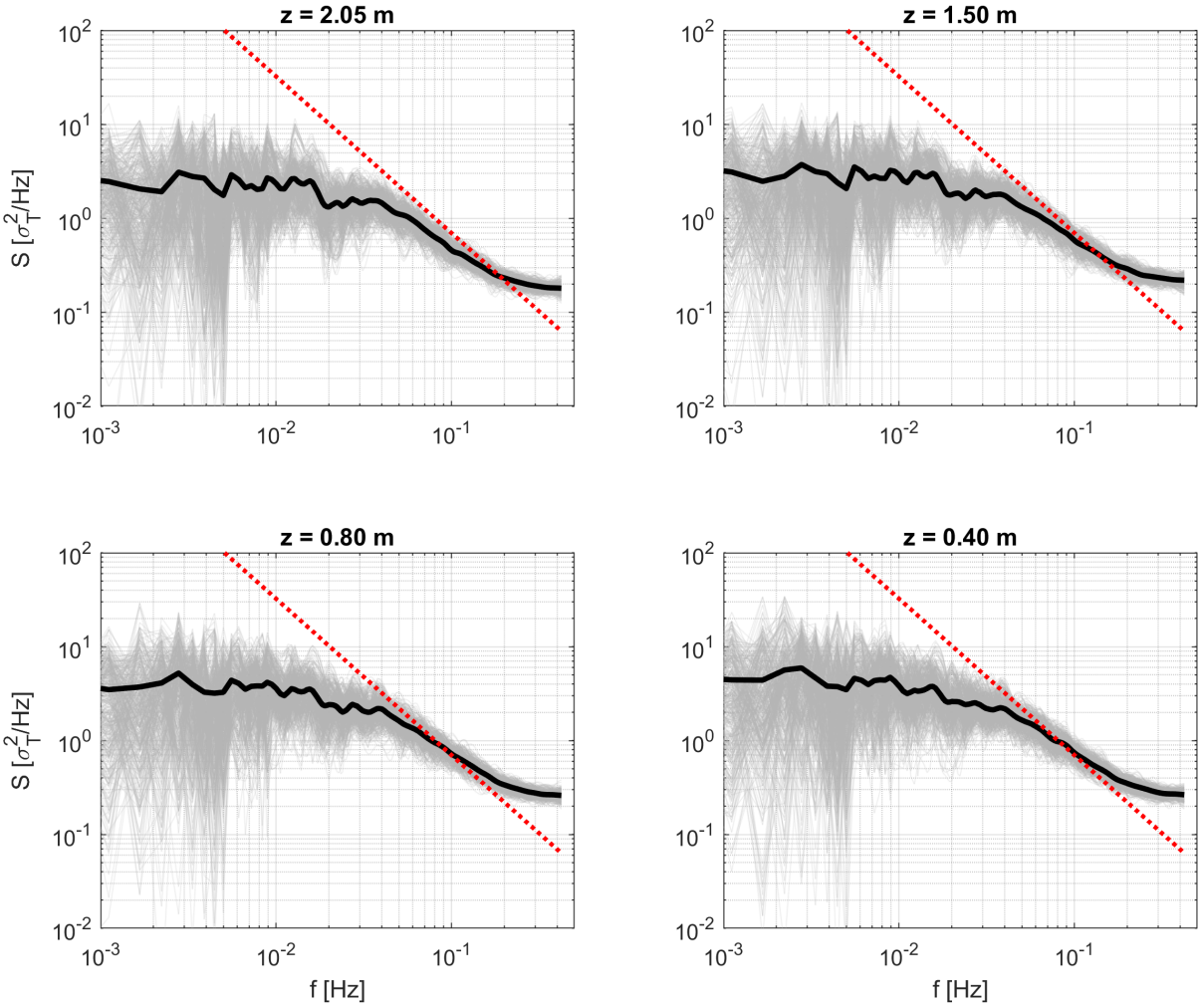

Figure 43.: Spectra of the turbulence harp for all four heights. The spectra are plotted for the same time period of 30 minutes from 16 July 10:30 UTC. The spectrum at $z = 0.40$ m is the same as shown in Figure 42.

The structure parameters that are detected do roughly follow the diurnal trend that the sonic anemometer displays. The results from $z = 0.40$ m, the lowest transect of the turbulence harp, matches best with the sonic anemometer. This can also be seen in the correlation between $C^2_{T,spec}(t)$ and $C^2_{Ts,spec}(t)$ in Figure 45. Here the slope in the correlation is steepest for $z = 0.40$ m, similar to what was found in the definition method. The slope is significantly steeper than for the definition method and the offset is smaller. This suggests that this method, which discriminates in what temperature data is acceptable for C_T^2 determination, produces a closer match to the sonic anemometer reference, although with a strong loss in the number of data points.

In an attempt to produce more detected structure parameters to use as data points, a 10 minute interval analysis was also conducted. However, this resulted in nearly no detection of structure parameters at all.

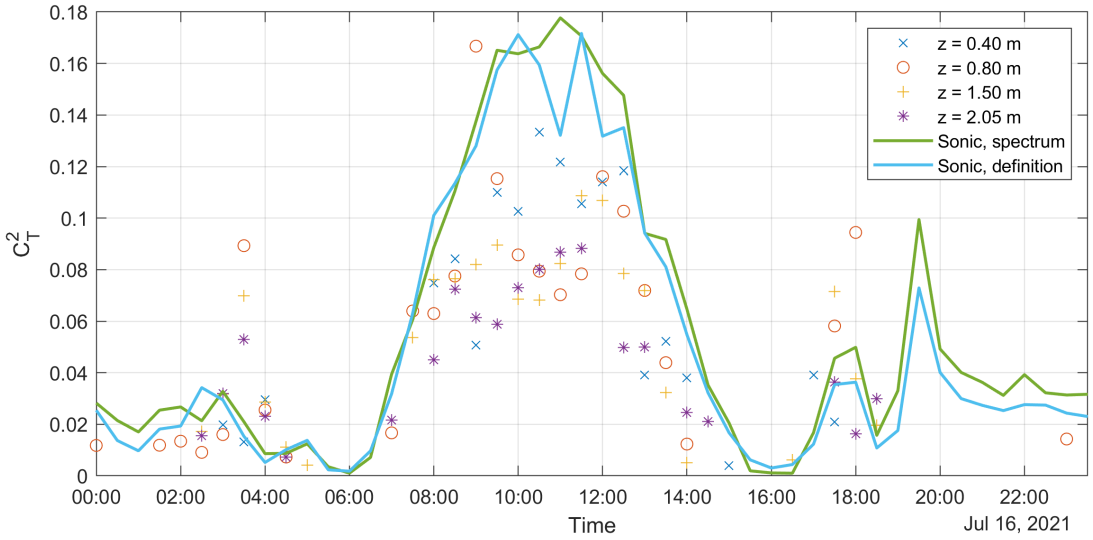

Figure 44.: Structure parameter over time obtained through the DTS spectrum ($C^2_{T,spec}(t)$) for all heights of the turbulence harp. Also plotted are the structure parameters obtained from the sonic anemometer through both the definition and the spectral method.

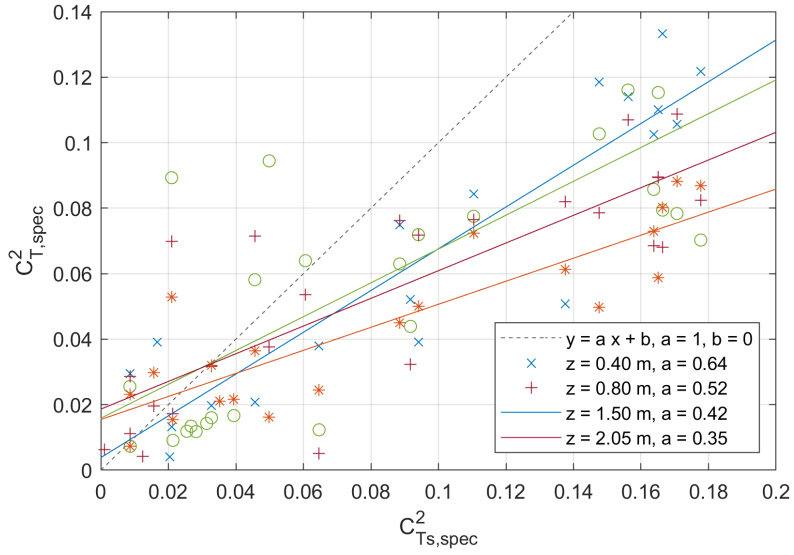

Figure 45.: Correlation between DTS and sonic anemometer for C_T^2 obtained through the spectral method. The dashed line represents a 1-to-1 relation. The four heights of the turbulence harp are plotted with different colours.

10.3. C_T^2 spatial series

10.3.1. Definition method

Switching from the time series to spatial series, in this section results of structure parameters over space are presented. Here, instead of looking at temperature fluctuations over time like in the previous sections, we look at temperature fluctuations across the transect at a point in time. The results here are presented as time series, rather than spatial series, since it appears that over periods longer than several minutes, temperature fluctuations over time dominate those over space.

Structure parameters over a small time scale are displayed in the Appendix in Figure 60 for the four heights of the turbulence harp and several values for r at an arbitrary 5-minute interval over around noon of 16 July. The structure parameters shown in this figure correspond to the temperature contour plots shown in 38 of the raw data section.

Figure 46 shows the 1-minute averaged $C^2_{T,def}(x)$ for several values of r during the transition from nighttime to daytime. The values for the separation distance r were chosen from 1 m to 3.5 m. This was done considering that the distance between the masked poles is approximately 3.7 m, so that gives a maximum separation value. Since the temperature values obtained by DTS are already path-averaged to create a finite resolution, it was chosen to put the minimum value of r at 1 m.

Visible within Figure 46 is a clear change of regime between nighttime and daytime at 9:50 UTC. Before this transition, C_T^2 values for different r always have a large spread. After the transition this changes from the C_T^2 values being spread out to them being very close together. In an ideal scenario, looking only at the inertial range, the C_T^2 values should be independent of r. This seems to happen here only for two spikes in C_T^2 values, at 10:25 and 11:10 UTC.

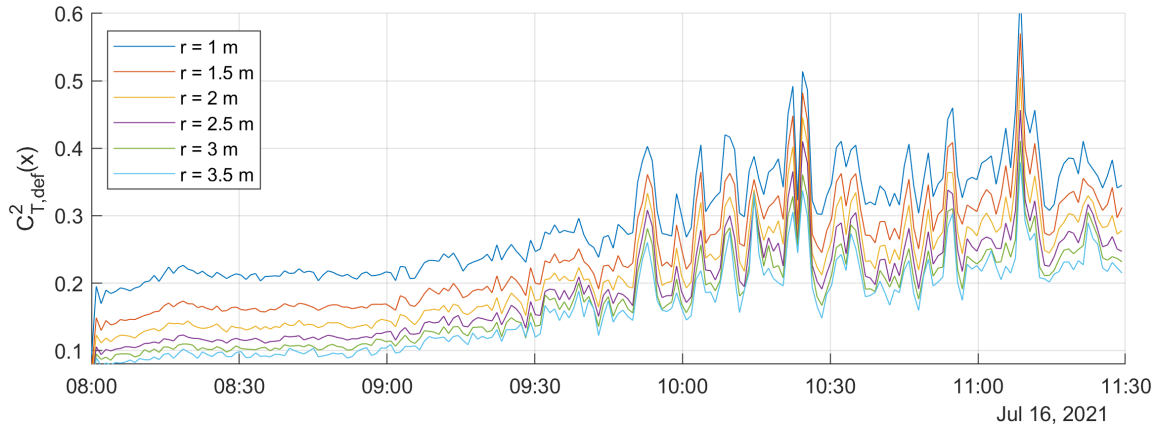

Figure 46.: C_T^2 over space during the sunrise of 16 July for different r

Figure 47 gives an overview of C_T^2 results over the longer term, from both $C_{T,def}^2(x)$ and $C_{T,def}^2(t)$ as well as the results from the sonic anemometer $C_{Ts}^2(t)$. The results displayed in this figure are created from the turbulence harp data at $z = 0.40$ m and for different values of r. Figures 47a and 47b are also included for $z = 2.05$ m in the Appendix as Figures 61 and 61. An important consideration regarding this figure is that the separation distance r is different for space and time. This is a result from both the time and spatial series being constricted by the experiment. The spatial series is constricted up to 4 m because of the spacing of the poles and the time series are constricted to rather large values of r because of the DTS effective sample rate limitations.

In $C_{T,def}^2(x)$ a consistent trend over time is visible of the C_T^2 values for each values of r. Apart from a scaling factor, $C_{T,def}^2(x)$ appears to find similar values for different r, which is an indication of the inertial range being present. This is markedly different from the behaviour of $C_{T,def}^2(t)$, of which the C_T^2 values do follow the same general trend, but with much more variance. Additionally, the distinction between day and night is much less visible in the temporal C_T^2 . The temporal C_T^2 has instances where the nighttime C_T^2 maximum approaches the daytime C_T^2 maximum. Based on Figure 47b it should also be considered that $r = 2$ m is not a suitable separation distance for the temporal C_T^2 , which stipulates again the limitations in terms of high frequency of the DTS.

Comparing the DTS C_T^2 values to the C_T^2 values from the sonic anemometer show that both DTS C_T^2 values manage to find a diurnal pattern. $C_{T,def}^2(x)$ finds a clear diurnal pattern that matches quite well with the sonic anemometer, while in the $C_{T,def}^2(t)$ data a diurnal peak during noon is visible, but not as pronounced. Both DTS C_T^2 values find significantly higher C_T^2 values for nighttime when compared to the sonic anemometer (≈ 0.2 versus ≈ 0.02), which likely are not physical temperature fluctuations.

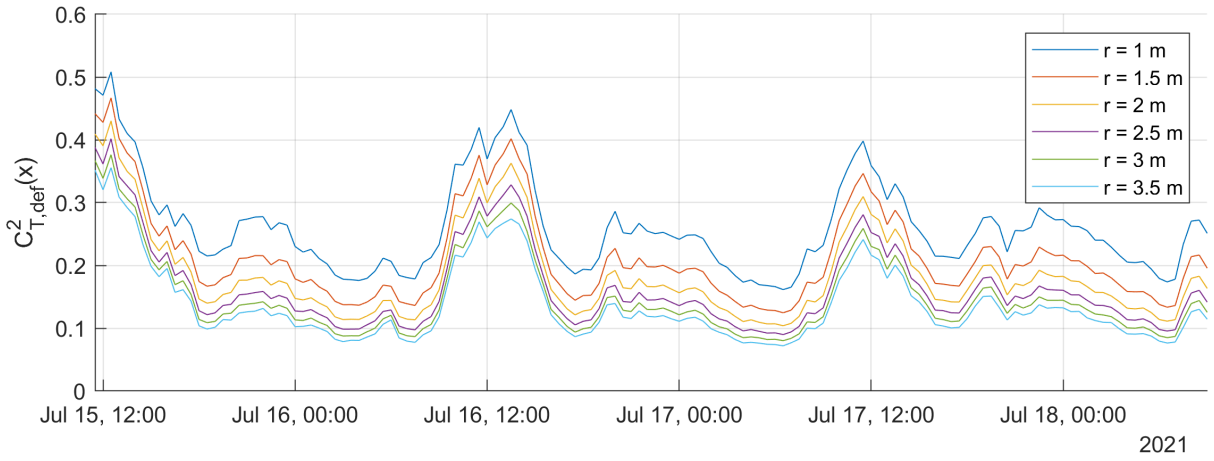

(a) C_T^2 over space from the definition method over several days.

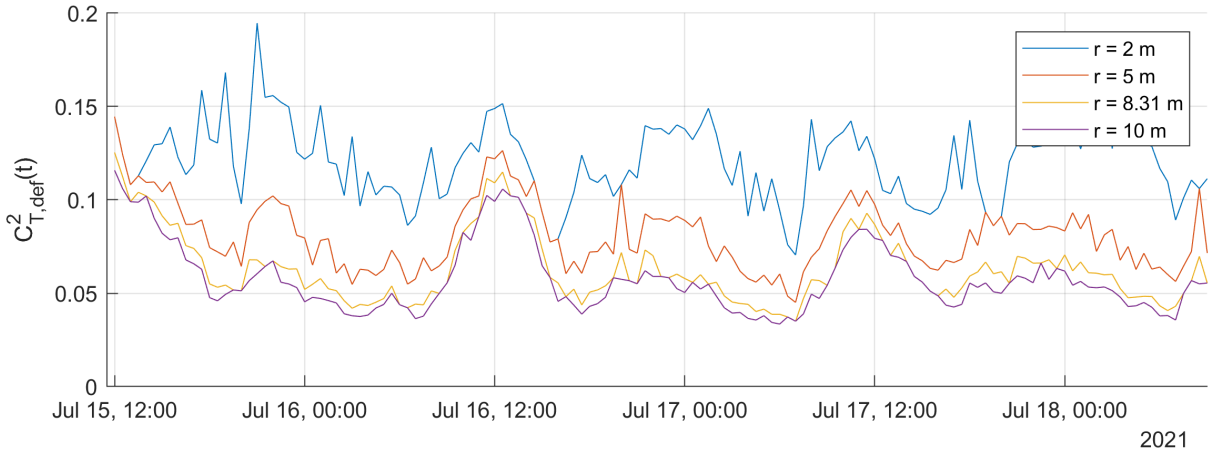

(b) C_T^2 over time from the definition method over several days.

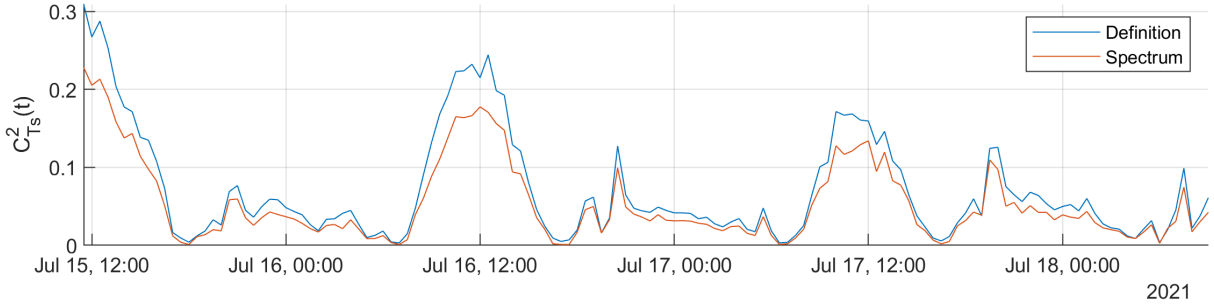

(c) C_T^2 from the sonic anemometer from both methods over several days.

Figure 47.: Comparison of obtained structure parameters over three days. Figure (a) shows $C^2_{T,def}(x)$ as acquired from the method in this section. Figure (b) shows the structure parameters resulting from the same definition method, but then over time. Figure (c) shows the structure parameters obtained from the sonic anemometer as reference.

Rather, it is possible that the structurally higher C_T^2 values during nighttime indicate the instrument noise signal that was also discussed in Section 10.2.1 based on the data in Figure 39. This discussion addressed that the nighttime values for structure parameters are no physical temperature fluctuations, but instead fluctuations introduced by instrument noise. To test this hypothesis an analysis was conducted in which a noise floor e was subtracted from $C_{T,def}^2(x)$. The value of e was determined rudimentary by taking the difference between the minimum C_T^2 values of $C_{T,def}^2(x)$ and $C_{Tsonic,def}^2$. Using this rough approach, e was found to be between 0.07 and 0.16 for r ranging from 1 m to 3.5 m.

The noise floor was subtracted from the original $C_{T,def}^2(x)$ in order to simulate a signal without instrument noise. For r between 1 and 3.5 m this signal was compared to the reference structure parameter. It was found that the minimum mean square error between the reference and $C_{T,def}^2(x) - e$ exists at $r = 3.11$ m. The structure parameters for this separation distance are plotted in Figure 48 along with the reference C_T^2 from the definition method. This figure shows a close match in both trend and scaling of the DTS and the reference structure parameters, which is confirmed considering their correlation, which has an R^2 of 0.88 (Figure 49).

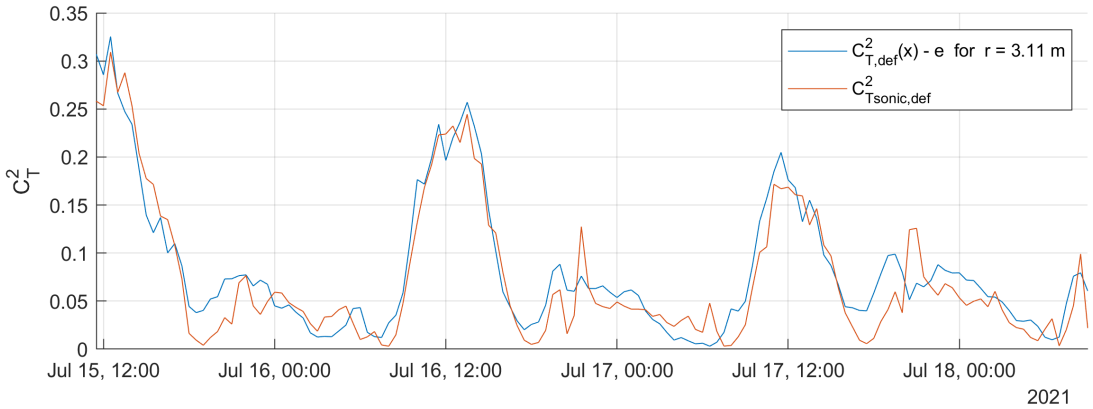

Figure 48.: $C_{T,def}^2(x)$ **without noise floor for** $r = 3.11$ **m,** plotted together with the reference value from the definition method. A constant noise e was subtracted from $C_{T,def}^2(x)$ to remove instrument noise. The value for r with the minimum mean square error between $r = 1$ m and $r = 20$ m was chosen.

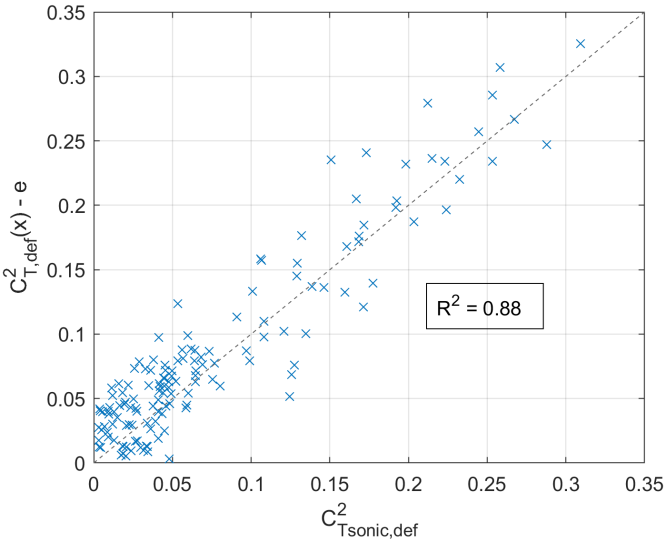

Figure 49.: Correlation between the spatial C_T^2 from the definition method and the reference sonic anemometer C_T^2 . A noise floor e was subtracted from the DTS structure parameter. R^2 was found to be 0.88.

10.4. Spectral method

For the analysis of the spatial series through the spectral method a programming routine has been written around the `nufft.m` function. This routine is necessary because looking when looking at the turbulence harp over space, the poles of the set-up are encountered. These need to be filtered out, resulting in a non-uniform series.

To investigate the effect of a non-uniform data series as opposed to a uniform series, a test was conducted with sonic anemometer data. A temperature time series of 30 minutes from the sonic anemometer was taken at an arbitrary time to use for this test. This time series is shown in the top plot of Figure 50. In order to create a non-uniform time series, 14 sections were removed at a regular interval from the original time series, similar to the spatial series from the turbulence harp. This results in the time series shown in the bottom plot of Figure 50.

Figure 51 displays the difference in spectra between the uniform and the non-uniform dataset. The top plot of 51 corresponds to the time series of the top plot of 50, and the bottom plots of both figures correspond to the non-uniform series. Overal the spectrum characteristics remains equivalent, but there are changes in the spectrum. Specifically, the non-uniform spectrum introduces peaks in temperature variance, in this example along 1 Hz and 2 Hz. This seems to be a typical flaw of the non-uniform Fourier transform introduced by the inherent periodicity of the non-uniform time series. These peaks have been found consistently throughout multiple spacing and data series.

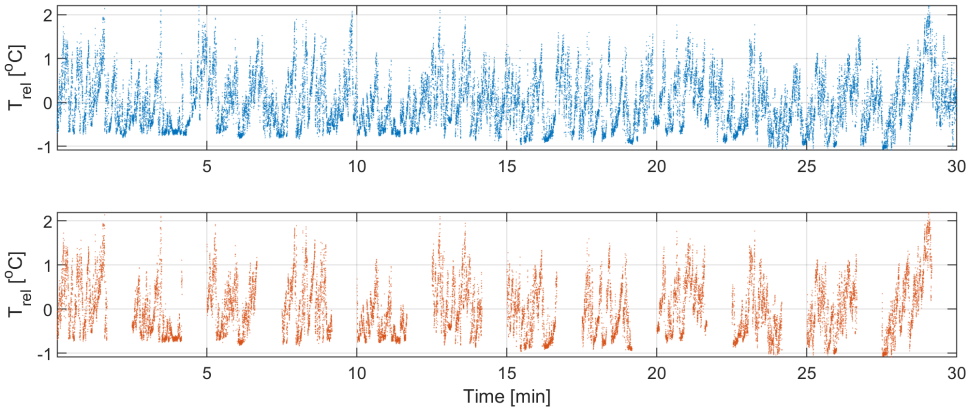

Figure 50.: Uniform and non-uniform sonic anemometer data for an arbitrary 30 minutes.

While the routine for determining spectra using non-uniform time series is shown to work for the sonic anemometer, it has not yet given meaningful results concerning the turbulence harp dataset. Two preliminary spectra are displayed in this section, in Figure 52 and 53. Figure 52 displays the spectra of 10 consecutive points along the transect (at $z = 0.40$ m), with the solid black line giving a smoothed moving average. Figure 53 shows the same spectra, but then for all the points along the spectrum. Both figures clearly do not show an inertial range and should be taken as preliminary results. At the time of writing, it is yet undecided whether there is a computational problem or if the problem lies within the limits of the DTS data acquisition.

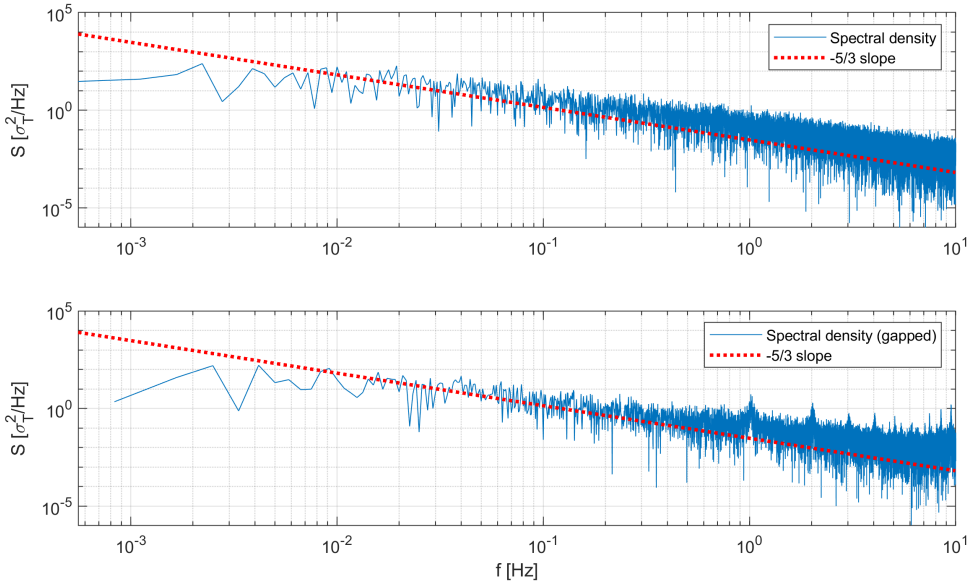

Figure 51.: Sonic anemometer spectra of uniform and non-uniform temperature series. Top plot shows the spectrum of the original uniform dataset, bottom plot shows the spectrum of an artificial non-uniform dataset.

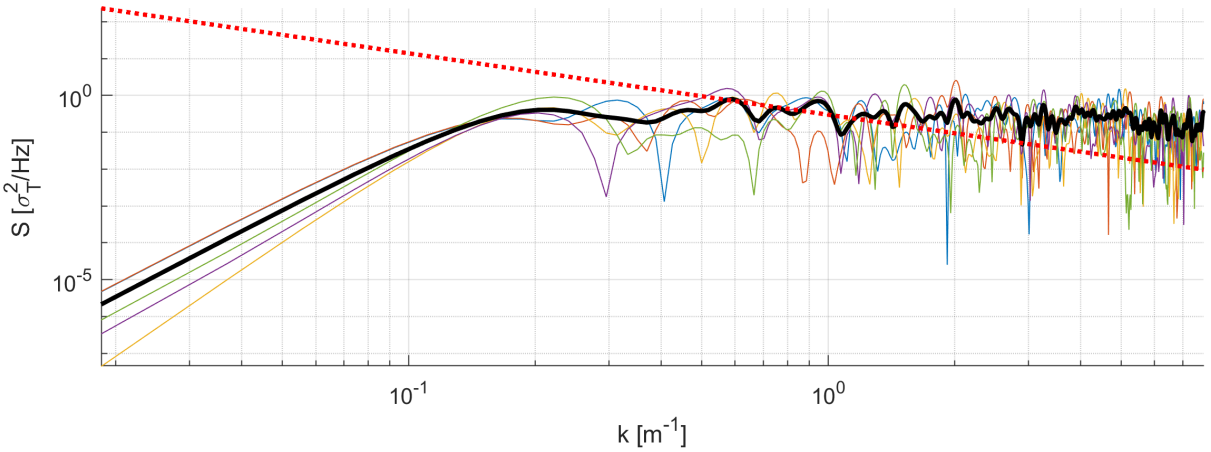

Figure 52.: Spatial non-uniform spectrum for 10 consecutive points on the transect (z = 0.40 m). The thick black line indicates the average spectrum and the dashed red line the -5/3 slope.

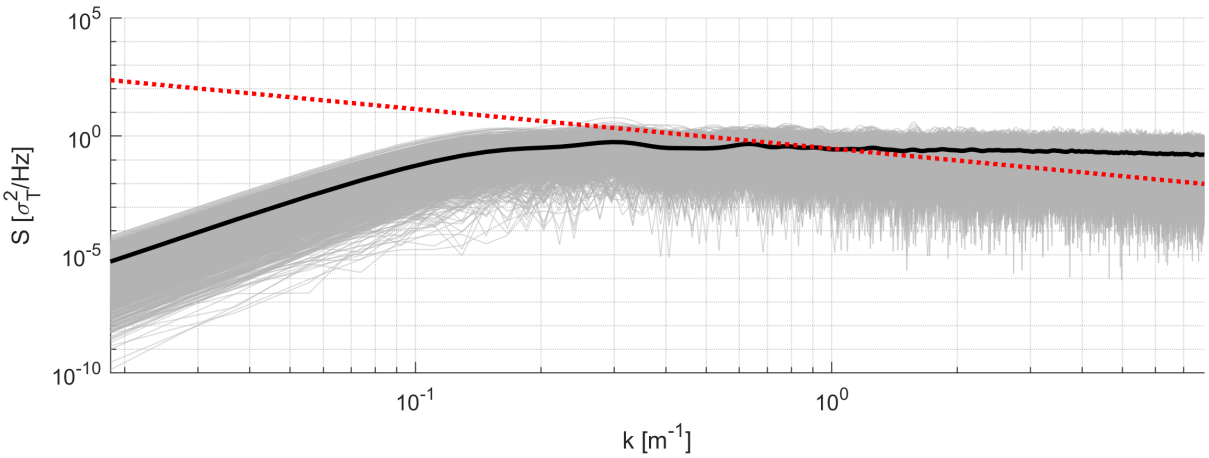

Figure 53.: Spatial non-uniform spectrum for all points on the transect (z = 0.40 m). The thick black line indicates the average spectrum and the dashed red line the -5/3 slope.

11. Discussion of Part 2

Similar to Part 1, this discussion is an addition to the points that were brought up in the previous chapter. The design of the experiment will be discussed, as well as an outlook on further research.

11.1. Design of the set-up

The turbulence harp set-up was the largest and the most labour-intensive set-up of the four DTS set-ups. The amount of labour was mostly due to the metal poles that were used and guiding and securing the thin fiber through the set-up. In the design metal poles were chosen, since a height of 2 m needed to be achieved, with the construction also be put under tension. A lot of effort was needed to get the poles into the ground, but after that it did create a rigid construction.

The downside of this rigidity is the large thermal mass that the 2.5 cm diameter solid iron poles have. This caused the poles to be large hot spots in the measurements, radiating out so much that it was noticeable up to 60 cm away by the fiber. Because of this 22% of the data along the transects of the turbulence harp had to be filtered out. On its own this is not a critical problem, since the use of poles inherently means that data has to be filtered out, resulting in a non-uniform temperature series. However, the extent to which attachment points of the fiber influence environmental temperature measurements is something to take into account for future DTS measurements. In this situation, an alternative could have been to for instance use hollow metal poles so that there is less mass to radiate heat. The solid metal poles are also a significant resource to bring on a campaign, weighing approximately 200 kg.

Significant effort was put into guiding the fragile fiber carefully and securing it without damaging it (Figure 57). This was done to great success, since the fiber has not broken once during the campaign, resulting in an uninterrupted time series of 8 days of measurements. A suggestion for improvement would be to look into a better solution for guiding the length of fiber that connects two heights (Figure 57d). While the horizontal length of fiber should be kept under tension to keep it level and avoid it fluttering with the wind, the vertical lengths connecting it should be under little tension to avoid sharp corners (Figure 57e). In this experiment this was achieved iteratively on the first campaign day by tightening clamps and dividing fiber length accordingly. It would however be good to think of a more elegant construction for this.

The single-ended configuration of the turbulence harp contains two reference baths after which the fiber runs to the set-up. An improvement to this configuration would be to include an extra reference section for validation purposes, as is also described in Hausner et al. (2011). For future (atmospheric) DTS measurements, it is recommended to have three reference sections for each section of fiber (so for each length of fiber between two splices) whenever possible. This can either be done by running the fiber back to a previous calibration bath in a duplex configuration or by adding another calibratin bath.

11.2. Capturing the inertial range

The design of this set-up was committed to use a single-ended configuration, since the goal was to measure turbulent fluctuations. To capture as much as possible of the turbulent spectrum, the fastest possible sampling rate is therefore desired. Therefore the sample rate was set at 1 Hz, which together with

processing time creates an effective sample rate f_s of approximately 0.85 Hz. f_s was calculated for every 30 minute interval, according to the processing strategy.

Since the processing time differs slightly for each measurement, this results in f_s being slightly different for each 30 minutes of data. The dataset therefore has different time intervals per 30 minutes, which is not ideal for creating an accessible dataset. This choice was made for this analysis, since there is a trade-off here. On the one hand, a consistent sampling rate over the whole analysis period is preferred, but this comes at the cost of accuracy in sampling rate at smaller time periods. On the other hand, the period over which C_T^2 is determined must have linearly-spaced time, so the original timestamps, which do not have equal spacing, cannot be used.

However, the actual sampling frequency f_a of the turbulence harp does not seem to be limited by the sample rate f_s. f_a is a combination of both the sampling rate f_s and the response time of the fiber. Since the fiber has a certain mass and finite size, it has a heat capacity and will therefore need time to change temperature according to environmental temperature changes. For this set-up, already a thinner fiber was chosen to take the response time into the scale of seconds.

Both the definition and spectral methods of the time series analysis suggest that f_a is smaller than f_s. The inertial range found through the DTS using the spectral method begins at approximately 0.04 Hz, which corresponds to the start of the inertial range found by the sonic anemometer. However, for all four heights of the turbulence harp, the -5/3 slope flattens out rather quickly, around 0.1 - 0.2 Hz (Figure 43), whereas this is not the case for the sonic anemometer. This suggests that at frequencies above 0.15 Hz, the obtained signal from the DTS changes from being dominated by the inertial range to being dominated by noise. The results from the definition method add to this suggestion, with the underestimation of C_T^2 during daytime. Structure parameters found with this method are approximately half of the sonic anemometer reference, suggesting that perhaps only half of the inertial range is captured. With these findings a conclusion can be drawn that with this current set-up it is possible to sample turbulence up to $f_a = 0.15$ Hz, rather than the 1 Hz the experiment was designed for.

A readily-available solution is the replacement of the 0.5 mm acrylic cable by a thinner cable, such as 0.25 mm acryllic or 0.20 mm naked fibers that are available. Considering that over the period of the campaign the 0.5 mm cable has not broken once, the trade-off between fragility and response time could be put more towards response time for future campaigns investigating turbulence with DTS.

11.3. Outlook on further research

The original reason for bringing distributed temperature sensing to the LIAISE campaign was to look into using DTS for complementing scintillometer heat fluxes with spatial data. The comparison to scintillometer measurements has not been achieved within the scope of this study, but is something that should definitely be considered for future studies. The turbulence set-up was designed with the intention of the DTS capturing the same footprint as the scintillometer. A combination of the two instruments could then combine the high frequency measurements of the scintillometers with the spatial information of DTS within the same footprint.

The principle measurement height of the turbulence harp was designed at $z = 2.05$ m, since that heigh corresponds to the height of the scintillometer. The remaining three heights were added as additional measurement points. However, for the analysis in this work mostly the lowest height of $z = 0.40$ m was used. This was done because the temperature fluctuations were strongest at that height, making determining C_T^2 the most convenient. This can also be seen in the time series C_T^2 analysis, where $z = 0.40$ m has the strongest correlation with the structure parameters obtained from the sonic anemometer.

The determination of C_T^2 over time and space using the definition method yielded notable differences, as visible in Figure 47. The temporal C_T^2 roughly follows a diurnal trend for $r = 5$ m and larger, while the spatial C_T^2 shows a clear consistency between structure parameters found for different r. An important point to be made here is that the spatial C_T^2 is an independent measurement, whereas the temporal C_T^2

is not. This is displayed in the workflow in Figure 33, which shows that the spatial methods rely purely on DTS measurements, while the time series methods also need the horizontal wind speed, in this case from a sonic anemometer.

This difference in independence between time and space, caused by Taylor's frozen turbulence hypothesis, might be the principle reason why the spatial C_T^2 show clear structure over time while the temporal C_T^2 do so only in a lesser extent. The use of a 30 min averaged horizontal wind speed from another instrument could very well be the reason why the temporal C_T^2 ($C_{T,def}^2(t)$) shows a lack of consistent trends over time for different r. The spatial C_T^2 ($C_{T,def}^2(x)$) does not need addition of an external instrument and purely relies on the temperatures as measured in the fiber. A possible idea for further research would be to look for corrections to transform the temporal C_T^2 into a more useable time series, similar to what has been done to the spatial C_T^2 and resulted in Figures 48 and 49.

As an additional option for further research, the profile of C_T^2 could be used to estimate the friction velocity u_*. Using the four heights of the turbulence harp, structure parameters for different heights can be calculated. Using that C_T^2 scales with $z^{-2/3}$ for unstable conditions, the C_T^2 -profile approach can be applied to calculate the Obukhov length, which can be used to determine u_*. Developing a routine for this would create a u_* with containing spatial information, adding onto path-averaged C_T^2 obtained from scintillometer measurements (Nieveen and Green, 1999).

12. Conclusions of Part 2

The goal of Part 2 was to perform an analysis on whether it is possible to resolve temperature turbulence values using distributed temperature sensing. Specifically, the question was asked whether turbulent information can be found over both space and time, of which the determination over space is a novel method. The turbulent information was quantified by the structure parameter C_T^2 , which characterizes the intensity of temperature fluctuations occurring within a certain path length. Both the definition of the structure parameter (the definition method) and the -5/3 power law from the inertial range in the turbulent spectrum (the spectral method) were used to determine C_T^2 . A sonic anemometer was used as a reference instrument in determining the structure parameter.

A single-ended fiber-optic set-up with a thin 0.5 mm cable was designed for this end. This set-up, called the turbulence harp, had a vertical extent of 2.05 m and a horizontal extent of 70 m, measuring at heights of $z = 2.05$ m, 1.50 m, 0.80 m and 0.40 m. The set-up measured at 1 s and 12.7 cm resolution and was able to capture spatial temperature difference over the horizontal. The actual sampling frequency appeared to be 0.15 Hz, rather than the designed 1 Hz rate, causing the inertial range to not be fully sampled by the designed DTS set-up. However, enough of the temperature turbulence spectrum was captured to obtain structure parameters and turbulent information.

The temporal C_T^2 were found to roughly follow a diurnal cycle, for separation distance $r > 2$ m, but with significant variation. This could be due to the necessity of using an external horizontal wind speed for determining C_T^2 , making it not an independent measurement. Compared to the reference dataset, the results from the definition method underestimated during daytime and overestimated during nighttime. The daytime underestimation is assumed to be caused by the actual sampling frequency being too small to capture all turbulent fluctuations. The nighttime overestimation is likely caused by DTS measurement noise introducing artificial temperature fluctuations. The effectiveness of the spectral method was limited due to the small extent of the inertial range. Therefore detection of C_T^2 was difficult. The spectral method did produce a better correlation with the reference C_T^2 , with a slope 50% closer.

Using the definition method on the spatial data yielded C_T^2 values with clear structure for different values of r between 1 and 3.5 m. Structure parameters for $r = 3.11$ m have the closest resemblance to the reference data set when looking at the RMSE. By applying a correction for the noise floor, a good correlation ($R^2 = 0.88$) has been found between the reference dataset and C_T^2 obtained through the definition method over space. This illustrates that the novel method of using fiber-optics to measure spatial characteristics of turbulence has potential to be used in further research. An attempt was made to obtain C_T^2 through the spectral method over space, but results are as of yet not conclusive.

It was possible to determine structure parameters in this work using DTS temperature measurements. The resulting turbulent parameters from the spatial series showed significantly more structure than those of the time series methods. This is likely due to the inclusion of sonic anemometer data for the horizontal wind speed in the time series method. These results suggest that either the use of a separate instrument to include horizontal wind speed is not valid, or that Taylor's hypothesis is not strictly applicable within the spatio-temporal dimensions used in this DTS set-up.

Future recommendations concerning this work are to further investigate the effects of instrument noise and the limited sampling frequency on the determination of C_T^2 . A further look into the determination of C_T^2 via the spectral method over space is also encouraged. The results from this analysis can be further developed into potentially obtaining spatially resolved friction velocities and heat fluxes. For future campaigns it is recommended to investigate into the possibility of using thinner cables for a faster response time, and it is strongly suggested to critically look into the calibration strategy.

Bibliography

PJ Van Oevelen, Roy Rasmussen, Jan Polcher, and Alex C Ruane. The world climate research programme grand challenge on water for the food baskets in the world. In *100th American Meteorological Society Annual Meeting*. AMS, 2020.

J. Cos, F. Doblas-Reyes, M. Jury, R. Marcos, P.-A. Bretonnière, and M. Samsó. The mediterranean climate change hotspot in the cmip5 and cmip6 projections. *Earth System Dynamics*, 13(1):321–340, 2022. doi: 10.5194/esd-13-321-2022. URL `https://esd.copernicus.org/articles/13/321/2022/`.

Aaron Boone. Land surface Interactions with the Atmosphere over the Iberian Semi-arid Environment (LIAISE), April 2019. URL `https://hal.archives-ouvertes.fr/hal-02392949`. Quarterly Newsletter of The Global Energy and Water cycle Exchanges (GEWEX) project which is dedicated to understanding Earth's water cycle and energy fluxes at the surface and in the atmosphere.

Arnold F Moene, Frank Beyrich, and Oscar K Hartogensis. Developments in scintillometry. *Bulletin of the American Meteorological Society*, 90(5):694–698, 2009.

John S. Selker, Luc Thévenaz, Hendrik Huwald, Alfred Mallet, Wim Luxemburg, Nick van de Giesen, Martin Stejskal, Josef Zeman, Martijn Westhoff, and Marc B. Parlange. Distributed fiber-optic temperature sensing for hydrologic systems. *Water Resources Research*, 42(12), 2006. doi: https://doi.org/10.1029/2006WR005326. URL `https://agupubs.onlinelibrary.wiley.com/doi/abs/10.1029/2006WR005326`.

Christoph K Thomas, Adam M Kennedy, John S Selker, Ayla Moretti, Martin H Schroth, Alexander R Smoot, Nicholas B Tufillaro, and Matthias J Zeeman. High-resolution fibre-optic temperature sensing: A new tool to study the two-dimensional structure of atmospheric surface-layer flow. *Boundary-layer meteorology*, 142(2):177–192, 2012.

Scott W Tyler, John S Selker, Mark B Hausner, Christine E Hatch, Thomas Torgersen, Carl E Thodal, and S Geoffrey Schladow. Environmental temperature sensing using raman spectra dts fiber-optic methods. *Water Resources Research*, 45(4), 2009.

Jonathan G Izett, Bart Schilperoort, Miriam Coenders-Gerrits, Peter Baas, Fred C Bosveld, and Bas JH van de Wiel. Missed fog? *Boundary-layer meteorology*, 173(2):289–309, 2019.

B. Schilperoort, M. Coenders-Gerrits, W. Luxemburg, C. Jiménez Rodríguez, C. Cisneros Vaca, and H. Savenije. Technical note: Using distributed temperature sensing for bowen ratio evaporation measurements. *Hydrology and Earth System Sciences*, 22(1):819–830, 2018. doi: 10.5194/hess-22-819-2018. URL `https://hess.copernicus.org/articles/22/819/2018/`.

Rainer V. J. Hilland, Christian Bernhofer, May Bohmann, Andreas Christen, Marwan Katurji, Gillian Maggs-Kölling, Matthias Krauß, Jarl A. Larsen, Eugene Marais, Andrea Pitacco, Benjamin Schumacher, Robert Spirig, Nadia Vendrame, and Roland Vogt. The namib turbulence experiment: Investigating surface–atmosphere heat transfer in three dimensions. *Bulletin of the American Meteorological Society*, 103(3):E741 – E760, 2022. doi: 10.1175/BAMS-D-20-0269.1. URL `https://journals.ametsoc.org/view/journals/bams/103/3/BAMS-D-20-0269.1.xml`.

M.-L. Zeller, J.-M. Huss, L. Pfister, K. E. Lapo, D. Littmann, J. Schneider, A. Schulz, and C. K. Thomas. The ny-Ålesund turbulence fiber optic experiment (nytefox): investigating the arctic boundary layer, svalbard. *Earth System Science Data*, 13(7):3439–3452, 2021. doi: 10.5194/essd-13-3439-2021. URL `https://essd.copernicus.org/articles/13/3439/2021/`.

K. Lapo, A. Freundorfer, L. Pfister, J. Schneider, J. Selker, and C. Thomas. Distributed observations of wind direction using microstructures attached to actively heated fiber-optic cables. *Atmospheric Measurement Techniques*, 13(3):1563–1573, 2020. doi: 10.5194/amt-13-1563-2020. URL `https://amt.copernicus.org/articles/13/1563/2020/`.

V.F. Bense, T. Read, and A. Verhoef. Using distributed temperature sensing to monitor field scale dynamics of ground surface temperature and related substrate heat flux. *Agricultural and Forest Meteorology*, 220:207–215, 2016. ISSN 0168-1923. doi: https://doi.org/10.1016/j.agrformet.2016.01.138. URL `https://www.sciencedirect.com/science/article/pii/S0168192316301496`.

S. C. Steele-Dunne, M. M. Rutten, D. M. Krzeminska, M. Hausner, S. W. Tyler, J. Selker, T. A. Bogaard, and N. C. van de Giesen. Feasibility of soil moisture estimation using passive distributed temperature sensing. *Water Resources Research*, 46(3), 2010. doi: https://doi.org/10.1029/2009WR008272. URL `https://agupubs.onlinelibrary.wiley.com/doi/abs/10.1029/2009WR008272`.

Arnold F Moene and Jos C Van Dam. *Transport in the atmosphere-vegetation-soil continuum*. Cambridge University Press, 2014.

Xiaoyi Bao and Liang Chen. Recent progress in distributed fiber optic sensors. *Sensors*, 12(7):8601–8639, 2012. ISSN 1424-8220. doi: 10.3390/s120708601. URL `https://www.mdpi.com/1424-8220/12/7/8601`.

Mark B Hausner, Francisco Suárez, Kenneth E Glander, Nick Van de Giesen, John S Selker, and Scott W Tyler. Calibrating single-ended fiber-optic raman spectra distributed temperature sensing data. *Sensors*, 11(11):10859–10879, 2011.

Bas des Tombe, Bart Schilperoort, and Mark Bakker. Estimation of temperature and associated uncertainty from fiber-optic raman-spectrum distributed temperature sensing. *Sensors*, 20(8), 2020. ISSN 1424-8220. doi: 10.3390/s20082235. URL `https://www.mdpi.com/1424-8220/20/8/2235`.

K Lapo and A Freundorfer. pyfocs v0.5. Zenodo: Genève, Switzerland, 2020. `https://github.com/klapo/pyfocs`.

Bart Schilperoort, Karl Lapo, Anita Freundorfer, and Bas des Tombe. Untangling fiber optic distributed temperature sensing: Getting the right temperature and getting there smoothly. In *EGU General Assembly Conference Abstracts*, page 7821, 2020.

B Schilperoort. *Heat Exchange in a Conifer Canopy: A Deep Look using Fiber Optic Sensors*. PhD thesis, Delft University of Technology, 2022.

Bart Schilperoort. Dts soil coil, 2020. `https://github.com/BSchilperoort/dts_soil_coil/`.

Christoph K Thomas, Jannis-Michael Huss, Mohammad Abdoli, Tim Huttarsch, and Johann Schneider. Solid-phase reference baths for fiber-optic distributed sensing. *Sensors*, 22(11):4244, 2022.

Nick Van De Giesen, Susan C Steele-Dunne, Jop Jansen, Olivier Hoes, Mark B Hausner, Scott Tyler, and John Selker. Double-ended calibration of fiber-optic raman spectra distributed temperature sensing data. *Sensors*, 12(5):5471–5485, 2012.

B. T. Neilson, C. E. Hatch, Q. G. Bingham, and S. W. Tyler. Effect of Solar Radiation on Fiber Optic Cables Used in Distributed Temperature Sensing (DTS) Applications. In *AGU Fall Meeting Abstracts*, volume 2008, pages H51H–0970, December 2008.

John C Wyngaard. *Turbulence in the Atmosphere*. Cambridge University Press, 2010.

Oscar Hartogensis. *Exploring scintillometry in the stable atmospheric surface layer*. Wageningen University and Research, 2006.

Roland B Stull. *An introduction to boundary layer meteorology*, volume 13. Springer Science & Business Media, 1988.

JP Nieveen and AE Green. Measuring sensible heat flux density over pasture using the ct2-profile method. *Boundary-Layer Meteorology*, 91(1):23–35, 1999.

A. Raw powers, temperatures and LAF

LAF **[m]**	**Location**	**Comment**
0	DTS computer	Pigtail connection to computer
1.873	Begin indoor bath	**Only from 21 July onwards**
10.483	End indoor bath	
110.416	Begin 50 m mast	at z = 1.6 m
149.055	Top 50 m mast	at z = 40 m
187.947	End 50 m mast	at z = 1.6 m
374.530	Begin warm outdoor bath	
380.276	End warm outdoor bath	
381.393	Splice	From 50 m mast to ground coil
381.901	Begin warm outdoor bath	
421.048	End warm outdoor bath	
423.082	Begin cold outdoor bath	
439.096	End cold outdoor bath	
448.502	Begin ground coil	at z = -46.25 cm
459.432	End ground coil	at z = 8.75 cm
468.075	Begin cold outdoor bath	
484.089	End cold outdoor bath	
486.123	Begin warm outdoor bath	
524.253	End warm outdoor bath	
525.778	Splice	From ground coil to canopy harp
526.032	Begin warm outdoor bath	
546.114	End warm outdoor bath	
547.193	Begin cold outdoor bath	
564.416	End cold outdoor bath	
572.551	Begin canopy harp	
595.174	End canopy harp	Also end of fiber

Table 1.: Table of physical locations corresponding to LAF-values from the vertical set-ups.

LAF [m]	Location	Comment
0	DTS computer	Pigtail connection to computer
144.5	Splice	To thinner cable
154	Begin warm outdoor bath	
181	End warm outdoor bath	
184	Begin cold outdoor bath	
205	End cold outdoor bath	
265.729	Begin turbulence harp	at $z = 2.05$ m
336.0	End turbulence harp	at $z = 2.05$ m
336.5	Begin turbulence harp	at $z = 1.50$ m, **direction reversed**
406.5	End turbulence harp	at $z = 1.50$ m
407.1	Begin turbulence harp	at $z = 0.80$ m
407.4	End turbulence harp	at $z = 0.80$ m
477.35	Begin turbulence harp	at $z = 0.40$ m, **direction reversed**
547.636	End turbulence harp	at $z = 0.40$ m

Table 2.: Table of physical locations corresponding to *LAF*-values from the horizontal (turbulence harp) set-up.

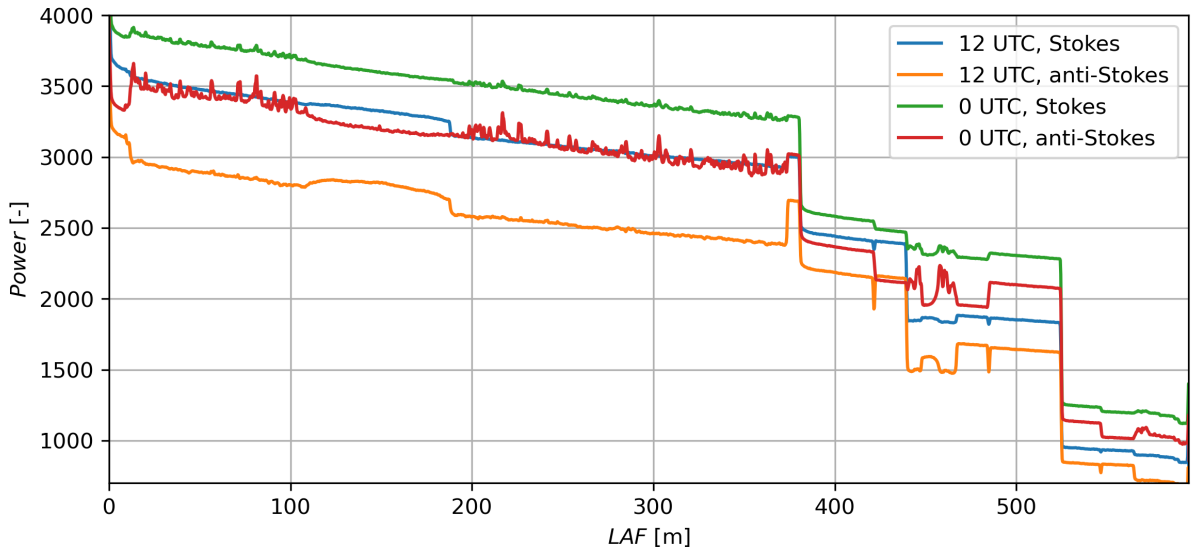

Figure 54.: Single (5 s) measurement of raw power for the vertical set-up. Both the Stokes and anti-Stokes component are shown for 19 July 12 UTC and 0 UTC.

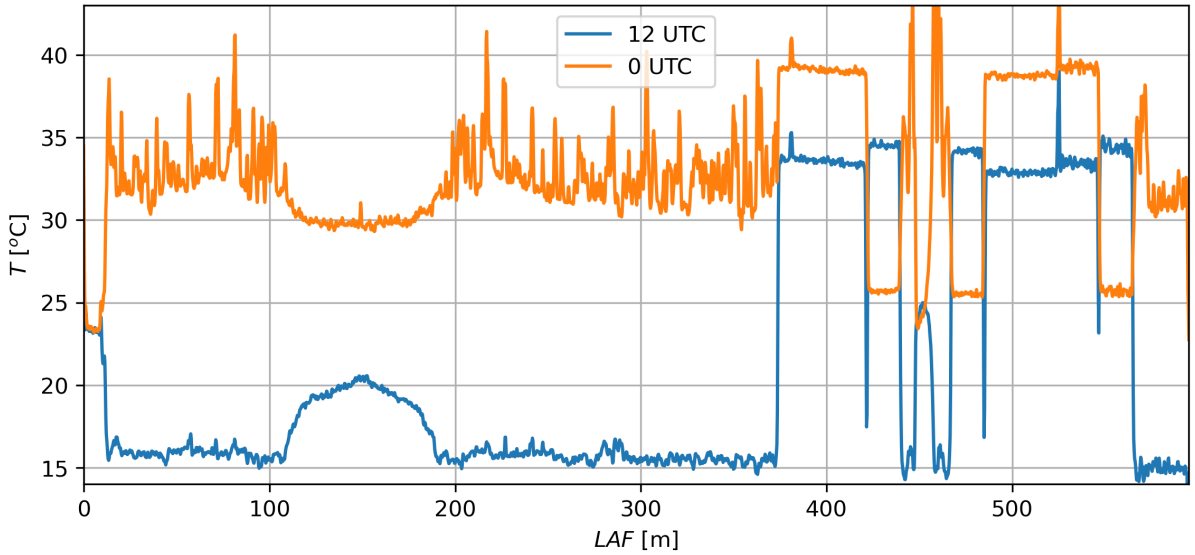

Figure 55.: Single (5 s) measurement of temperatures for the vertical set-up. Temperatures are calculated from as a ratio of the Stokes and anti-Stokes powers in Figure . The fiber runs from left to right in the figure from the Cabin (0 m), the 50 m mast (100 - 200 m), the outdoor calibration baths (350 m - 550 m), the ground coil (around 450 m) and the canopy harm (550 - 600 m). Exact values for the LAF of the set-ups can be found in Table 1.

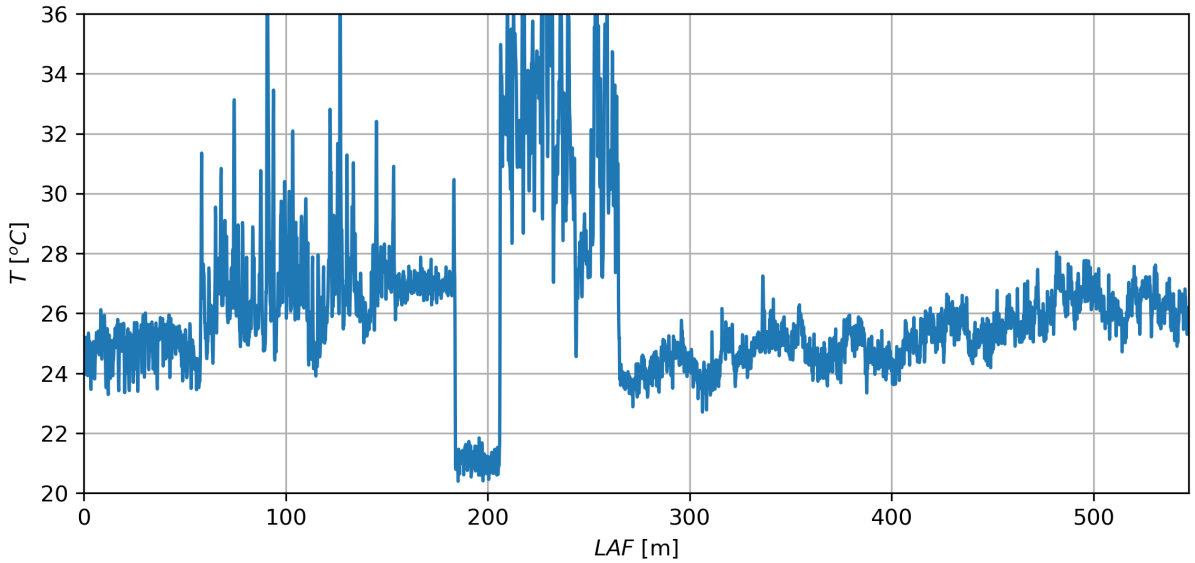

Figure 56.: Single (1 s) measurement of temperatures for the horizontal set-up. Calibration baths are located between LAF values of 150 m and 210 m, the turbulence harp is located from 260 m onwards. Exact values for the LAF of the set-ups can be found in Table 2.

B. Securing and guiding of fibers

(a) Foam combined with cable ties or hose clamps to used to keep the fibers in place without damaging them.

(b) Fiber position secured by clamped foam, with spare length of cable present in the field in case of fiber break.

(c) Cable secured by clamped foam and protected by garden hose from chafing on hard objects.

(d) Hose clamps keeps tension on the horizontal stretch of fiber while allowing for slack on the vertical part.

(e) Foam piece prevents a sharp right angle of the fiber on a connecting corner.

(f) Clamped foam secure the bottom of the mast set-up. Markers with tape are used to detect slippage.

Figure 57.: Collection of examples about the securing and guiding of fibers. Clamped pieces of foam were used to keep fibers securely on their place without damaging the fiber. Cut-open garden hose was used to prevent chafing of the fiber. There was spare fiber length coiled up in the field to be able to repair possible fiber breaks. To detect possible slippage markers were made with tape on key locations.

C. Data log

	Day	Time	Set-up				Comment
#	*Calendar*	*(LT)*	*50 m mast*	*Ground coil*	*Canopy harp*	*Turbulence harp*	
1	July 15	7:03:52				on	Test run
		9:57:20				off	
		11:56:12				on	
		19:50:27	on	on			Some data before this with different settings
2	July 16	4:57:11					Fiber break after ground coil
		14:13:00					Ice packs added for cooling
		15:30:00					TidBits deployed (5 min resolution)
3	July 17	8:25:00					Ice packs added for cooling
		12:29:40	off	off			Turned off for splicing
		13:16:36	on	on	on		
		15:33:13	off	off	off		
		15:37:20	on	on	on		
		16:02:51	off	off	off		
		16:05:47	on	on	on		
4	July 18	2:37:01			broken		Fiber break at LAF = 527 m
		9:39:58	off	off	off		Turned off for splicing
		9:57:49	on	on	on		
		10:14:00					Ice packs added for cooling
		11:14:21				off	missing data for unknown reason
5	July 19	0:00:00				on	missing data for unknown reason
		9:30:00					Ice packs added for cooling
6	July 20	10:23:00					Ice packs added for cooling
7	July 21	8:34:00					Ice packs added for cooling
		14:30:00					TidBits removed
8	July 22	8:28:00					Ice packs added for cooling
		12:20:49				off	Heat wave precaution
		14:10:46	off	off	off		Heat wave precaution
		15:52:03	on	on	on		
		15:54:17				on	
9	July 23	9:09:38				off	Heat wave precaution
		9:13:19	off	off	off		Heat wave precaution
10	July 24						
11	July 25						
12	July 26	9:02:30					Datalogger failure
		9:10:48	on	on	on		
		10:55:00					Ice packs added for cooling
		11:08:10				on	
13	July 27	12:53:00					Ice packs added for cooling
14	July 28	10:00:00					TidBits deployed (10 s resolution)
		10:00:00					Ice packs added for cooling
		14:01:54				off	End of measurement
15	July 29	11:24:00					Ice packs added for cooling
16	July 30	7:38:14	off	off	off		
		8:15:00					TidBits removed

D. 10 minute analysis

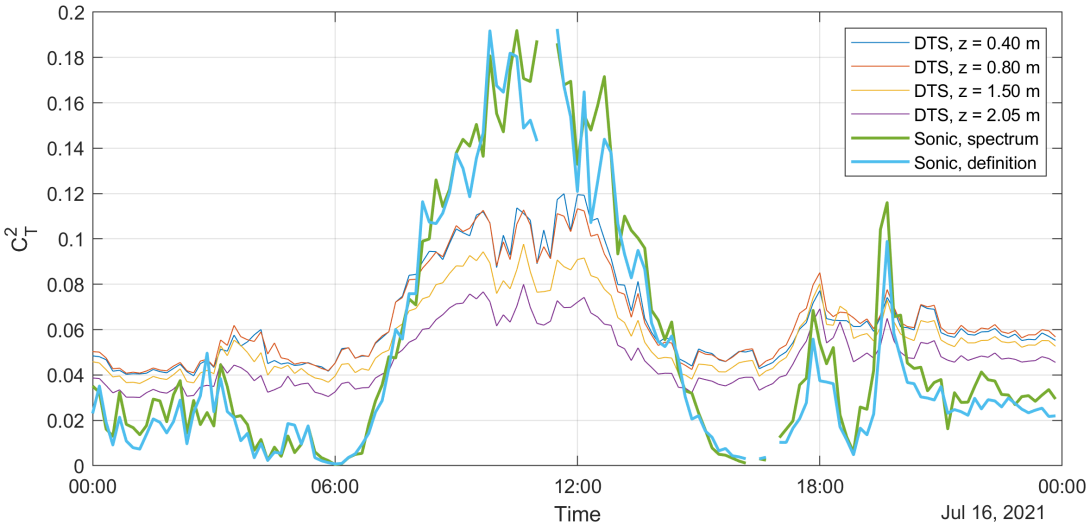

Figure 58.

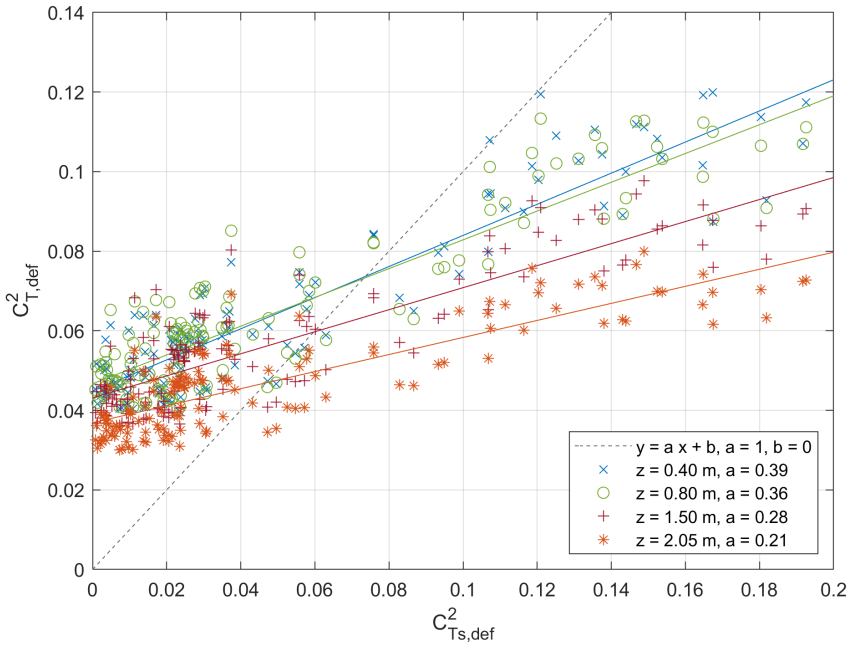

Figure 59.

E. Spatial series - Definition method, additional figures

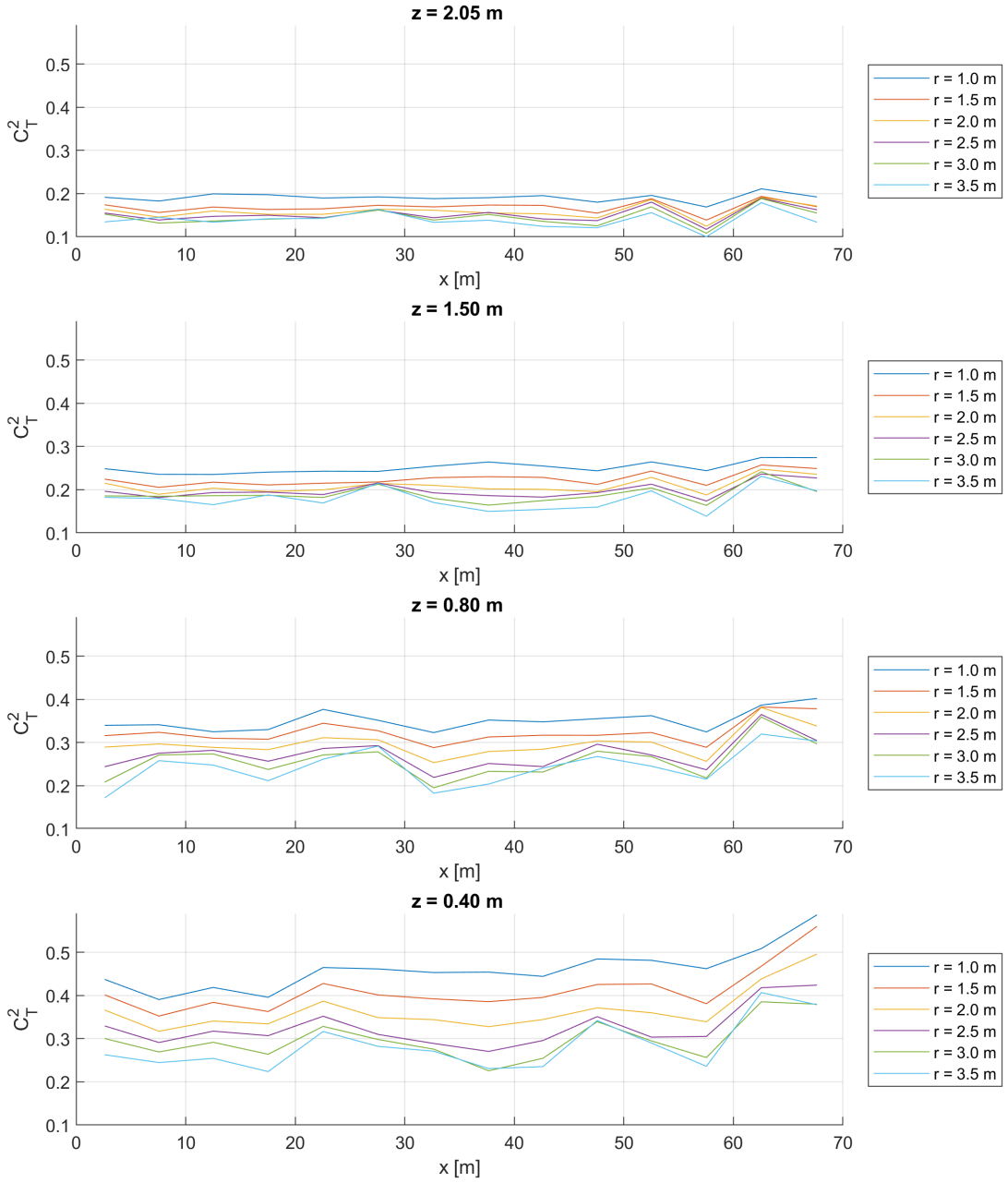

Figure 60.

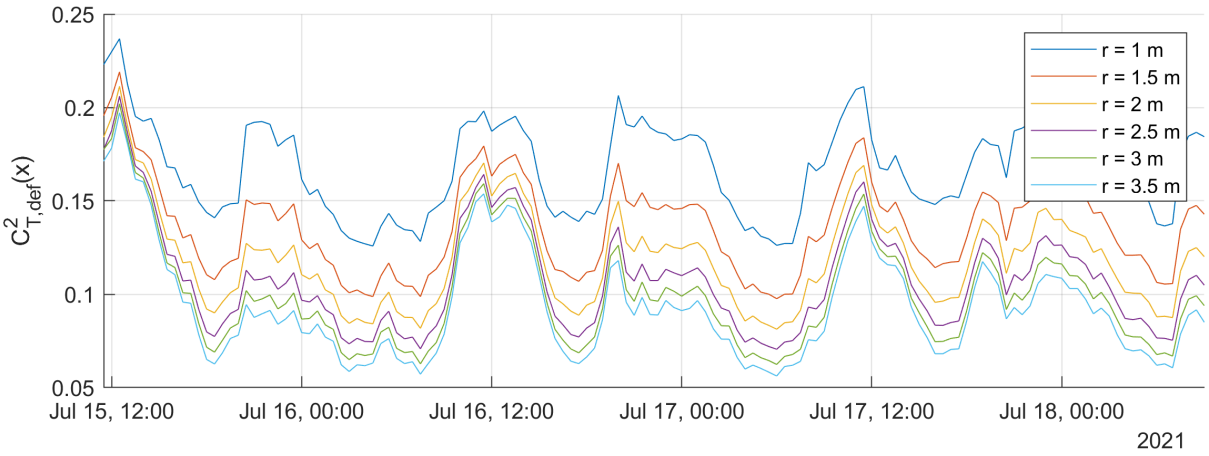

Figure 61.

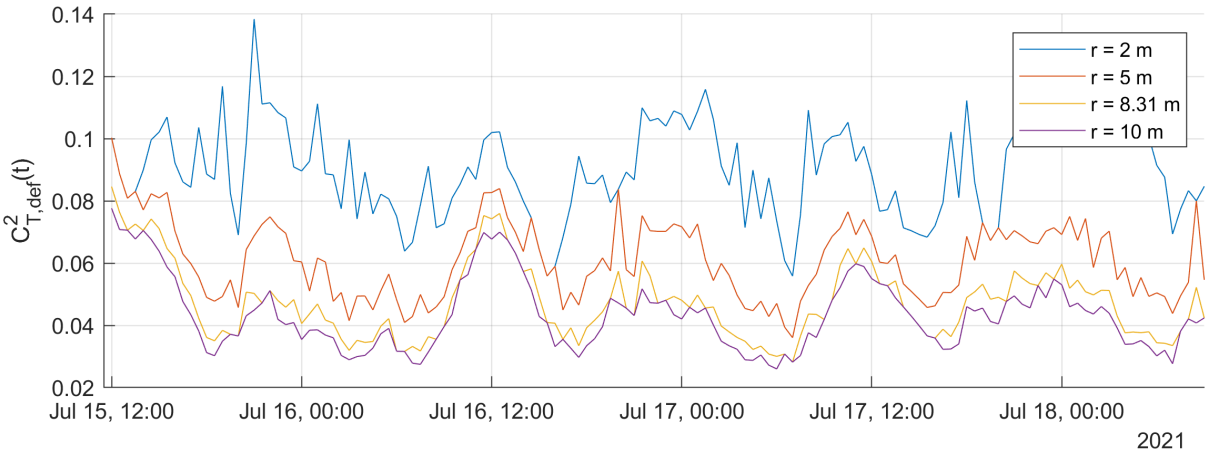

Figure 62.

F. Alternative day plots for 50 m mast

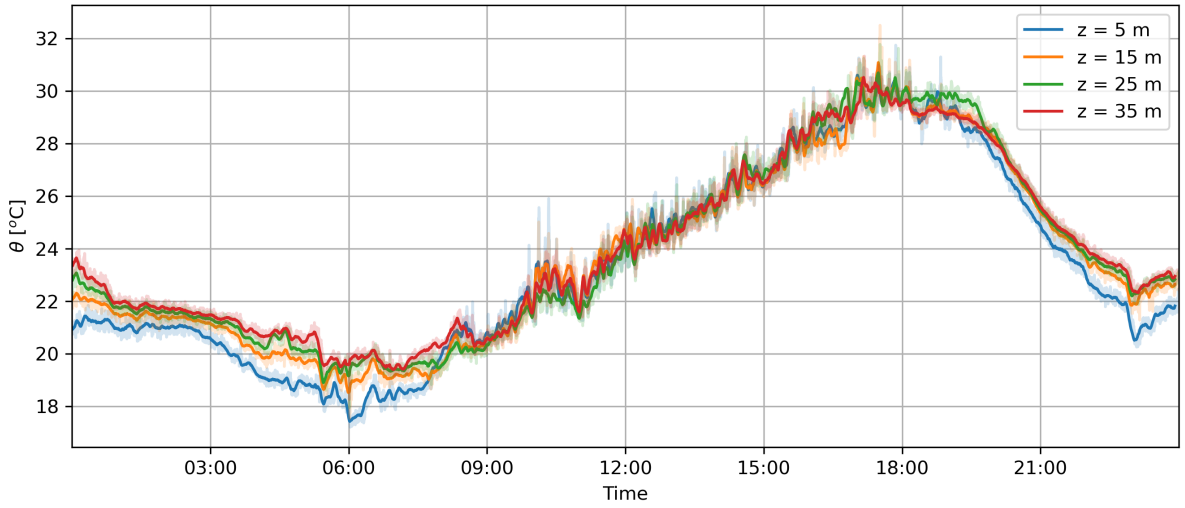

Figure 63.

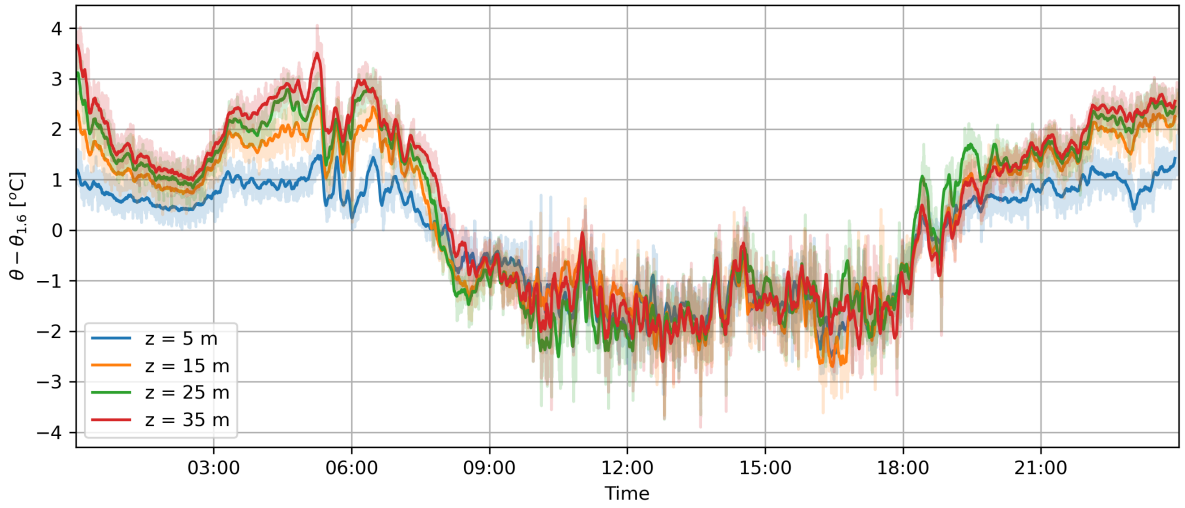

Figure 64.

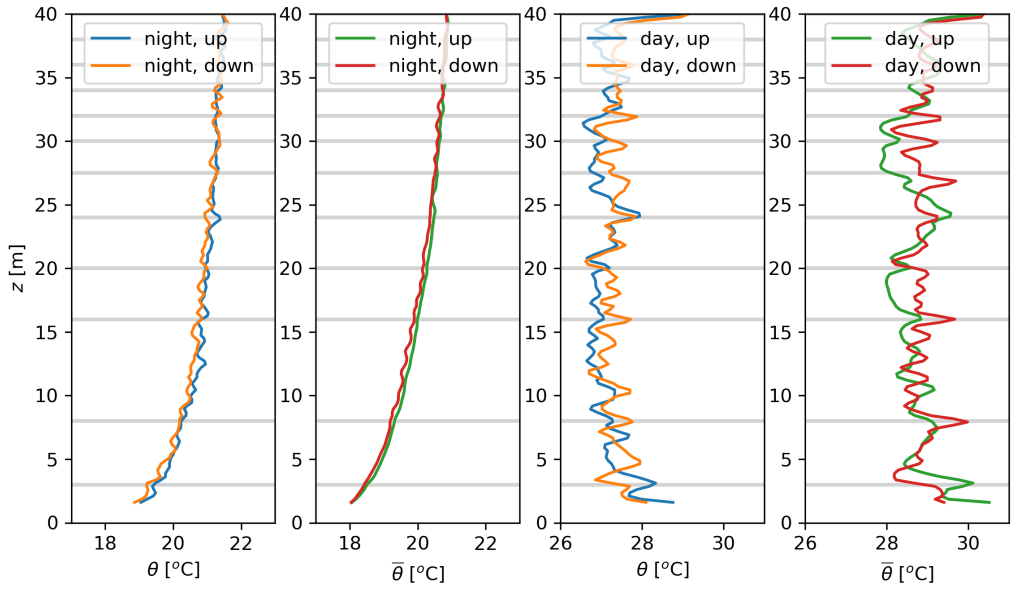

Figure 65.

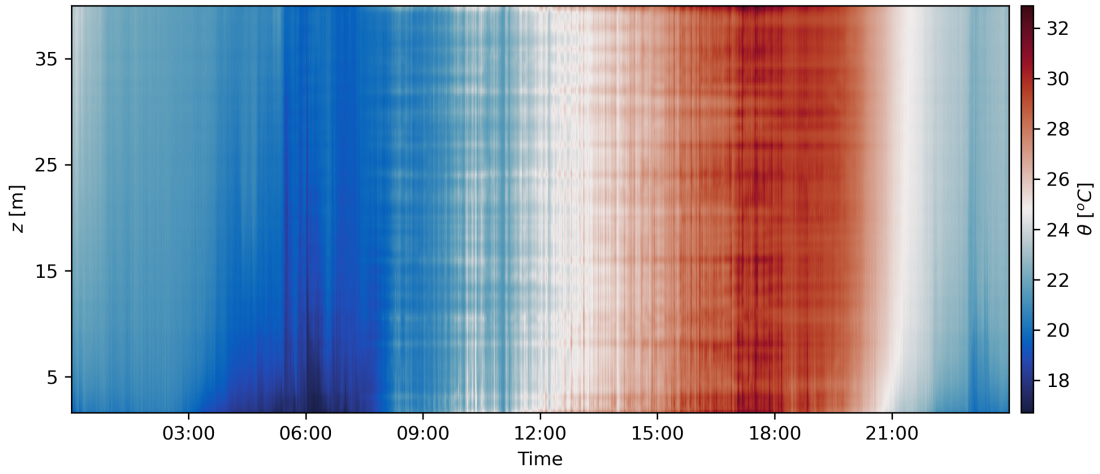

Figure 66.

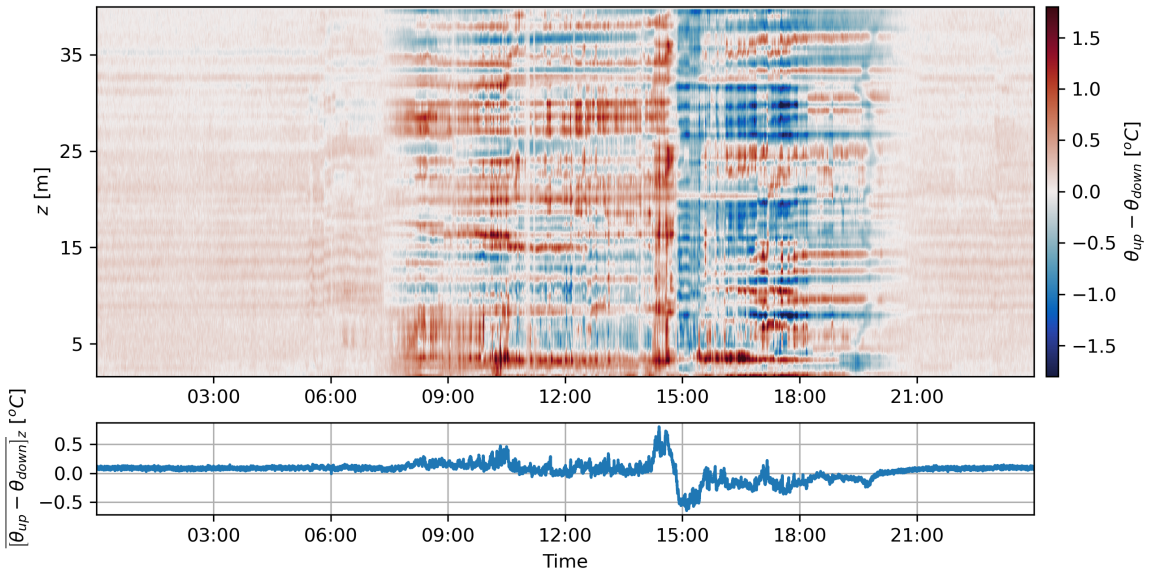
35
25
15
5
z [m]
03:00
06:00
09:00
12:00
15:00
18:00
21:00
1.5
1.0
0.5
0.0
−0.5
−1.0
−1.5
$\theta_{up} - \theta_{down}$ [°C]
$\overline{[\theta_{up} - \theta_{down}]_z}$ [°C]
0.5
0.0
−0.5
Time

Figure 67.

G. Comparison between Pt-100 and TidBit reference sensors

This chapter gives an overview of the data obtained by the reference temperature sensors and a brief comparison between their performances. The first of these reference sensors is a set of Pt-100 resistance thermometers, which were provided by WUR. The second reference sensors are a pair of HOBO TidbiT Water Temperature Data Loggers. These TidBits (Figure 68) are small battery-powered and waterproof programmable temperature loggers with a manufacturer specified 12-bit resolution, ± 0.2 °C accuracy and 5 minute reponse time.

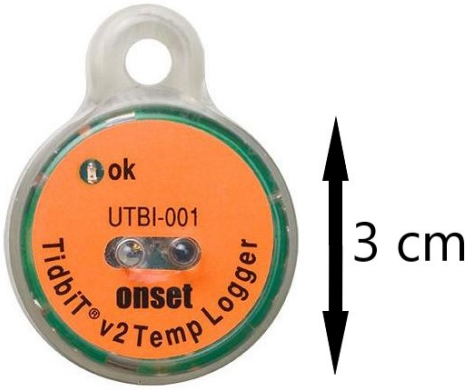

Figure 68.: HOBO TidBit Water Teperature Data Logger

The TidBits were originally brought as principal reference sensors for the outdoor calibration baths, but were made redundant by the availability of 2 Pt-100's from WUR. As a test for validation and performance, the TidBits were still deployed in the outdoor calibration baths for 6 days. The temporal resolution of the TidBits was set at 5 minutes (in order to save battery), while the resolution of the Pt-100's was 10 seconds during the whole campaign. An overview of this validation run can be seen in the time series of Figure 69 and 70 for the cold and warm outdoor baths respectively.

A slightly more illustrative view of both reference sensors is given in Figures 71 and 72. These show 1-hour zoom-ins of the time series of the warm outdoor bath of Figure 70. Figure 71 shows a time instance where the bath was refilled with ice packs and Figure 72 shows a random time instance of that same day. Replacing the ice packs has a noticeable effect which takes 30 minutes to stabilize again. The TidBit response to the ice packs lags behind with 3.0 minutes, which makes sense considering the prescribed response time of 5 minutes.

The temperature difference $\Delta T = T_{TidBit} - T_{Pt100}$ was also calculated for the validation run. This is shown in Figure 74. Here the bottom plot is a zoomed-in version of the top plot and both the warm and cold baths are plotted. The effect of the daily ice pack replacement is visible in the temperature spikes, which are between 2 and 6 degrees. The warm bath shows a diurnal trend, where the TidBit temperature is relatively higher at night, and slightly colder during the day. This is likely a radiative effect caused by the warm bath being fully exposed to Solar radiation, while the cold bath is in the shade. This would also explain why this effect is also visible in the cold bath, but less pronounced. The Pt100's were floating within the water of the calibration baths, while the TidBits where in direct contact with the Styrofoam casing. This could be the cause of this diurnal trend.

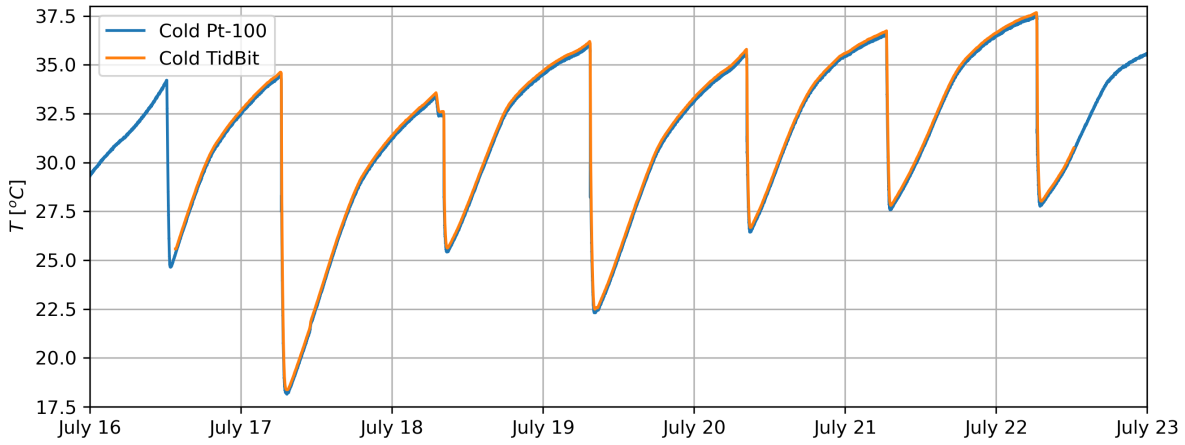

Figure 69.: Validation run time series for the cold outdoor calibration bath, showing the Pt-100 and the TidBit temperature data for six days.

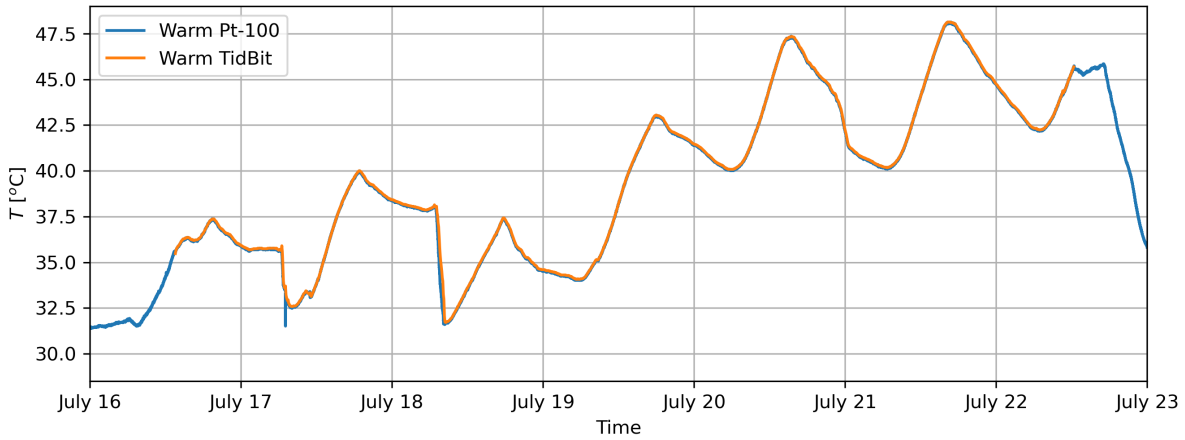

Figure 70.: Validation run time series for the warm outdoor calibration bath, showing the Pt-100 and the TidBit temperature data for six days.

The time series of the temperature difference in Figure 74 is also plotted as a histogram in Figure 73. Here the temperature distribution is visible, which seems approximately Gaussian for the cold bath, but is more skewed for the warm bath. The median temperature difference is 0.15 °C for the cold bath and 0.040 °C for the warm bath. In Figure 75 the TidBit and Pt-100 temperatures are plotted against each other, which show clear correlation. The outliers that are visible are caused by the replacing of the ice packs.

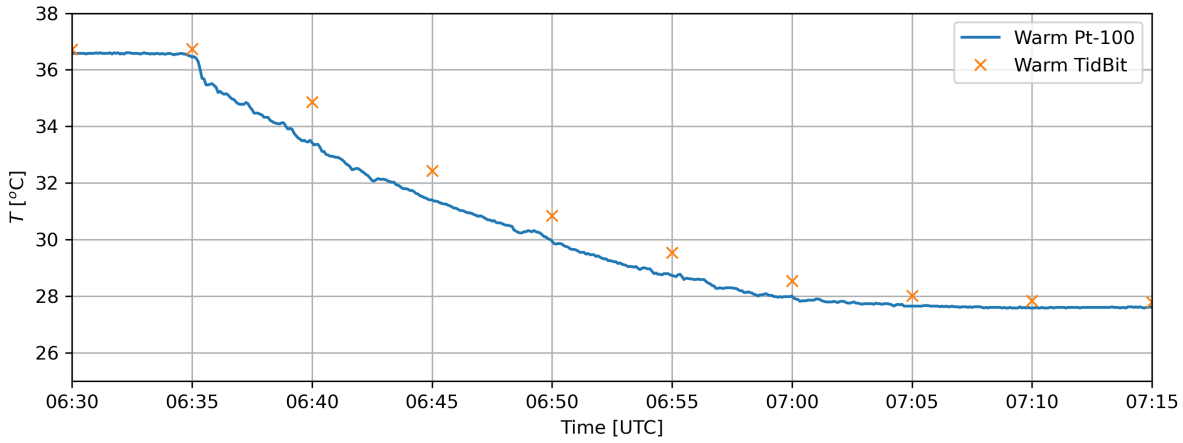

Figure 71.: Zoom-in of Figure 69 during the replacement of the ice packs.

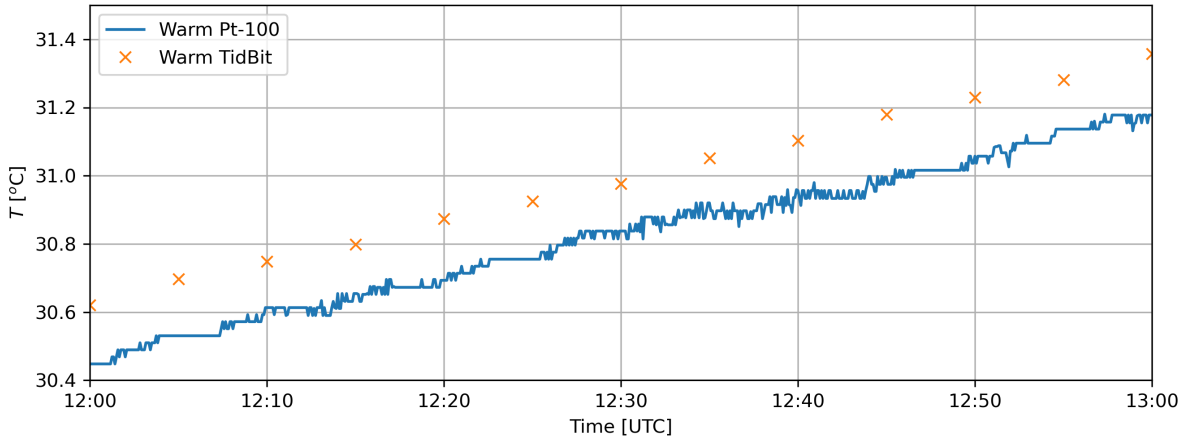

Figure 72.: Zoom-in of Figure 69 for an arbitrary hour during the same day as 71.

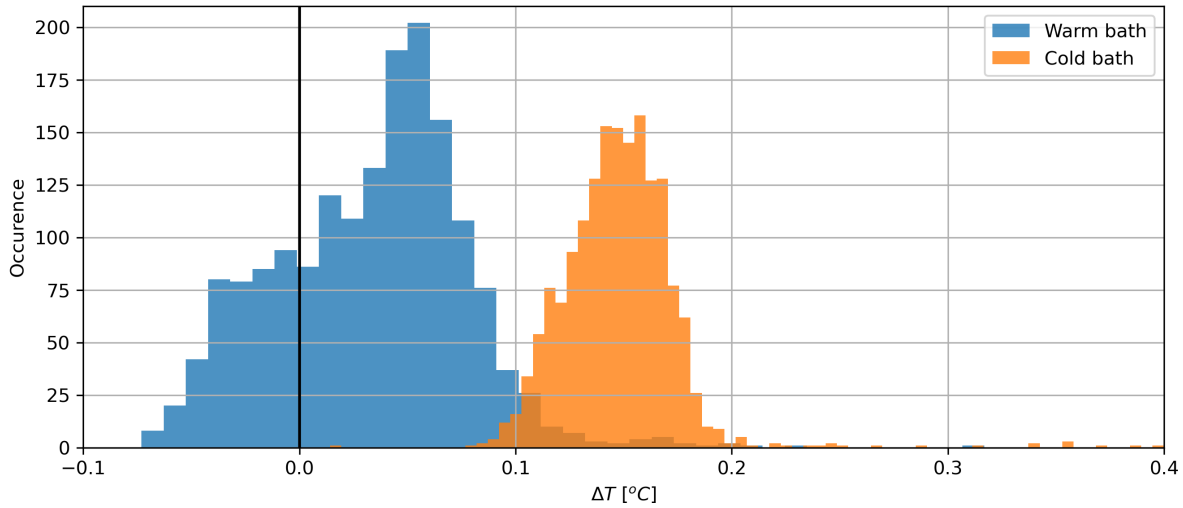

Figure 73.: Histogram of temperature difference between Pt-100 and TidBit for both outdoor baths

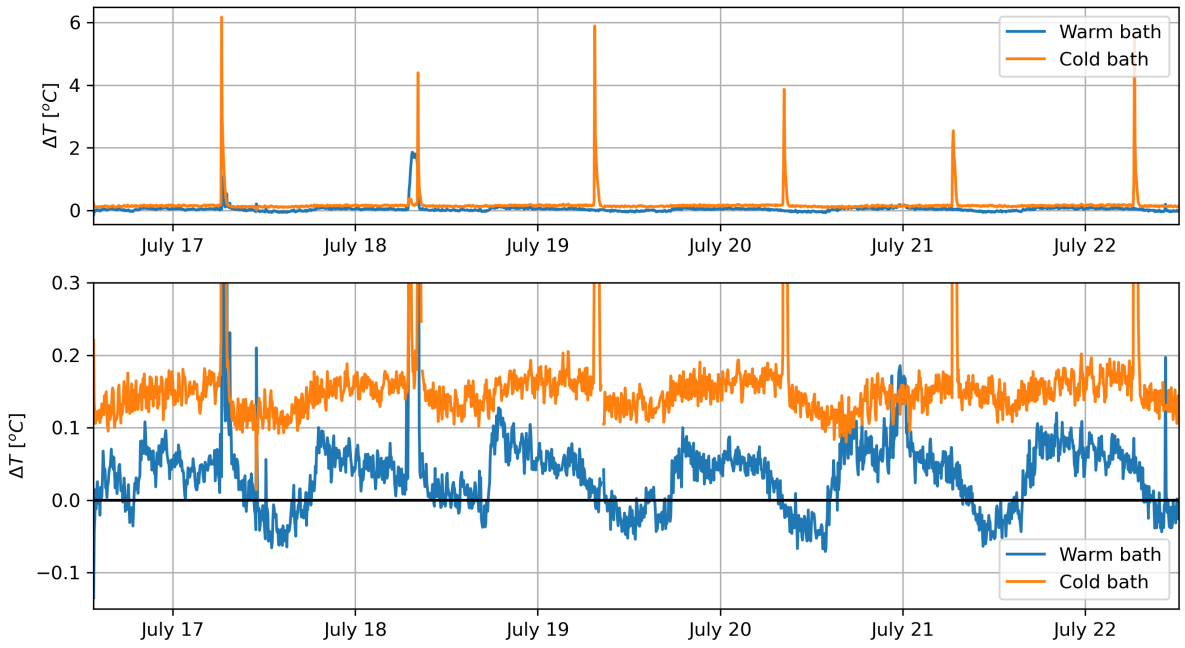

Figure 74.: Time series of temperature difference between Pt-100 and TidBit for both outdoor baths

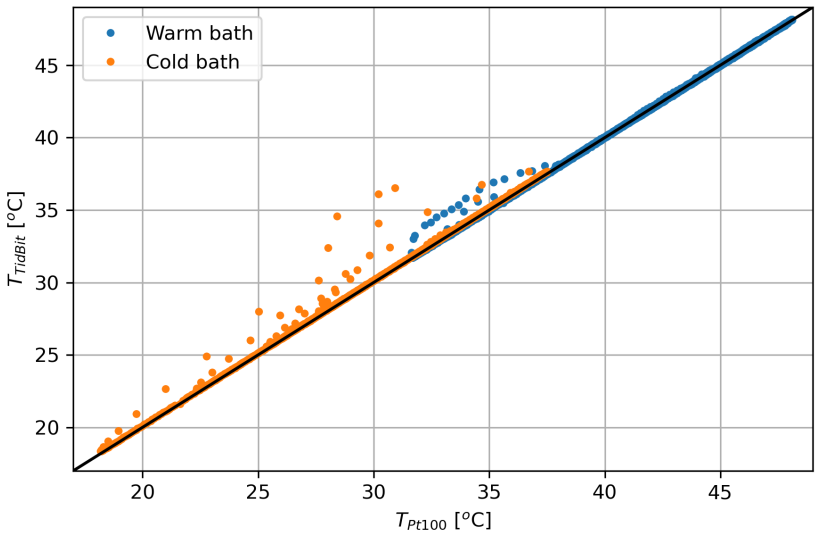

Figure 75.: Correlation plot of Pt-100 and TidBit temperature.

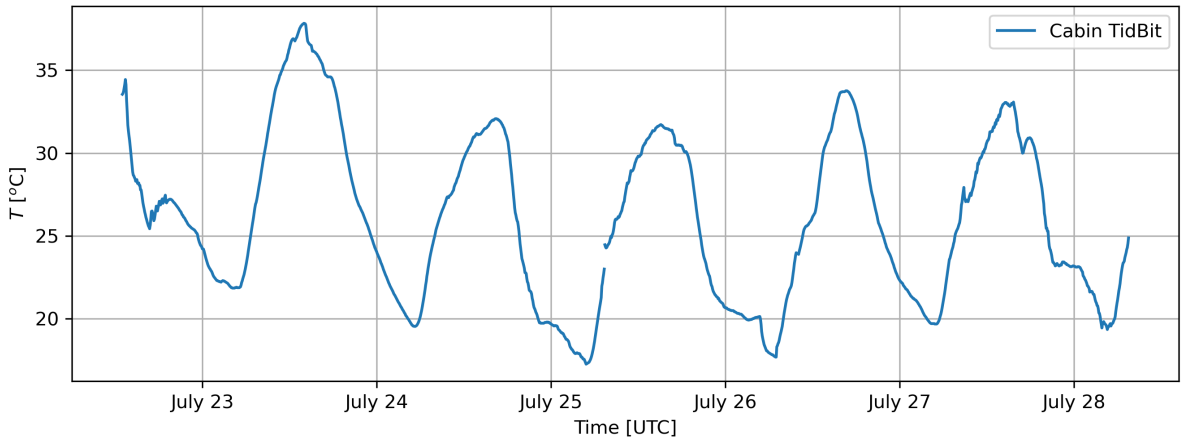

Figure 76.: TidBit temperature time series of the Dutch cabin during the heat wave when airconditioning and therefore also DTS instrumentation were turned off.

During the heat wave in the middle of the campaign DTS measurements were halted because the air conditioning in the cabin was turned off. During this time a TidBit was used to monitor the cabin temperature at low temporal frequency. For completeness this data has also been included in Figure 76.

In the final stage of the campaign the TidBits were used as a replacement of the Pt-100's as reference sensors, now at a higher time resolution of 10 seconds to match the Pt-100 sampling. Time series of the outdoor baths for these days are plotted in Figure 75.

A comparison of the performance of both the Pt-100 and TidBit sensors at 10 s measurement time is shown in Figure 78. This plot those four time series, two of the Pt-100 and two of the TidBit temperatures, at *different* time instances. The data for both sensors come from different days since there was no overlap of them measuring at the same frequency during the same time. Comparable moments were chosen and the same axis were used to allow for a qualitative comparison. For the top plot a significantly slower reaction time is visible for the TidBit during the cooling down by the ice packs. The bottom plots show the limited temperature resolution of the TidBits as compared to the Pt-100's during temperature variations during the day.

Frther research is necessary to assess whether the TidBits temperature data is of high enough quality for application in DTS calibration. For this, the next step is to use both Pt-100 and TidBit temperature series for DTS calibration and then quantify the difference in outcomes for the DTS temperatures.

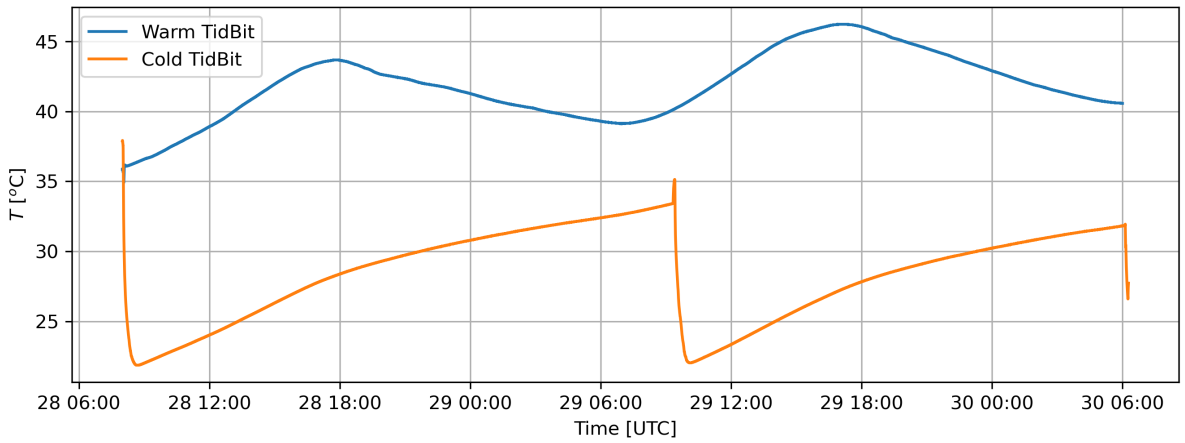

Figure 77.: TidBit temperature time series of the last days of the campaign, when the TidBits were used are replacement reference sensors.

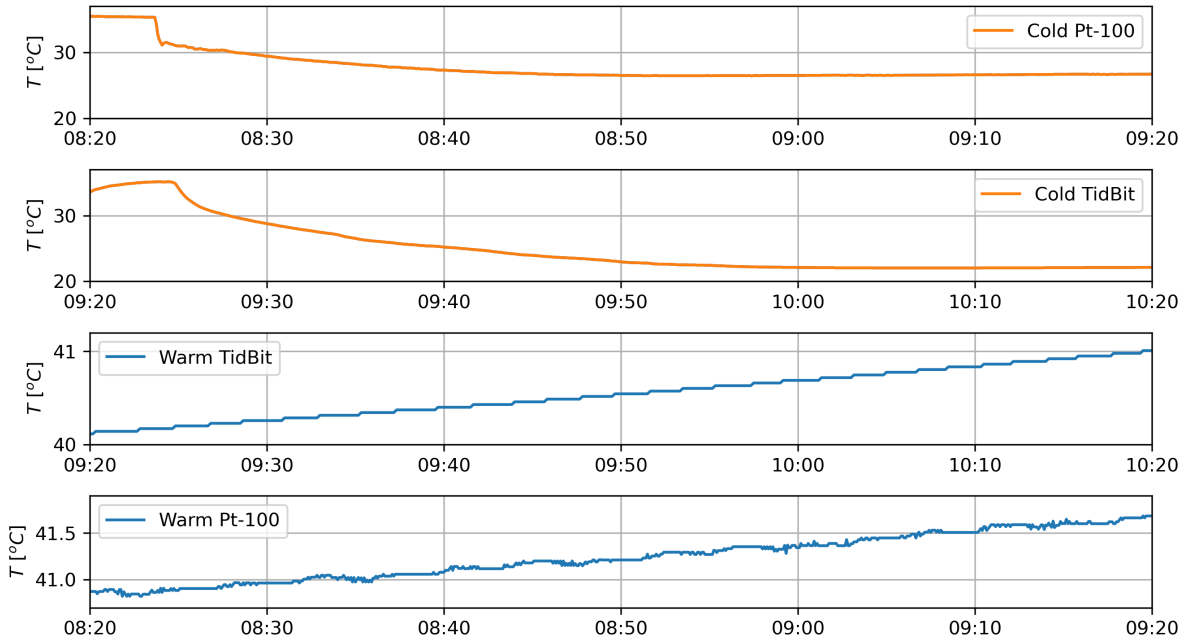

Figure 78.: Comparison plot of Pt-100 and TidBit characteristics. Top plots show a 1-hour time series of during ice pack replacement, bottom plots show a 1-hour time series of an arbitrary moment the same day. Pt-100 and TidBit time series are from *different* days.